

Dissertation
submitted to the
Combined Faculties for the
Natural Sciences and for Mathematics
of the Ruperto–Carola University of Heidelberg, Germany
for the degree of
Doctor of Natural Sciences

Put forward by

Master of Science: Volker Luiz Siegmar Kurz

Born in: Campinas, Brazil

Oral examination: February 1st, 2011

Orientation, conformation and phase
transitions of thin polymer films and
self-assembled monolayers studied by
SFG spectroscopy

Referees: Prof. Dr. Michael Grunze
Prof. Dr. Annemarie Pucci

Orientation, conformation and phase transitions of thin polymer films and self-assembled monolayers studied by SFG spectroscopy

The aim of this dissertation was the characterization of thin polymeric films on metal substrates. Of special interest were films of poly-N-isopropylacrylamide (pNIPAM). Their lower critical solution temperature (LCST) at 32°C makes this polymer attractive for many applications. The changes in the molecular structure and the dynamic of these changes at the LCST are related to macroscopic properties. Using inherently interface specific sum-frequency generation spectroscopy, gave insights into the molecular arrangement even through bulk media. The molecular groups responsible for the phase transition were identified and the influence of the molecular weight was analyzed. Order parameters were also deduced. In order to obtain quantitative information from the SFG spectra a spectral simulation program was implemented allowing for quantification of molecular orientation in the polymer films investigated. The composition of an n-layer system of the sample, angle of incidence, and molecular symmetry groups were used as parameters. Furthermore, the existing SFG spectrometer was adapted to investigate the solid/liquid interface using a freshly developed *in situ* cell as well as a novel pulse shaping technique allowing for the clear separation of the spectral phase of vibrational resonances. A reference beam line for absolute intensity measurements was also added. In addition, samples of self assembled monolayers of oligo(ethylene glycol) OEG, often used as model systems for the understanding of anti fouling materials, were investigated. The effect of different aqueous environments, temperatures, chain lengths and terminal groups on the conformations of the molecules in the film were characterized.

Untersuchung von Orientierung, Konformation und Phasenübergängen von dünnen Polymerfilmen und selbst aggregierenden Monolagen mit SFG Spektroskopie

Im Rahmen dieser Dissertation wurden dünne Polymerfilme auf metallischen Substraten untersucht. Von besonderem Interesse waren poly-N-isopropylacrylamid (pNIPAM) Filme, deren untere kritische Lösungstemperatur (engl. LCST) bei 32° liegt, was sie auch sehr attraktiv für viele Anwendungen macht. Die Veränderungen der molekularen Struktur und die Dynamiken dieser Änderungen an der Polymer/Wasser Grenzfläche bei der LCST wurden in Bezug zu makroskopischen Eigenschaften gesetzt. Die molekularen Gruppen, die den Phasenübergang verursachen wurden ausgemacht und auch der Einfluss des Molekulargewichts analysiert. Lineare optische Spektroskopie hat viele Einschränkungen bei der Analyse von verdeckten Grenzflächen, daher wurde die intrinsisch grenzflächenspezifische Summenfrequenz-Erzeugungs Spektroskopie angewandt, um selbst durch dicke Schichten hindurch die molekulare Anordnung an der Grenzfläche zu untersuchen. Dabei wurden auch Ordnungsparameter abgeleitet. Für quantitative Interpretationen dieser Spektren, wurde ein Programm implementiert, das SFG Spektren anhand zahlreicher Parameter simulieren kann, so dass die molekularen Winkel bestimmt werden konnten. Parameter für die Simulationen waren die Zusammensetzung des n-Schicht Systems, Einfallswinkel und Symmetrieeigenschaften der chemischen Gruppen. Darüberhinaus wurde das SFG Spektrometer mit einer neuen selbstentwickelten Messzelle für die fest/flüssig Grenzfläche erweitert und der "probe" Pulse wurde in der Zeitdomäne modifiziert, um die Phasen von Schwingungsresonanzen eindeutig zu bestimmen. Eine Referenzstrahllinie wurde hinzugefügt um absolute Intensitäten zu messen. Zusätzlich wurden Proben von selbst aggregierenden Monolagen von Oligo-Ethylenglycol untersucht. Diese Systeme werden häufig als Modellsystem zum Verständnis für anti Biofouling Materialien verwendet. Dabei wurde der Einfluss verschiedener wässriger Lösungen, Temperaturen, Kettenlängen und terminierenden Gruppen untersucht.

Contents

List of Figures	xi
Preface	xv
1 Introduction and aims	1
1.1 Poly(N-isopropylacrylamide) - pNIPAM	1
1.2 Oligo(ethylene-glycol)	5
1.3 Aims	8
1.3.1 Experimental obstacles	8
1.3.2 pNIPAM	8
1.3.3 Oligo ethylene-glycol SAMs	9
References	10
2 Methods	15
2.1 Fourier Transform Infrared reflection adsorption spectroscopy (FT-IRRAS)	15
2.2 Raman Spectroscopy	17
2.3 Sum-frequency generation Spectroscopy (SFG)	18
2.3.1 SFG theory	20
2.3.2 SFG spectrometer	23
2.3.2.1 Pulse shaping	28
2.3.2.2 Purging chamber	33
2.3.2.3 Sample stage	33
2.3.3 Data analysis	34
2.3.3.1 Sensitivity determination	37
2.3.4 Thin-layer analysis (TLA) cell	39
2.4 Ellipsometry	41

CONTENTS

2.4.1	Theory	41
2.4.2	Experimental design	42
2.5	Contact angle	44
	References	46
3	Materials and sample preparation	51
3.1	Gold substrates	51
3.2	Alkane thiol	51
3.3	pNIPAM	52
3.3.1	NBT-pNIPAM	52
3.3.2	Spincoated pNIPAM	52
3.3.3	ATRP pNIPAM	53
3.4	Oligo ethylene-glycols	53
3.5	Aqueous environments	55
	References	57
4	Theoretical model and Simulations of SFG spectra	59
4.1	Introduction	59
4.2	Theory	60
4.2.1	Model description	60
4.2.2	Transfer matrix method	61
4.2.3	Fundamental fields in the layered media	66
4.2.4	Sum-frequency fields	68
4.2.5	Molecular second order nonlinear susceptibility	69
4.2.6	Non-resonant $\chi^{(2)}$	72
4.2.7	Relative phases of different SFG sources	74
4.3	Experimental confirmation	74
4.4	Simulations and Discussions	75
4.4.1	Dependence of SF intensity on film thickness	77
4.4.2	Dependence of SF intensity on molecular angles	78
	References	83

5	Results & Discussion of poly-N-isopropylacrylamide	87
5.1	Ellipsometry	87
5.2	IRRAS and Raman spectroscopy	90
5.3	Contact angle	93
5.4	SFG of the CH stretching region	95
5.4.1	NBT-modified pNIPAM	95
5.4.2	ATRP pNIPAM films	100
5.5	SFG of the Amide region	106
5.6	SFG of the OH region	108
5.7	Conclusions	109
	References	111
6	Oligo ethylene-glycol	113
6.1	Quantum chemical calculations	113
6.1.1	Method	113
6.1.2	Results	114
6.2	SFG results	116
6.2.1	Chain length effect	117
6.2.2	Environmental effects	120
6.2.3	Temperature effects	121
6.3	Conclusions	122
	References	124

CONTENTS

List of Figures

1.1	Schematic of pNIPAM tethered on a gold substrate	2
1.2	LCST behavior on the macroscopic scale. Figure from B.E Xiaohu Xia [1]	2
1.3	Structure of EG ₆ OH with a C ₁₁ H ₂₂ SH linker as proposed by calculations [50]	7
2.1	Energy diagram	20
2.2	Scheme of nonlinear polarizability	21
2.3	Scheme of a typical sample composition	22
2.4	Top view image of the optical layout of the broadband SFG system after the OPA	24
2.5	General layout of the optical table	26
2.6	Beam profile of the VIS pulse at the sample stage	27
2.7	Time profile of VIS pulse	28
2.8	Etalons pulse shaping	30
2.9	Alkane thiol ppp SFG spectrum with different time delays	31
2.10	Image (isometric view) of the purging chamber	32
2.11	Image (isometric view) of the sample stage area (purging chamber not shown)	35
2.12	CCD image of the SFG signals from a Au sample and the reference line.	37
2.13	Calculation of the lower detection level of the SFG system	38
2.14	Thin layer analysis cell	40
2.15	Ellipsometer in a PCSA-configuration	42
2.16	Ellipsometer	43

LIST OF FIGURES

2.17	Photograph of two 2 mm captive air bubbles under a gold sample (a); typical image acquired from the instruments camera, for determining the contact angles. (b)	45
3.2	Chemical structure of EG _y OX and PEGOX	54
3.3	detail C1s XPS spectra	55
3.4	detail O1s XPS spectra	55
4.1	Layered medium composed of k layers and $k + 1$ interfaces embedded between ambient and substrate media.	62
4.2	Orientational angles relating the molecular-fixed and surface-fixed coordinate systems	70
4.3	Integrated area of resonant CH ₃ stretching peaks and non-resonant background from DDT-coated Au in water for <i>ppp</i> polarization at different incidence angles.	76
4.4	(a) Simulated amplitude of downward- (<i>blue</i>) and upward- (<i>purple</i>) propagating E field fields as function of depth. (b) E field amplitude as function of IR incidence angle.	77
4.5	Simulated SFG intensity of CH ₃ stretching vibrational modes as function of incidence angle from a thin layer model for various water film thicknesses (0.1-2.0 μm) for <i>ppp</i> , <i>ssp</i> , and <i>sps</i> polarizations. Molecular angles are set to polar tilt $\theta = 30^\circ$ and azimuthal turn $\phi = 15^\circ$. (a,d,g) resonant symmetric stretching <i>ss</i> , (b,e,h) resonant asymmetric stretching <i>as</i> and (c,f,i) non-resonant background	79
4.6	Simulated SFG intensity of asymmetric and symmetric CH ₃ stretching vibrational modes as function of polar angle θ from a thin layer model with water film thickness 1.0 μm and for <i>ppp</i> , <i>ssp</i> , and <i>sps</i> polarizations. (a,c,e) resonant symmetric stretching, (b,d,f) resonant asymmetric stretching. The azimuthal angle ϕ is fixed at 0°	80
4.7	Simulated SFG intensity of asymmetric and symmetric CH ₃ stretching vibrational modes as function of polar angle θ from a thin layer model with water film thickness 1.0 μm and for <i>ppp</i> , <i>ssp</i> , and <i>sps</i> polarizations. (a,c,e) resonant symmetric stretching, (b,d,f) resonant asymmetric stretching. The azimuthal angle ϕ is fixed at 30°	81

LIST OF FIGURES

4.8	Simulated SFG intensity of asymmetric and symmetric CH_3 stretching vibrational modes as function of twist angle ϕ from a thin layer model with water film thickness $1.0\ \mu\text{m}$ and for <i>ppp</i> , <i>ssp</i> , and <i>sps</i> polarizations. (a,c,e) resonant symmetric stretching, (b,d,f) resonant asymmetric stretching. The polar angle θ is fixed at 30°	82
5.1	<i>In situ</i> ellipsometric of data pNIPAM films of different thicknesses . . .	88
5.2	Fits of Ellipsometric data for thickness and refractive index of pNIPAM films of different thickness	89
5.3	IR and Raman spectra of spin coated pNIPAM films on gold	91
5.4	IR spectra of pNIPAM films of different thickness polymerized on a surface	91
5.5	Captive bubble contact angle of various pNIPAM films as function of temperature	94
5.6	NBT modified pNIPAM SFG spectra	96
5.7	Synchronous 2D SFG correlation spectrum	97
5.8	Asynchronous 2D SFG correlation spectrum	98
5.9	SFG peak intensities from the NBT-modified pNIPAM as a function of temperature	99
5.10	Resonant contributions of a <i>ppp</i> SFG spectra, showing CH stretching region of a 230 nm thick pNIPAM film on gold in water	101
5.11	Resonant contributions of a <i>ppp</i> SFG spectra, showing CH stretching region of a 110 nm thick pNIPAM film on gold in water	101
5.12	Simulated symmetric and asymmetric methyl stretch <i>ppp</i> SFG intensity as function of polar molecular angle	102
5.13	Resonant contributions of a <i>ssp</i> SFG spectra, showing CH stretching region of a 230 nm thick pNIPAM film on gold in water	103
5.14	Resonant contributions of a <i>ssp</i> SFG spectra, showing CH stretching region of a 110 nm thick pNIPAM film on gold in water	104
5.15	Background suppressed SFG spectra, showing Amide region of a 230 nm thick pNIPAM in air during a temperature sweep	105
5.16	Background suppressed SFG spectra, showing Amide I band of 110 nm thick pNIPAM	107

LIST OF FIGURES

5.17	Integrated SFG intensity in the spectral region of OH stretches acquired with <i>ssp</i> and in the background suppressed mode, normalized with the reference line signal.	108
6.1	Geometry optimized conformations of HME (a) in air (b) interacting with a H ₂ O molecule	114
6.2	<i>Ab initio</i> and experimental spectra of EG ₁ OH - (points) experimental data (solid line) calculated spectra. (a) in air (b) in D ₂ O	115
6.3	SFG spectra in the CH stretching region of EG ₁ OH.	116
6.4	SFG spectra in the CH stretching region of EG ₁ OH-EG ₆ OH	117
6.5	SFG spectrum of EG ₆ OMe (left) and EG ₆ OH (right)	119
6.6	SFG spectrum of PEG2000OH (left) and PEG2000OMe (right).	119
6.7	background suppressed SFG spectra of EG ₆ OH	121
6.8	SFG spectra of EG ₆ OCH ₃ SFG spectra in the CH stretching region with <i>ssp</i> polarization	122

Preface

This doctoral work has been performed at the Department of Applied Physical Chemistry at the University of Heidelberg, with Prof. Michael Grunze as the main supervisor and with co-supervisors Prof. Annemarie Pucci and Priv. Doz. Dr. Patrick Kölsch. The research was performed at facilities of the University of Heidelberg and the KIT-Campus Nord.

The aim of this doctoral research was the characterization of thin polymeric films on metal substrates. Films of poly-N-isopropylacrylamide (pNIPAM) and oligo (ethylene-glycol) (OEG) are of great interest due to their unique properties. pNIPAM exhibits a lower critical solution temperature (LCST) phase transition at physiological relevant 32°C in water. Self assembled monolayers of OEG are often used as model systems for the understanding of antifouling materials.

Understanding the origin of these properties can help in the discovery and improvement of responsive polymers. In order to achieve this goal, different techniques were applied to elucidate changes in the molecular structure and dynamics. The molecular groups responsible for the phase transition were identified.

The effect of different aqueous environments and temperatures on films were characterized, and the dependency of the conformation on the chain length and terminal group was quantified.

Interfaces can often be difficult to see experimentally, as they are buried between bulk media, e.g. a gold substrate and water. In order to probe such interfaces a novel sample cell was developed, able to create a "window" through absorbing liquid media to the interface. Sum-frequency generation (SFG) spectroscopy was chosen as probing technique due to its ability to exclusively probe interfacial molecular groups. The SFG spectrometer used for these experiments was augmented with a novel pulse shaping technique in order to clarify the spectral phase of vibrational resonances. Furthermore,

0. PREFACE

a reference beam line was added for absolute intensity measurements. Other methods such as ellipsometry and IRRAS were applied to probe the thickness and the overall chemical composition of the films. Each of these technique probes selectively different parts of the interface and the combination provides a profound picture of the interfacial architecture.

Furthermore a program able to simulate SFG spectra was implemented, allowing for quantification of molecular orientation in the investigated polymeric film. The composition of an n-layer system of the sample, angle of incidence, molecular symmetry groups, and molecular vibrational modes were used as parameters.

This research will help further the knowledge of the molecular structure of polymer surfaces at buried interfaces.

Own papers regarding the work in this thesis

- In-situ characterization of thermo-responsive poly(N-isopropylacrylamide) films with sum-frequency generation spectroscopy
V. Kurz, M. Grunze and P. Koelsch
ChemPhysChem, 11 (2010) 1425–1429.
- Sample cells for probing solid/liquid interfaces with broadband sum-frequency-generation spectroscopy
D. Verreault, V. Kurz, C. Howell and P. Koelsch
Review of Scientific Instruments, 81 (2010) 06311/11–10.
- Sum-frequency-generation in layered media: angular and thickness dependence
V. Kurz, D. Verreault and P. Koelsch
Manuscript
- Characterizing oligo ethylene glycol self-assembled monolayers with sum-frequency-generation spectroscopy under different environmental conditions
V. Kurz, M. Grunze and P. Koelsch
Manuscript

Other contributions as a PhD student:

- In vitro characterization of surface properties through living cells
M.-O. Diesner, C. Howell, V. Kurz, D. Verreault and P. Koelsch
Journal of Physical Chemistry Letters, 1 (2010) 2339–2342.
- Sum-frequency-generation spectroscopy of DNA films in air and aqueous environments
C. Howell, R. Schmidt, V. Kurz and P. Koelsch
Biointerphases, 3 (2008) FC47–FC51

As a master student:

- Measurement of the infrared complex Faraday angle in semiconductors and insulators
M.-H. Kim, V. Kurz, G. Acbas, C. T. Ellis and J. Cerne
JOSA B, 27 (2010). (Galley proofed)

0. PREFACE

Conference contributions:

- Volker Kurz and Patrick Koelsch, *"A closer look on the thermo-responsive behavior of ultrathin pNIPAM films relating interfacial molecular transitions to macroscopic properties"*, 2nd HGS Mathcomp Annual Colloquium, Heidelberg, Germany, November 18th 2010.
- Volker Kurz and Patrick Koelsch, *"A closer look on the thermo responsive behavior of thin pNIPAM films - relating molecular transitions to macroscopic properties"*, ECIS 2010, Prague, Czech Republic, September 6–10, 2010.
- Volker Kurz, Dominique Verreault, Mark-Oliver Diesner, Caitlin Howell and Patrick Koelsch *"In situ and in vitro characterization of solid/liquid interfaces using nonlinear optical spectroscopy"*, Auftaktkongress zum Strategieprozess "Nächste Generation Biotechnologische Verfahren 2020", Berlin, Germany, July 8th 2010.
- Volker Kurz and Patrick Koelsch, *"In situ SFG spectroscopy on ethylene glycol and poly-N-isopropylacrylamide at different temperatures"*, 1st HGS Mathcomp Annual Colloquium, Heidelberg, Germany, October 2009.
- Volker Kurz and Patrick Koelsch *"In situ sum-frequency-generation spectroscopy on ethylene glycol and poly-N-isopropylacrylamide at different temperatures"* APS Meeting, Pittsburgh, USA, March 16–20 2009.
- Patrick Koelsch, Dominique Verreault, Volker Kurz, Caitlin L. Howell, Ronny Schmidt, *"In-Situ Broadband Sum-Frequency Spectroscopy of Biomolecules at Interfaces"*, AVS Meeting, Boston, USA, October 19–24, 2008.
- Patrick Koelsch, Caitlin L. Howell, Ronny Schmidt, Dominique Verreault, Volker Kurz and Michael Grunze, *"Sum-frequency generation spectroscopy of single stranded DNA monolayers"*, ECIS 2008 Conference, Cracow, Poland, 31 August – 5 September, 2008.
- Volker Kurz, Michael Grunze and Patrick Koelsch, *"Characterization of pNIPAM and EG6OH in solution by sum-frequency spectroscopy"*, Bunsentagung "Analyse, Manipulation und Simulation auf der Nanometerskala", Saarbrücken, Germany, Mai 1–3 2008.(suggested for a poster award)

Introduction and aims

The behavior of many polymer systems is controlled by properties of their surfaces and interfaces. Such properties include wettability, adhesion, biocompatibility, permeability, rheology, morphology, charge and are widely used in modern technology fields. The properties of polymer materials at surfaces and interfaces are strongly dependent on the chemical structure. Therefore, in order to control polymer surface/interface properties by manipulating surface and interface structures, there must be an extensive database of detailed correlations between properties and structures. Confined to a surface, polymer molecules may have different structure or conformation when compared to the bulk. As a result, it is crucial to study polymer structure at the interface using techniques that are sensitive to the surface and interface.

1.1 Poly(N-isopropylacrylamide) - pNIPAM

In this work the molecular morphology of poly(N-isopropylacrylamide) (pNIPAM) was investigated for particular molecular subgroups at the polymer/water interface. The well-defined Lower Critical Solution Temperature (LCST) at around 32°C makes this polymer so popular in science and industry. Polymer chains exhibit temperature-dependent solvation behavior in which they become less solvated with increasing temperature. This results in a thermo-responsive behavior, the origin and consequences of which have not yet been completely investigated. Fig. 1.1 shows a simplified scheme of the thermo-responsive behavior for polymer chains grafted on a flat substrate. By definition the LCST is the critical temperature below which a mixture is miscible. The

1. INTRODUCTION AND AIMS

LCST mechanism for pNIPAM-water solutions involves the loss of water solvent in the hydrated film, which results in a loss of water solubility. The macroscopic changes are illustrated in Fig. 1.2 from B. E. Xiaohu Xia,[1] in which a hydrogel of pNIPAM particles is shown. In this example the viscosity is increased above the LCST as shown in b) and the radius of the particles, as determined by dynamic light scattering (DLS) is plotted in c).

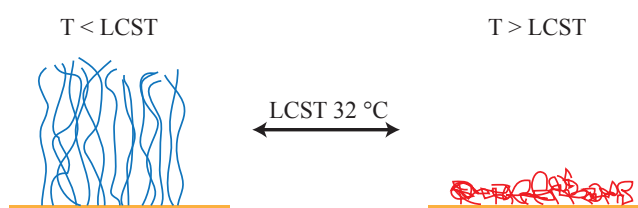


Figure 1.1: Schematic of pNIPAM tethered on a gold substrate - below the LCST (left) and above the LCST (right)

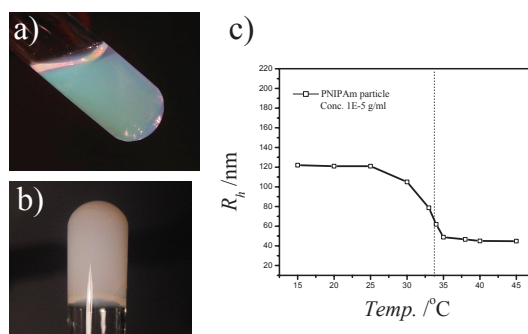


Figure 1.2: LCST behavior on the macroscopic scale. Figure from B.E Xiaohu Xia [1] - a) photograph of semi-dilute aqueous solution below the LCST, b) above the LCST and c) radius of hydrogel particles as function of temperature.

The aim of the thesis is to characterize the molecular rearrangement of surface-immobilized pNIPAM especially at the interface during the phase transition from the mixed to the segregated phase, and to identify the molecular groups which change orientation, hydration and conformation. This work was also undertaken in order to answer the question of whether these changes occur instantaneously like results from advancing contact angle measurements are showing [2, 3, 4] or if they occurring already before the film reaches the transition temperature.

PNIPAM has become one of the most widely used stimulus-responsive polymers due to its applicability to a wide range of applications, such as biointerfaces,[5, 6, 7, 8, 9, 10] controlled drug delivery systems,[11, 12, 13, 14, 15], permeation-controlled filters,[16] and functional composite surfaces.[17, 18, 19] These polymers are also one of the most widely used stimulus-responsive materials for bioengineering applications due to their ability to release biological cells intact. To date, there has been a great deal of effort invested into the use of pNIPAM films to release cells. However, most of this research focusing on cell release has centered around the applications, not the mechanism of release. The applications most often investigated are mammalian cell release, cell sheet engineering[20], tissue transplantation[21], the study of the extracellular matrix underlying cells[22], and the formation of shapes and spheroids[23]. Yet despite the volume of literature available on this topic, only a few systematic studies exist. Such studies will be of critical importance to the understanding of fundamental issues involving these films, such as the importance of film thickness for cell release. In this work the results of systematic thickness-dependent investigations are reported.

A variety of different experimental techniques have been used to characterize pNIPAM films *in situ*. Surface plasmon resonance (SPR),[3, 24] and quartz crystal microbalance (QCM) have been used to characterize the bulk polymer as well as to monitor dynamic processes such as water adsorption and segregation in these films. Neutron reflectivity,[25] and ellipsometry [26] have also been used to investigate the dynamics of the film thickness changes and to a limited extent the chemical composition depth profile. Atomic force microscopy (AFM),[27, 28] has been used as an efficient probe to detect surface morphology, friction, and adhesion properties with high spatial resolution. In order to obtain chemical information, IR reflection absorption spectroscopy (IRRAS) has been used to obtain information from these films adsorbed on reflective substrates. However, in order to examine the films *in situ* it becomes necessary to probe through a bulk water phase located above the film, which would absorb most IR intensity. Putting the polymer on an IR transparent substrate and probing from the substrate side can solve this problem, permitting detection of the polymer without passing the beams through a bulk water. However, IR spectroscopy is not interface specific, and will gather information from all the matter through which the probing beam travels, not only the polymer itself. Furthermore contributions from the polymer interface will likely be quite small compared to the bulk signal. Special

1. INTRODUCTION AND AIMS

modification of IR spectroscopy such as PM-IRRAS (Polarization Modulation Infrared Reflection Absorbance Spectroscopy) allow for probing of only the first few μm of the material, but in this work interfaces of only a few nm thick films are of the greatest interest. The interface specific nonlinear spectroscopic techniques of second-harmonic-generation (SHG) and sum-frequency-generation (SFG) vibrational spectroscopy have emerged as particularly well-suited tools to study adsorbates at various interfaces at these scales.[29, 30, 31, 32, 33, 34, 35, 36, 37, 38] Sum-frequency can be generated in any media with a second order nonlinear susceptibility. At an interface this susceptibility is always non-zero since the inversion symmetry of the molecular groups is broken. SFG spectroscopy allows for both probing the polymer-water interface and the water-polymer interface. Due to the selection rules, the SF beam generated carries information about the chemical and structural properties of the probed material, similar to IR and Raman spectroscopy. SFG spectroscopy has been previously applied to pNIPAM by Cheng et al.[39] and Miyamae et al.[40] to study the orientation of side-chain groups at the air/pNIPAM interface, and the water/pNIPAM interface both below and above the LCST. In air and above the LCST in water, strong CH_3 stretch peaks were observed which indicated the presence of ordered isopropyl groups from the polymer side chain tilting toward the surface normal, either orienting to the interior of the polymer or in the plane of the surface. In contrast, at room temperature the SFG spectrum at the water/pNIPAM interface indicates an orientation of the hydrophobic isopropyl groups away from the surface. Similarly, Miyamae and co-workers used SFG spectroscopy to study *in situ* pNIPAM films chemically grafted on quartz in various polarization combinations below and above the LCST. However, none of these studies have elucidated the molecular arrangement during the LCST transition. A deeper analysis of the spectral data allows deduction of the phase of each single molecular resonance and therefore their orientation. Yet even without a phase resolved measurements, molecular angles can be obtained for systems with certain constraints, such as a particular polarization combination of the the incoming beams and isotropic distribution of molecular orientation relative to a coordinate axis. For example, the orientation of the polar angle of a methyl group can be deduced by the ratio of the signal from the asymmetric and symmetric stretches. In order to understand this relation between molecular angles and SFG spectra, a program was developed within the framework of the doctoral research. The SFG spectral analysis using this program revealed which molecular groups were

involved in the reorientation and disordering of the polymer chains during the LCST transition of pNIPAM. The high spectral resolution allowed differentiation between differently "hydrated" isopropyl groups, as well as between the interfacial groups and those a few molecular units into the ultrathin polymer film. Reorientation within the pNIPAM film as function of thickness ranging from 10-200 nm and temperature was recorded. The macroscopic properties of the film through the Lower Critical Solution Temperature (LCST) transition were also tracked in great detail by ellipsometry and capturing bubble contact angle, which allows for the measurement of the thickness, and water content within the film, as well as the changes in surface energy, chemical potential and interfacial entropy. These results were correlated with data acquired by *in situ* SFG spectroscopy. A smeared transition in the range between 20°C and 40°C is common in the macroscopic studies of these systems. Pushing the limits of the SFG, the effect of interfacial water orientation on the pNIPAM film during the LCST, was also analyzed. The increasing order of the water interface in the segregated phase was visualized.

These studies serve to bridge the gap between macroscopic and microscopic properties and increase the understanding of the dynamic properties of pNIPAM in water at solid interfaces.

1.2 Oligo(ethylene-glycol)

In addition to pNIPAM, self-assembled monolayers (SAMs) of oligo ethylene-glycol (OEG) are also of interest, both theoretically and experimentally. These systems are an ideal as experimental models, for studying molecular orientations and conformations due to their already widely investigated properties. They are of special interest, because of their application as protein resistant coatings for biomaterials and antifouling issues. The undesired growth of marine organisms on submerged surfaces, is a global problem with both economic and environmental consequences.[41, 42]. The use of biocidal antifouling paints is increasingly restricted, therefore science and industry are seeking environmentally benign coatings to control the fouling. In this area basic research can contribute a great deal to fundamental understanding by determining which surface properties either inhibit settlement of the colonizing stages of fouling organisms, or reduce adhesion strength of the attached organisms, so that they are more easily removed

1. INTRODUCTION AND AIMS

by shear forces. OEG SAMs have been used for protein and cell adhesion studies for many years, and their surface properties have been characterized in detail by various techniques. It is already known that steric repulsion is the major mechanism behind antifouling properties of these systems, as determined by De Gennes, Andrade and Jeon in 1986.[43, 44, 45] Poly ethylene-glycol (PEG) chains are heavily hydrated at the water interface, which prevent protein adsorption, since overcoming such hydration would require huge pressure to press the water out of the film. Beside needing a large amount of energy to accomplish this, the entropy of the film would also be reduced due reduced space for the polymer chains themselves. For shorter OEG SAMs of a high packing density, the protein resistance can not be explained by steric repulsion since the short chains restrict the conformation realization possibilities already in such a way that a further entropy loss upon protein adsorption is only minor. There is less space for water molecules inside such films. A model explaining the protein resistance for these systems stated that with an increased hydronium concentration at the interface and the resulting negative charge results in a repelling of most proteins, which are primarily negatively charged.[46, 47]

Previous quantum chemical approaches already describe the conformations of OEG systems in the hydrated state. Using density functional theory with nonlocal corrections, researches have found that solvated EGOCH_3 moieties with non-uniform gauche rotations are by far the most stable in solvated state.[48] Studies of the interaction of water with oligo(ethylene glycol) in the helical and planar all-trans form with *ab initio* methods to determine the stability and density distributions in water clusters as function of the molecular conformation were done by Wang and Kreuzer.[49] Static energy minimization and Monte Carlo simulation were used to study the effect of external electrostatic fields on the structure of OEGs.[50]

Pertsin and Grunze [50] used grand canonical Monte Carlo simulations to determine that the conformation of EG_3OH terminated alkane thiols on gold in contact with water was helical. In addition, they found that the conformations of the molecules depend heavily on the packing density and will be, for example, "zig zag" on silver substrates. The proposed conformation of EG_3OH on gold in water was assumed to be helical for EG_6OH as well, but was not calculated. Fig. 1.3 shows the assumed conformation. Due to the complexity of these systems, all these theoretical studies cannot not include the impact of different aqueous solutions and temperatures on films consisting of more than

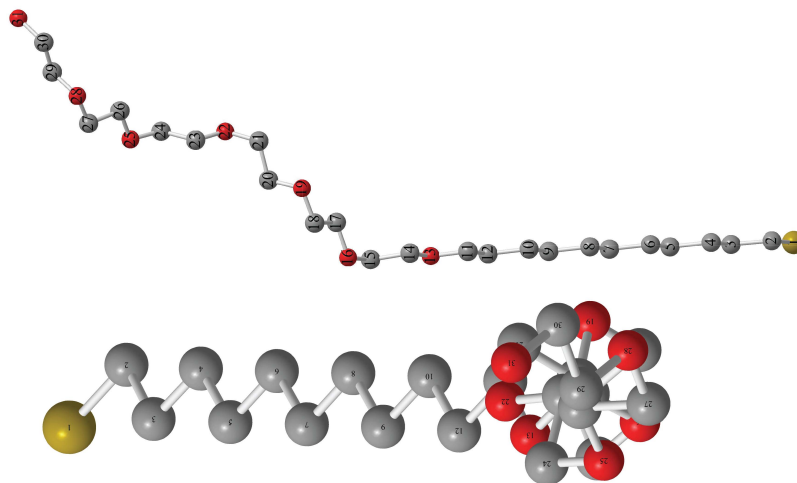


Figure 1.3: Structure of EG₆OH with a C₁₁H₂₂SH linker as proposed by calculations [50] - The results postulate the shown conformation only for EG₃OH, however an extrapolation for EG₆OH is shown. A view from the side and one from top of the helix.

a few EG units. Experimentally, the bulk conformations of PEG in different media or at different temperatures have been widely studied with IRRAS [51, 52] and Neutron scattering experiments [53]. In this work, SFG is applied to verify these findings and allow for conclusions beyond those results to be made. Some SFG have previously been done on this topic but not in a detailed or systematic manner [54, 55] or do not include environmental conditions. [56]

Hydration plays a key role in the understanding of the antifouling issues. This aspects are investigated in detail in this work. Using SFG spectroscopy, which is able to investigate both the conformational order and the hydration of particular molecular groups at the same time. The differences in the properties for applications in a laboratory system and in environmental condition, namely phosphate buffer saline (PBS) and artificial sea water (ASW) are investigated. The purpose is to quantify the influence of different ions and environmental conditions on the film properties on the molecular scale by SFG spectroscopy *in situ*. Also the effect of temperature on the conformation is also investigated.

1. INTRODUCTION AND AIMS

1.3 Aims

1.3.1 Experimental obstacles

Several experimental obstacles had to be accomplished in order to answer the scientific questions outlined in the previous section.

- Augmentation of the SFG spectrometer for directly probing the solid/liquid interface through the bulk of the water phase at various environmental conditions, temperatures, and incident angles, without losing too much pulse energy.
- Implementation of a reference beam line for quantitative analysis of the SFG signal intensity in order to make conclusions about the amount of ordered molecular groups.
- Optimization of data treatment and analysis, allowing for the calculation of molecular angles. This includes the simulation of an entire SFG spectrum by inputting parameters such as the layer composition of the sample, incident angles and polarizations, molecular symmetries and angles and electronic properties of the substrate.
- Building of a purging chamber to access certain spectral regions without the ambient atmospheric absorption bands.
- Modification of the probing pulse in order to obtain spectra solely from the interface and not from the substrate, allowing for the recording of phase resolved spectra.
- Calculation of vibrational modes with *ab initio* methods for peak assignments.

1.3.2 pNIPAM

The general scientific targets which needed to be accomplished for the pNIPAM studies are:

- Identification of molecular groups which change conformation and orientation at the LCST transition of pNIPAM.

- Determination of the different steps of reorganization of the molecular groups during the LCST.
- Quantification of the molecular angles as well of the side groups as of the polymeric backbone before and after the LCST transition of the polymer.
- Investigation of the dependencies of the molecular weight and grafting density on the transition.
- Verification of the reproducibility of the phase transition.
- Analysis of the interfacial orientation of the water molecules during the LCST transition.
- Correlation of the microscopic molecular findings with macroscopic changes observed by ellipsometry and contact angle.

1.3.3 Oligo ethylene-glycol SAMs

Scientific aims of the OEG SAM studies were:

- To reveal the structure of various OEG SAMs on gold in aqueous solutions with SFG spectroscopy.
- Verification of the influence of modifications such as different head groups and chain length on the SAMs.
- To check the hydration of different OEG SAMs on the molecular scale.
- Elucidation of the effect of different environmental conditions such as ions and temperature on the film structure and hydration behavior.
- Comparison of the experimental results with previous outcomes of theoretical methods.

REFERENCES

References

- [1] B. Xiaohu Xia, *Fabrication and light scattering study of multi-responsive nanostructured hydrogels and water-soluble polymers*. PhD thesis, University of North Texas, 2003. [xi](#), [2](#)
- [2] J. Zhang, R. Pelton, and Y. Deng, “Temperature-dependent contact angles of water on poly(n-isopropylacrylamide) gels,” *Langmuir*, vol. 11, pp. 2301–2302, 1995. [2](#)
- [3] S. Balamurugan, S. Mendez, S. S. Balamurugan, M. J. O’Brien, and G. P. Lopez, “Thermal response of poly(n-isopropylacrylamide) brushes probed by surface plasmon resonance,” *Langmuir*, vol. 19, no. 7, pp. 2545–2549, 2003. [2](#), [3](#)
- [4] K. N. Plunkett, X. Zhu, J. S. Moore, and D. E. Leckband, “Pnipam chain collapse depends on the molecular weight and grafting density,” *Langmuir*, vol. 22, no. 9, pp. 4259–4266, 2006. [2](#)
- [5] R. M. P. da Silva, P. M. Lopez-Perez, C. Elvira, J. F. Mano, J. S. Roman, and R. L. Reis, “Poly(n-isopropylacrylamide) surface-grafted chitosan membranes as a new substrate for cell sheet engineering and manipulation,” *Biotechnol. Bioeng.*, vol. 101, no. 6, pp. 1321–1331, 2008. [3](#)
- [6] T. Chen, J. M. Zhong, D. P. Chang, A. Carcia, and S. Zauscher, “Fabrication of micropatterned stimulus-responsive polymer-brush ‘anemone’,” *Advanced Materials*, vol. 21, no. 18, pp. 1825–1829, 2009. [3](#)
- [7] D. P. Chang, J. E. Dolbow, and S. Zauscher, “Switchable friction of stimulus-responsive hydrogels,” *Langmuir*, vol. 23, no. 1, pp. 250–257, 2007. [3](#)
- [8] M. A. Cole, N. H. Voelcker, H. Thissen, and H. J. Griesser, “Stimuli-responsive interfaces and systems for the control of protein-surface and cell-surface interactions,” *Biomaterials*, vol. 30, pp. 1827–1850, 2009. [3](#)
- [9] M. A. Cole, M. Jasieniak, N. H. Voelcker, H. Thissen, R. Horn, and H. J. Griesser, “Switchable surface coatings for control over protein adsorption - art. no. 641606,” *Biomed. Applications of Micro- and Nanoengineering III*, vol. 6416, p. 41606, 2007. [3](#)
- [10] M. D. Kurkuri, M. R. Nussio, A. Deslandes, and N. H. Voelcker, “Thermosensitive copolymer coatings with enhanced wettability switching,” *Langmuir*, vol. 24, no. 8, pp. 4238–4244, 2008. [3](#)
- [11] E. W. Edwards, M. Chanana, D. Wang, and H. Mohwald, “Stimuli-responsive reversible transport of nanoparticles across water/oil interfaces,” *Angew. Chem. Int. Ed. Engl.*, vol. 47, no. 2, pp. 320–323, 2008. [3](#)

REFERENCES

- [12] M. M. Yallapu, J. K. Vasir, T. K. Jain, S. Vijayaraghavalu, and V. Labhasetwar, "Synthesis, characterization and antiproliferative activity of rapamycin-loaded poly(n-isopropylacrylamide)-based nanogels in vascular smooth muscle cells," *J. Biomed. Nanotechnol.*, vol. 4, no. 1, pp. 16–24, 2008. 3
- [13] I. C. Kwon, Y. H. Bae, and S. W. Kim, "Electrically erodible polymer gel for controlled release of drugs," *Nature*, vol. 354, no. 6351, pp. 291–293, 1991. 3
- [14] M. K. Krusic, M. Ilic, and J. Filipovic, "Swelling behaviour and paracetamol release from poly(n-isopropylacrylamide-itaconic acid) hydrogels," *Polymer Bulletin*, vol. 63, no. 2, pp. 197–211, 2009. 3
- [15] A. Chilkoti, M. R. Dreher, D. E. Meyer, and D. Raucher, "Targeted drug delivery by thermally responsive polymers," *Adv. Drug Delivery Rev.*, vol. 54, no. 5, pp. 613–630, 2002. 3
- [16] Y. S. Park, Y. Ito, and Y. Imanishi, "Permeation control through porous membranes immobilized with thermosensitive polymer," *Langmuir*, vol. 14, no. 4, pp. 910–914, 1998. 3
- [17] V. Lapeyre, N. Renaudie, J.-F. Dechezelles, H. Saadaoui, S. Ravaine, and V. Ravaine, "Multiresponsive hybrid microgels and hollow capsules with a layered structure," *Langmuir*, vol. 25, no. 8, pp. 4759–4766, 2009. 3
- [18] L. Ionov, M. Stamm, and S. Diez, "Reversible switching of microtubule motility using thermoresponsive polymer surfaces," *Nano Lett.*, vol. 6, no. 9, pp. 1982–1987, 2006. 3
- [19] Y. Yang, X. Yan, Y. Cui, Q. He, D. Li, A. Wang, J. Fei, and J. Li, "Preparation of polymer-coated mesoporous silica nanoparticles used for cellular imaging by a "graft-from" method," *J. Biomed. Nanotechnol.*, vol. 18, no. 47, pp. 5731–5737, 2008. 3
- [20] H. E. Canavan, X. Cheng, D. J. Graham, B. D. Ratner, and D. G. Castner, "A plasma-deposited surface for cell sheet engineering: Advantages over mechanical dissociation of cells," *Plasma Processes Polym.*, vol. 3, no. 6-7, pp. 516–523, 2006. 3
- [21] T. Matsuda, "Poly(n-isopropylacrylamide)-grafted gelatin as a thermoresponsive cell-adhesive, mold-releasable material for shape-engineered tissues," *J. Biomater. Sci., Polym. Ed.*, vol. 15, pp. 947–955, 2004. 3
- [22] A. Kushida, M. Yamato, C. Konno, A. Kikuchi, Y. Sakurai, and T. Okano, "Decrease in culture temperature releases monolayer endothelial cell sheets together with deposited fibronectin matrix from temperature-responsive culture surfaces," *J. Biomed. Mater. Res.*, vol. 45, pp. 355–362, 1999. 3
- [23] T. Takezawa, Y. Mori, and K. Yoshizato, "Cell culture on a thermo-responsive polymer surface," *Nat. Biotechnol.*, vol. 8, pp. 854–856, 1990. 3

REFERENCES

- [24] S. Balamurugan, L. K. Ista, J. Yan, G. P. Lopez, J. Fick, M. Himmelhaus, and M. Grunze, “Reversible protein adsorption and bioadhesion on monolayers terminated with mixtures of oligo(ethylene glycol) and methyl groups,” *J. Am. Chem. Soc.*, vol. 127, no. 42, pp. 14548–14549, 2005. [3](#)
- [25] H. Yim, M. S. Kent, S. Mendez, G. P. Lopez, S. Satija, and Y. Seo, “Effects of grafting density and molecular weight on the temperature-dependent conformational change of poly(n-isopropylacrylamide) grafted chains in water,” *Macromolecules*, vol. 39, no. 9, pp. 3420–3426, 2006. [3](#)
- [26] S. Schmidt, H. Motschmann, T. Hellweg, and R. von Klitzing, “Thermoresponsive surfaces by spin-coating of pnipam-co-paa microgels: A combined afm and ellipsometry study,” *Polymer*, vol. 49, no. 3, pp. 749–756, 2008. [3](#)
- [27] F. Montagne, J. Polesel-Maris, R. Pugin, and H. Heinzelmann, “Poly(n-isopropylacrylamide) thin films densely grafted onto gold surface: Preparation, characterization, and dynamic afm study of temperature-induced chain conformational changes,” *Langmuir*, vol. 25, no. 2, pp. 983–991, 2009. [3](#)
- [28] N. Ishida and S. Biggs, “Direct observation of the phase transition for a poly(n-isopropylacrylamide) layer grafted onto a solid surface by afm and qcm-d,” *Langmuir*, vol. 23, no. 22, pp. 11083–11088, 2007. [3](#)
- [29] C. D. Bain, “Studies of adsorption at interfaces by optical techniques: ellipsometry, second harmonic generation and sum-frequency generation,” *Curr. Opin. Coll. Interface Sci.*, vol. 3, pp. 287–292, 1998. [4](#)
- [30] Z. Chen, Y. R. Shen, and G. A. Somorjai, “Studies of polymer surfaces by sum frequency generation vibrational spectroscopy,” *Annu. Rev. Phys. Chem.*, vol. 53, pp. 437–465, 2002. [4](#)
- [31] G. L. Richmond, “Molecular bonding and interactions at aqueous surfaces as probed by vibrational sum frequency spectroscopy,” *Chem. Rev.*, vol. 102, pp. 2693–2724, 2002. [4](#)
- [32] M. B. Raschke and Y. R. Shen, “Nonlinear optical spectroscopy of solid interfaces,” *Curr. Opin. Solid State Mater. Sci.*, vol. 8, pp. 343–352, 2004. [4](#)
- [33] F. Vidal and A. Tadjeddine, “Sum-frequency generation spectroscopy of interfaces,” *Rep. Prog. Phys.*, vol. 68, pp. 1095–1127, 2005. [4](#)
- [34] K. B. Eisenthal, “Second harmonic spectroscopy of aqueous nano- and microparticle interfaces,” *Chem. Rev.*, vol. 106, pp. 1462–1477, 2006. [4](#)
- [35] S. Gopalakrishnan, D. F. Liu, H. C. Allen, M. Kuo, and M. J. Shultz, “Vibrational spectroscopic studies of aqueous interfaces: Salts, acids, bases, and nanodrops,” *Chem. Rev.*, vol. 106, pp. 1155–1175, 2006. [4](#)

REFERENCES

- [36] Y. R. Shen and V. Ostroverkhov, “Sum-frequency vibrational spectroscopy on water interfaces: Polar orientation of water molecules at interfaces,” *Chem. Rev.*, vol. 106, pp. 1140–1154, 2006. [4](#)
- [37] F. M. Geiger, “Second harmonic generation, sum frequency generation, and $\chi^{(3)}$: Dissecting environmental interfaces with a nonlinear optical swiss army knife,” *Annu. Rev. Phys. Chem.*, vol. 60, pp. 61–83, 2009. [4](#)
- [38] H. Arnolds and M. Bonn, “Ultrafast surface vibrational dynamics,” *Surf. Sci. Rep.*, vol. 65, pp. 45–66, 2010. [4](#)
- [39] X. H. Cheng, H. E. Canavan, M. J. Stein, J. R. Hull, S. J. Kveskin, M. S. Wagner, G. A. Somorjai, D. G. Castner, and B. D. Ratner, “Surface chemical and mechanical properties of plasma-polymerized n-isopropylacrylamide,” *Langmuir*, vol. 21, no. 17, pp. 7833–7841, 2005. [4](#)
- [40] T. Miyamae, H. Akiyama, M. Yoshida, and N. Tamaoki, “Characterization of poly(n-isopropylacrylamide)-grafted interfaces with sum-frequency generation spectroscopy,” *Macromolecules*, vol. 40, no. 13, pp. 4601–4606, 2007. [4](#)
- [41] R. L. Townsin, “The ship hull fouling penalty,” *Biofouling*, vol. 19, pp. 9–15, 2003. [5](#)
- [42] M. P. Schultz, “Effects of coating roughness and biofouling on ship resistance and powering,” *Biofouling*, vol. 23, pp. 331–341, 2007. [5](#)
- [43] J. D. Andrade and V. Hlady, “Protein adsorption and materials biocompatibility: A tutorial review and suggested hypotheses,” *Adv. Polym. Sci.*, vol. 79, pp. 1–63, 1986. [6](#)
- [44] S. Jeon, J. Lee, J. Andrade, and P. D. Gennes, “Protein–surface interactions in the presence of polyethylene oxide: I. simplified theory,” *J. Colloid Interface Sci.*, vol. 142, no. 1, pp. 149–158, 1991. [6](#)
- [45] S. Jeon and J. Andrade, “Protein–surface interactions in the presence of polyethylene oxide: Ii. effect of protein size,” *J. Colloid Interface Sci.*, vol. 142, no. 1, pp. 159–166, 1991. [6](#)
- [46] C. Dicke and G. Hähner, “Interaction between a hydrophobic probe and tri(ethylene glycol)-containing self-assembled monolayers on gold studied with force spectroscopy in aqueous electrolyte solution,” *J. Phys. Chem. B*, vol. 106, pp. 4450–4459, 2002. [6](#)
- [47] C. Dicke and G. Hähner, “ph-dependent force spectroscopy of tri(ethylene glycol)- and methyl-terminated self-assembled monolayers adsorbed on gold,” *J. Am. Chem. Soc.*, vol. 124, pp. 12619–12625, 2002. [6](#)
- [48] R. L. C. Wang, H. J. Kreuzer, and M. Grunze, “The interaction of oligo(ethylene oxide) with water: a quantum mechanical study,” *Phys. Chem. Chem. Phys.*, vol. 2, no. 16, pp. 3613–3622, 2000. [6](#)

REFERENCES

- [49] R. L. C. Wang and H. J. Kreuzer, “Molecular conformation and solvation of oligo(ethylene glycol)-terminated self-assembled monolayers and their resistance to protein adsorption,” *J. Phys. Chem. B*, vol. 101, pp. 9769–9773, 1997. [6](#)
- [50] A. J. Pertsin and M. Grunze, “Computer simulations of water near the surface of oligo(ethylene glycol)-terminated alkanethiols self-assembled monolayers,” *Langmuir*, vol. 16, pp. 8829–8841, 2000. [xi](#), [6](#), [7](#)
- [51] R. Begum and H. Matsuura, “Conformational properties of short poly(oxyethylene) chains in water studied by ir spectroscopy,” *J. Chem. Soc., Faraday Trans.*, vol. 93, pp. 3839–3848, 1997. [7](#)
- [52] M. W. A. Skoda, R. M. J. Jacobs, J. Willis, , and F. Schreiber, “Hydration of oligo(ethylene glycol) self-assembled monolayers studied using polarization modulation infrared spectroscopy,” *Langmuir*, vol. 23, pp. 970–974, 2007. [7](#)
- [53] G. D. Smith, D. Y. Yoon, R. L. Jaffe, R. H. Colby, R. Krishnamoorti, and L. J. Fetters, “Conformations and structures of poly(oxyethylene) melts from molecular dynamics simulations and small-angle neutron scattering experiments,” *Macromolecules*, vol. 29, pp. 3462–3469, 1996. [7](#)
- [54] L. Dreesen, C. Humbert, P. Hollander, A. A. Mani, K. Ataka, P. A. Thiry, and A. Peremans, “Study of the water/poly(ethylene glycol) interface by ir-visible sum-frequency generation spectroscopy,” *Chem. Phys. Lett.*, vol. 333, no. 5, pp. 327–331, 2001. [7](#)
- [55] E. L. Hommel, J. K. Merle, G. Ma, C. M. Hadad, and H. C. Allen, “Spectroscopic and computational studies of aqueous ethylene glycol solution surfaces,” *J. Phys. Chem. B*, vol. 109, pp. 811–818, 2005. [7](#)
- [56] M. A. Even, C. Chen, J. Wang, and Z. Chen, “Chemical structures of liquid poly(ethylene glycol)s with different end groups at buried polymer interfaces,” *Macromolecules*, vol. 39, no. 26, pp. 9396–9401, 2006. [7](#)

2

Methods

2.1 Fourier Transform Infrared reflection adsorption spectroscopy (FT-IRRAS)

FT-IRRAS is a vibrational spectroscopic technique used for the pre characterization of the samples investigated in this work. The IR radiation adsorbed by the molecules is measured as function of wavelength.

Vibrational resonances of the chemical bounds have their eigenfrequencies in the infrared regime. Certain molecular vibrational modes couple with infrared radiation and exchange energy when the frequencies are in resonance. In an infrared experiment, the intensity of a beam of infrared radiation is measured before and after its interaction with the sample. Plotting the ratio of both intensities versus frequency gives information about the identities, surrounding environments and concentration of the chemical bonds.

IRRAS is a special type of IR spectroscopy, in which the radiation gets reflected onto the surface to probe an adsorbed thin film. Generally, metallic substrates are used in order to obtain highly reflective surfaces.

A simple way of describing molecules is as point masses connected by spring forces. It can be assumed that the involved atoms are following Hooks law, where the reset force F is linearly related to the deflection of the atoms from the rest position. The corresponding potential $V(r)$ is quadratic:

$$F = -k \cdot r; \quad V(r) = \frac{1}{2} \cdot kr^2 \quad (2.1)$$

2. METHODS

where the spring constant k is a measure of the bond strength between atoms separated by the distance r and holds specific information of the molecule.

Since these motions are on a microscopic scale, a quantum mechanical description is necessary. The possible energy eigenvalues E of the vibrational modes follow the Schrödinger equation:

$$H\psi(r) = E\psi(r); \quad H = \frac{\hat{p}^2}{2m} + V(r) \quad (2.2)$$

and the energy eigenvalues E_n of the vibrations of the simple harmonic oscillator are:

$$E_n = (n + \frac{1}{2})h\nu \quad (2.3)$$

where $h = 6.62610^{-34}$ Js is the Planck constant, ν the frequency and $n \in \{0, 1, 2, \dots\}$ the vibration quantum number. For a simple molecule of two atoms with mass m_1 and m_2 follows:

$$\nu = \frac{1}{2\pi} \sqrt{\frac{k}{\mu}} \quad (2.4)$$

with the reduced mass $\mu = \frac{m_1 m_2}{m_1 + m_2}$.

For IR spectroscopy, the selection rules indicate whether a molecule can be excited from one particular eigenstate to another. The dipole momentum μ in a molecule needs to be changed during the vibration. The intensity of an IR absorption band I_{IR} depends on the change of the dipole moment μ during this vibration:

$$I_{IR} \propto \left(\frac{\partial \mu}{\partial q} \right)^2 \quad (2.5)$$

where q is the normal coordinate.

The usual type of IR spectrometer, the type used in this work, is an FTIR spectrometer where a Michelson interferometer is applied. An IR laser beam is split and later recombined on the sample. While the beams are split they travel different distances, so that there is both a retardation γ and a phase difference $\delta\phi = \frac{\omega\gamma}{c}$.

A monochromatic light source will give constructive interference when $\gamma = n\lambda$, with ($n = 0, 1, 2, \dots$) and destructive interference when $\gamma = (n + \frac{1}{2})\lambda$.

For a broad band light source, constructive interference is at different optical retardation. Obviously the light of every wavelength interferes constructively if the optical retardation is zero. For the relation of the intensity with the retardation in general:

$$I(\gamma) = \int_{-\infty}^{+\infty} \frac{1}{2} P(\lambda) \left[1 + \cos \left(2\pi \frac{\gamma}{\lambda} \right) \right] d\lambda \quad (2.6)$$

with $P(\lambda)$: intensity of the light source

The spectral information is inside the argument of the cosine. This interferogram needs to be inversely Fourier transformed to obtain the spectrum:

$$S(\nu) = \int_{-\infty}^{+\infty} I(\gamma) \exp(-2i\pi\nu\gamma) d\gamma \quad (2.7)$$

Since both the sample and the light source are contributing to the resulting spectrum, a reference spectrum $I_0(\nu)$ is usually recorded as well. The absorption $A(\nu)$ and transmission spectrum $T(\nu)$ are then calculated:

$$A(\nu) = \log \frac{I_0(\nu)}{I(\nu)} = -\log \frac{I(\nu)}{I_0(\nu)} = -\log T(\nu) \quad (2.8)$$

The spectrometer used for the data in this work was a Vertex 70 from Bruker using p-polarized light and a liquid nitrogen cooled mercury cadmium telluride (MCT) detector. The variable angle reflection IRRAS sample stage was usually adjusted to 70 ° incident angle.

2.2 Raman Spectroscopy

Raman spectroscopy measures the inelastic light scattering that results from the excitation of vibrations in molecular and crystalline materials as a function of wavelength.

An intense monochromatic light beam impinges on the sample. The electric field of the incident radiation distorts the electron clouds of the chemical bonds and stores some energy. The distorted electron clouds relax and the stored energy is radiated mostly at the same frequency as the incident light. This is called Rayleigh scattering. A small portion of the stored energy is transferred to the sample itself and excites vibrational resonances. The energy of these excitations is deducted from the energy of the incident beam, resulting in the appearance of weak side bands, called Raman lines. This process is called Stokes scattering. On the other hand already existing thermally

2. METHODS

excited vibrations are annihilated by coupling with the incident beam. Both energies will add up. This process is called anti-Stokes scattering and is rarely measured, except for in the case of coherent anti-Stokes Raman spectroscopy (CARS). The intensity ratio of Stokes and anti-Stokes depends only on the number of molecules in each particular energy state, which is given by the Boltzmann distribution.

$$\frac{N_1}{N_0} = \frac{g_1}{g_0} \exp\left(-\frac{\Delta E_\nu}{kT}\right) \quad (2.9)$$

with N_0 number of molecules in the lower vibrational state and N_1 higher ones, g_0 the degeneracy of the lower state and g_1 higher state respectively, ΔE_ν the energy difference and k the Boltzmann constant.

One advantage of the Raman process, in contrast to IR spectroscopy, is that the exciting and emitting laser beam are in wavelength regions where the ambient atmosphere does not have any absorption bands. This makes the instrumentation in labs much simpler since purging with nitrogen or dry air is not necessary. Also, the emitted beam from the sample can be analyzed with a grating, which diffracts the beam on a CCD, which does not need liquid nitrogen cooling.

Analytically, the main difference between Raman IR spectroscopy is the complementary spectral activity of the Raman transition. Here it is not the change in the dipole moment, but it is the change of polarizability α with respect to the normal coordinate Q of the vibration.

$$\left|\frac{\partial\alpha}{\partial Q}\right| > 0 \quad (2.10)$$

Raman spectra in this work were recorded using a confocal microscope laser Raman system (Labram I, Horiba Jobin Yvon) with a cw argon gas laser with 15 mW at 512 nm.

2.3 Sum-frequency generation Spectroscopy (SFG)

The investigation of molecular behavior at solid interfaces *in situ* is of significant interest in the field of surface science, particularly in such issues as the development of biocompatible materials and material coatings, as well as a furthering of the knowledge of basic surface chemistry and physics.[1, 2, 3, 4] Recently, the technique of sum-frequency-generation (SFG) spectroscopy has emerged as a tool particularly well-suited

2.3 Sum-frequency generation Spectroscopy (SFG)

to this task, due to its surface sensitivity, molecular-level detection, and ability to function under standard conditions.[5, 6, 7] SFG spectroscopy has been previously applied to the investigation of various materials at the gas/solid interface,[8] the gas/liquid interface, [9, 10, 11] and the liquid/liquid interface.[12, 13] However, applications of this technique to solid/liquid interfaces have been fewer in number,[14] due at least in part to the difficulties associated with the more complex sample stage geometry required.

The first approaches to overcoming these difficulties consisted of probing the solid/liquid interface in a setup where the solid itself was a flat window of optically transparent material.[15, 16, 17, 18, 19] This approach has yielded valuable information about the adsorption of polyelectrolyte solutions,[15] the behavior of water at the α -quartz interface at various pH values,[16] the conformation of liquid poly(ethylene glycol) in contact with solid polymers,[17] and the adsorption of amino acids at hydrophobic and hydrophilic interfaces.[18]

Recent measurements made by York *et al.* at the polystyrene/air interface demonstrated that signal strength in SFG spectra was enhanced when the incoming beams were directed through a prism instead of a flat window. This enhancement of the SFG signal is usually found by having one of the incident beams near the total internal reflection (TIR) condition.[20] However, it was also shown that the SFG intensity is strongly influenced by the dispersion of the absorptive medium and that care must be taken in the quantitative analysis of the SFG experimental data.[21] Nevertheless, the former geometry had been previously used by Becraft and Richmond in their SFG investigations of water orientation at the $\text{CaF}_2/\text{H}_2\text{O}$ interface,[22] as well as by Hayes *et al.* in their second-harmonic-generation (SHG) studies of metal cations at the fused quartz/ H_2O interface.[23]

However, all of the methods used in the above-mentioned studies require that the solid surface be both visible (VIS)- and IR-transparent. Furthermore, when investigating thin films, it is necessary that the molecules of interest be immobilizable on this transparent surface, which is not the situation in many interesting phenomena at the solid/liquid interface. Stein *et al.* worked to overcome this limitation by probing through the backside of a fused silica window coated with a 20 nm layer of gold and covered with self-assembled monolayers (SAMs) of alkanethiols or ethylene glycols.[24] Using this setup, they were able to successfully quantify the percentage of water retained in these films. However, previous works characterizing the synthesis of very thin

2. METHODS

metal films have shown that achieving a fully closed film of such thickness is no trivial task,[25, 26] and that surface roughness stemming from incomplete film formation can complicate the interpretation of the obtained SFG spectra.[25] Furthermore, using thin metal films increases the risk of total film ablation if the intensity of the incoming beams is not carefully monitored and controlled. Later in this work a thin-layer analysis (TLA) cell is presented which solves the problems of being limited to transparent substrates or very thin metal films, offering the ability to probe the solid/liquid interface on any opaque and suitably reflective substrate.

2.3.1 SFG theory

Resonant vibrational SFG is a two photon process. The first photon is absorbed by resonantly exciting a molecular vibration and the second photon annihilates this particular vibration in an anti-Stokes process. Therefore the energy and momentum of the generated photon is the sum of both incoming photons. The energy diagram is shown in Fig.2.1

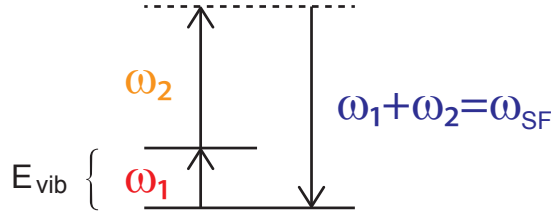


Figure 2.1: Energy diagram - SFG process

A closer look at this frequency mixing process starts with the induced polarization. The external electric field applies a polarization to the material and will displace electron clouds relative to the nucleus and create induced dipoles. The response of a material to the field is the amount N of dipole moments μ per volume V or polarization $P = N \frac{\langle \mu \rangle}{V}$. In the case of weak electric fields, the polarization is proportional to the field strength E :

$$P^{(1)}(\omega) = \epsilon_0 \chi^{(1)} E(\omega) \quad (2.11)$$

$\chi^{(1)}$ is the linear susceptibility.

2.3 Sum-frequency generation Spectroscopy (SFG)

For strong electric fields the polarization is no longer proportional to the field strength. The laser pulses used in this thesis have about $E_{pulsedlaser} \sim 10^{10} - 10^{15} \text{ V/m}$. The electric field of a hydrogen atom is $E_{atom} \leq \frac{e}{4\pi\epsilon_0 r_0^2} \approx 10^8 \text{ V/m}$ and the field of the sunlight on earth is about $E_{sun} \approx 10 \text{ V/m}$. In general the polarization can be expanded in a Taylor series:

$$P(\omega) = \epsilon_0 \left(\chi^{(1)} E(\omega) + \chi^{(2)} E^2(\omega) + \chi^{(3)} E^3(\omega) + \dots \right) \quad (2.12)$$

with $\chi^{(2)}$ the second order and $\chi^{(3)}$ the third order nonlinear susceptibility. As described in Eqn. 2.1 electron-atom interactions can be described with a spring model where the response is linear. This is true for $E \ll E_{atom}$ but as soon as $E \geq E_{atom}$ the potential becomes different from the simple parabolic harmonic potential. A realistic anharmonic potential is shown in Fig. 2.2. For weak incident fields, the induced polarization is proportional to the incident field. In the case of higher field amplitudes, however, the corresponding polarization is biased and can be separated with Fourier series expansion in components of various frequencies.

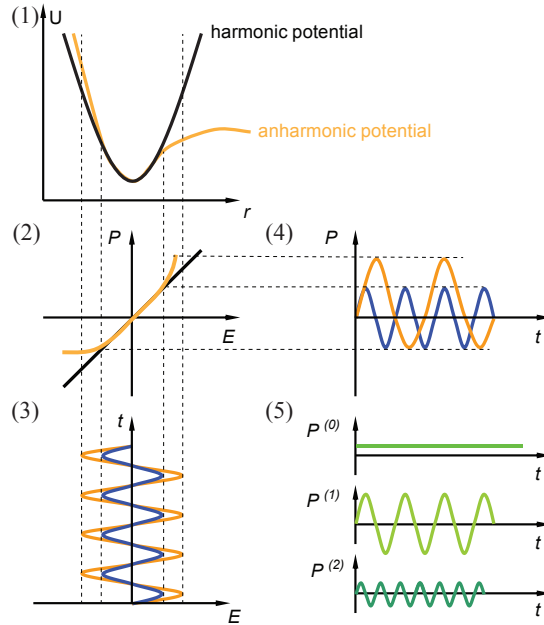


Figure 2.2: Scheme of nonlinear polarizability - (1) the anharmonic potential (2) induced polarization as function of incident field (3) weak incident field (blue), strong incident field (orange) (4) polarization response as function of time (5) Fourier series expansion of response function

2. METHODS

In the case of two incident laser beams overlapping in space and time at an interface with the susceptibility χ the second-order nonlinear polarization $\mathbf{P}^{(2)}$ is given by:

$$\mathbf{P}^{(2)} = \varepsilon_0 \chi^{(2)} : \mathbf{E}_{IR} \mathbf{E}_{VIS} = \varepsilon_0 \chi^{(2)} \begin{bmatrix} 2(E_1 E_1^*) \\ + E_1^2 \exp(-2i\omega_1 t) \\ + E_2^2 \exp(-2i\omega_2 t) \\ + 2E_1 E_2^* \exp(-i(\omega_1 - \omega_2)t) \\ + 2E_1 E_2^* \exp(-i(\omega_1 + \omega_2)t) \end{bmatrix} \quad (2.13)$$

where ε_0 is the vacuum permittivity (8.854×10^{-12} C/V.m), $\chi^{(2)}$ is the second-order nonlinear susceptibility, a 3rd rank tensor, and \mathbf{E}_{IR} and \mathbf{E}_{VIS} are the incoming electric fields of the IR and VIS beams, respectively. The nonlinear effects of optical rectification, second-harmonic ($2\omega_1$ and $2\omega_2$), difference-frequency ($\omega_1 - \omega_2$) and sum-frequency ($\omega_1 + \omega_2$) generation are appearing. In this work, only SFG is considered. The other effects are also important, e.g. for the generation of the tunable IR light, but will not be used for analysis.

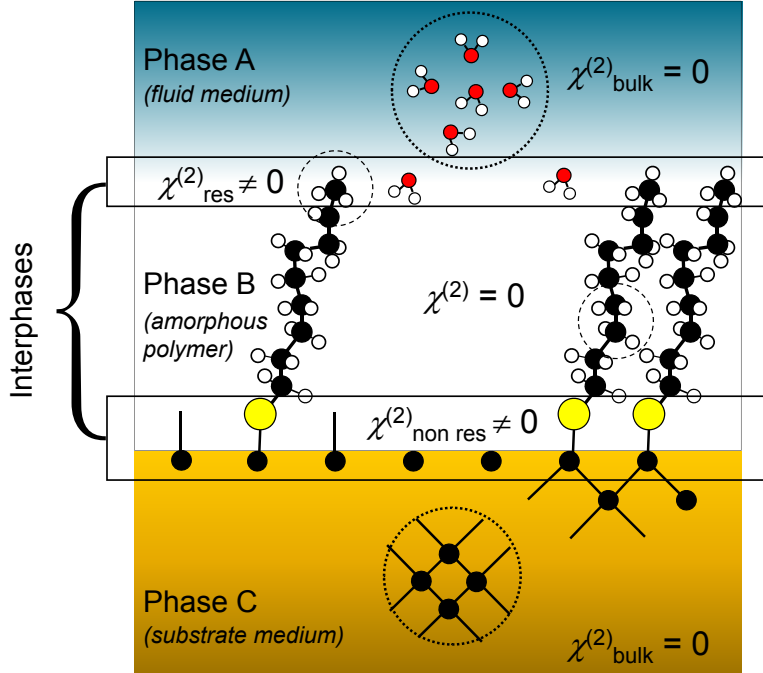


Figure 2.3: Scheme of a typical sample composition - only the interfaces with $\chi^{(2)} \neq 0$ give rise to an SFG signal.

According to the Neumann principle, the point group symmetry of any physical property of a system is the same as the system itself. If we assume a system with

2.3 Sum-frequency generation Spectroscopy (SFG)

inversion symmetry, this means that the second order susceptibility tensor needs to be invariant upon applying the parity operator P , so $P(\chi^{(2)}(\vec{r})) = \chi^{(2)}(\vec{r})$ with $P : X^i \rightarrow -X^i$. Also $\chi^{(2)}$ is a polar tensor with $\chi^{(2)}(\vec{r}) = -\chi^{(2)}(-\vec{r})$. Therefore the equation $\chi^{(2)}(-\vec{r}) = -\chi^{(2)}(\vec{r})$ needs to be satisfied for such a system with inversion symmetry. The only solution is $\chi^{(2)} = 0$. When inversion symmetry is present, no second order nonlinear processes occur and therefore there is SF generation. At interfaces or in some crystals the centrosymmetry is broken and SF signals can be generated. Fig. 2.3 show an example of a typical sample and highlights the regions where SFG will be generated.

Quantitatively, the SFG amplitude of the q th resonance is depending on the product of the IR transition dipole moment $\partial\mu/\partial Q_q$ and the Raman polarizability $\partial\alpha/\partial Q_q$:

$$\beta_{q,ijk} = -\frac{N_s}{\epsilon_0} \sum_{i'j'k'} \frac{1}{2\omega_q} \frac{\partial\alpha_{i'j'}}{\partial Q_q} \frac{\partial\mu_{k'}}{\partial Q_q} \langle (\hat{i} \cdot \hat{i}')(\hat{j} \cdot \hat{j}')(\hat{k} \cdot \hat{k}') \rangle \quad (2.14)$$

where N_s is the surface density of molecules, Q_q is the classical normal coordinate of the q th vibrational mode, and $\hat{i}, \hat{j}, \hat{k}$ are the laboratory coordinates which are transformed into $\hat{i}', \hat{j}', \hat{k}'$, the molecular coordinates.[27] The orientation of surface groups such as methyl, methylene, C=O, and OH can be determined by either *ssp*, *ppp*, and *sps* SFG spectra, experiments with swept incident angle, or by turning the molecular angle stepwise. Methyl and methylene angular information can also be obtained by the ratio of symmetric and asymmetric resonances. All different components of the molecular hyperpolarizability tensor β can be related to the laboratory coordinate system hyperpolarizability $\chi^{(2)}$. Information about the orientation of methyl groups has largely been collected using this approach. In chapter 4 further explanations about SFG intensity and simulations of the SFG spectra are presented.

2.3.2 SFG spectrometer

The generation of nonlinear signals from interfacial molecules requires high intensity laser light sources. Therefore, picosecond (ps) and femtosecond (fs) laser setups are most often used in SFG spectroscopy.[28] Ps-based systems usually have a large scanning range ($\sim 1000 \text{ cm}^{-1}$) with a spectral acquisition time on the order of tens of minutes. A ps-based laser system is tuned within a certain frequency range and an SFG signal is recorded by integrating the intensity at each frequency. Broadband SFG spectrometers based on fs tunable laser systems are conceptually different. In these, the broad SFG

2. METHODS

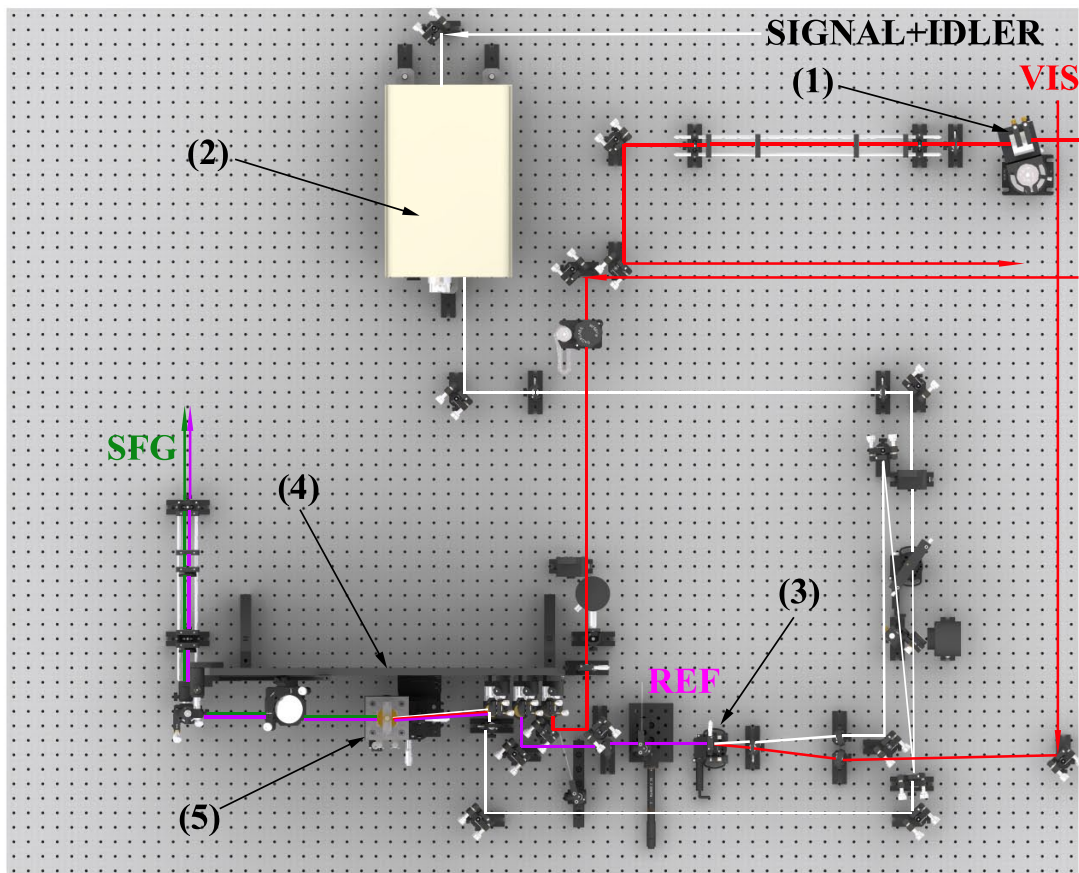


Figure 2.4: Top view image of the optical layout of the broadband SFG system after the OPA - (1) Fabry-Perot etalon, (2) NDFG, (3) nonlinear SF generating crystal for the reference line, (4) vertical breadboard, and (5) sample stage. The IR, REF, SFG, and VIS beams are represented by white, purple, green, and red solid lines, respectively.

2.3 Sum-frequency generation Spectroscopy (SFG)

signal is imaged through a spectrometer. This setup allows the detection of SFG signals in a narrower spectral range ($\sim 70\text{-}200\text{ cm}^{-1}$) with temporal resolution usually on the order of seconds. The sample cell presented in Sec. 2.3.2.3 can be used for both ps and fs SFG spectrometers. Dynamic processes on time scales from seconds to minutes are accessible to both type of systems. However, kinetic measurements obtained by ps systems are restricted to one fixed frequency,[29] while fs systems can record a spectral range.

Our fs SFG spectrometer setup is based on a broad bandwidth scheme.[30] It consists of a fs regenerative amplifier (RGA) (Spitfire Pro 35F XP, Spectra-Physics; sub-35 fs, 1 kHz) seeded by a mode-locked Ti:sapphire oscillator (Tsunami 3941-MS, Spectra-Physics; sub-30 fs, 80 MHz) with a tunable wavelength centered at 800 nm. The regenerative amplifier and seed laser are pumped by frequency-doubled Q-switched Nd:YLF (Empower 30, Spectra-Physics; 30 W, 1 kHz, 527 nm) and Nd:YVO₄ (Millenia Pro 5s, Spectra-Physics; 5 W, 532 nm) solid-state lasers, respectively. The RGA generates 90-fs duration pulses centered at 800 nm with a repetition rate of 1 kHz and an average power of 4 W. The amplified output beam is then split up and the larger fraction (80%) is used to pump an automated optical parametric amplifier (OPA) (TOPAS-C, Light Conversion) coupled to a non-collinear difference-frequency generator (NDFG) (Light Conversion). This generates broadband (FWHM $\sim 70\text{-}200\text{ cm}^{-1}$) IR pulses which can be tuned from 2.6 to 12 μm . The signal and idler beams are spatially separated and spectrally filtered by a Ge plate (Crystec). The remaining fraction of the output beam (20%) is fed into an air-spaced Fabry-Perot etalon (SLS Optics; spacing $d = 12.5\text{ }\mu\text{m}$, free spectral range $\text{FSR} = 398.29\text{ cm}^{-1}$, effective finesse $F_{eff} = 57.48$ at 790 nm) which gives narrowband (FWHM $\sim 1\text{ nm}$), asymmetric ps VIS pulses (see Sec. 2.3.2.1). A broadband reference (REF) beam is generated simultaneously by sum-frequency mixing of small portions of the IR ($\sim 1\%$) and VIS ($\sim 2\%$) beams in one of the following nonlinear crystals: 0.6 mm-thick LiIO₃ (2.7 - 5 μm , $\theta = 21.4^\circ$, $\phi = 0^\circ$), 0.2 mm-thick AgGaS₂ (5 - 6 μm , $\theta = 71^\circ$, $\phi = 45^\circ$), or AgGaS₂ (6 - 10 μm , $\theta = 54.4^\circ$, $\phi = 45^\circ$) (TOPAG Lasertechnik). These crystals were coated with a broadband anti-reflection coating for (800-5000) nm, 800+(5000-6000) nm, and 800+(6000-10000) nm, respectively, on the front side and (600-700) nm, (650-800) nm, and (700-800) nm, respectively, on the other side. The beam path length prior to the LiIO₃ crystal is the same as the beam path length to the sample stage. This allows for the recording of the

2. METHODS

exact spectral profile of the incident IR beam on the sample stage which can then be used for the data analysis as described in Sec. 2.3.3. Linearly polarized IR, REF, and VIS beams are independently directed and focused on the sample surface with incident angles (relative to the surface normal) of 60° , 68° and 70° , respectively (Fig. 2.4). The overall arrangement of the components on the table is shown in Fig. 2.5.

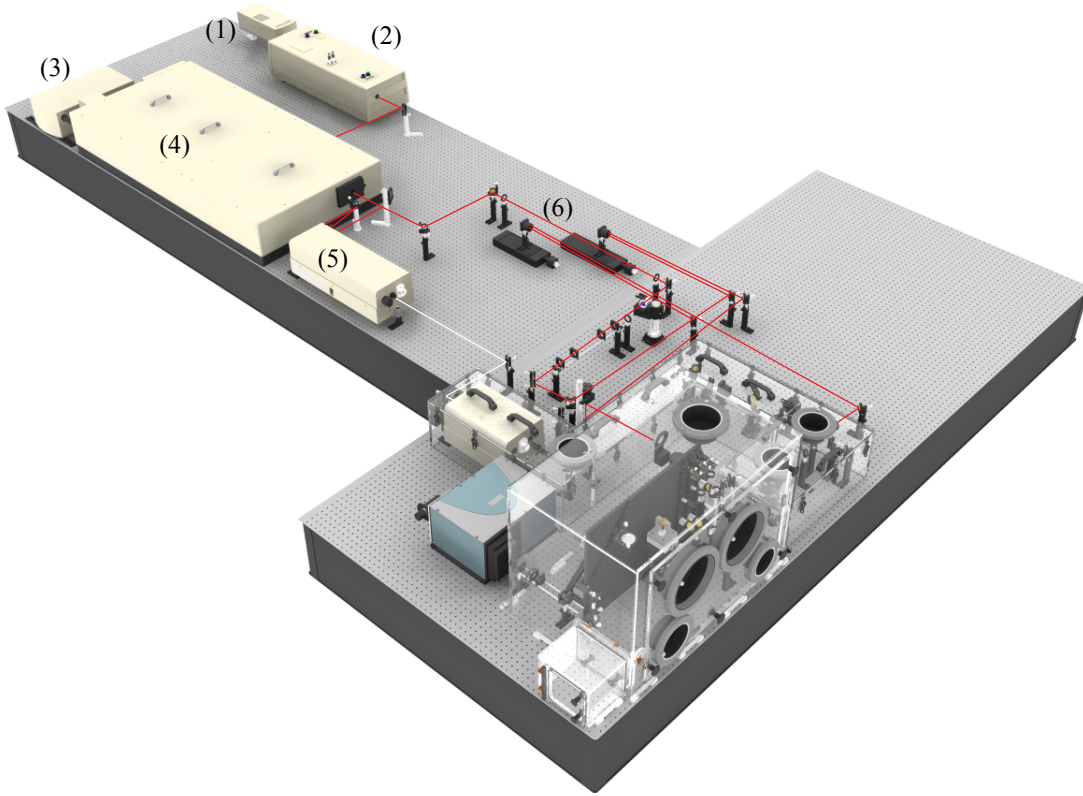


Figure 2.5: General layout of the optical table - (1) Millenia Pro, (2) Tsunami, (3) Empower, (4) Spitfire, (5) Topas, and (6) delay stages. The VIS and Signal+Idler beams are represented by red and white solid lines, respectively. For clarity the beams are only indicated until they hit the purged chamber.

A broadband SFG beam is produced when the narrowband VIS and broadband IR beams are spatially and temporally overlapped at the sample surface within a spot $\sim 200 \mu\text{m}$ in diameter. Figure 2.6 shows the beam profile of the VIS pulse at the sample. The elliptical shape is due to the incoming angle. The temporal overlap is accomplished through the use of motorized delay lines. The incidence angle of the REF beam is carefully adjusted so that on reflection it propagates collinearly with the

2.3 Sum-frequency generation Spectroscopy (SFG)

SFG beam. Maximum energies of $\sim 30 \mu\text{J}/\text{pulse}$ for the IR beam and $\sim 40 \mu\text{J}/\text{pulse}$ for the VIS beam can be obtained immediately before the sample. Usually, the energy of the incoming beams is adjusted by pinholes to prevent bubble formation or sample ablation.

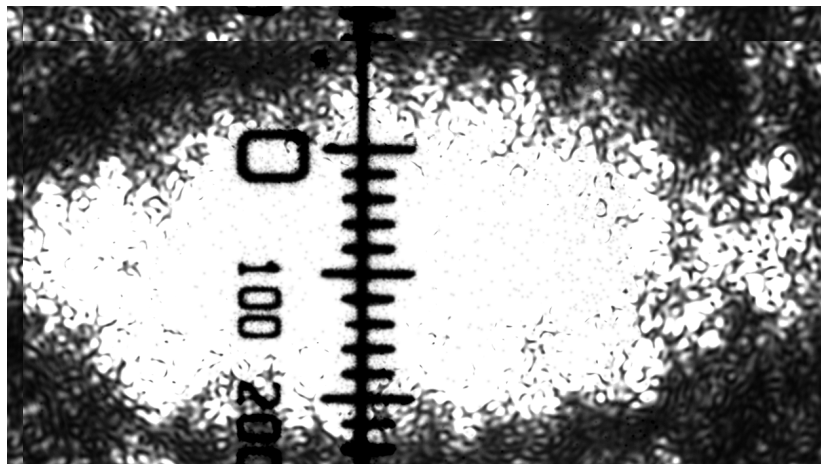


Figure 2.6: Beam profile of the VIS pulse at the sample stage - The scale shown is in μm units. This image was acquired using a microscope mounted above the sample stage of the VIS pulse hitting a piece of paper.

The intensity of the reflected REF beam is matched to that of the SFG beam using a variable neutral density filter prior to the sample. The outgoing SFG and REF beams are collimated by lenses, filtered through a short-pass filter (3rd Millennium 770SP, Laser Components), and dispersed in an imaging spectrograph (Shamrock SR-301i-B, Andor Technology; focal length $f = 303 \text{ mm}$, 1200 grooves/mm grating blazed at 500 nm) equipped with both a photomultiplier (R9110, Hamamatsu) and an air-cooled, back-illuminated high-resolution CCD camera (iDus DU420A-BR-DD, Andor Technology; 254×1024 pixels). SFG spectra with reasonable SNR are typically obtained on a time scale of ms to s. For alignment purposes, spectra can be recorded within one or two pulses, allowing real-time intensity optimization and frequency adjustment. Spectra are usually taken with an *ppp* polarization combination for the SFG, VIS, and IR beams, respectively. Other polarization combinations (*ssp*, *sps*, and *pss*) are also accessible by rotation of the IR and VIS beams through the use of half-wave plates and/or a periscope.

2. METHODS

2.3.2.1 Pulse shaping

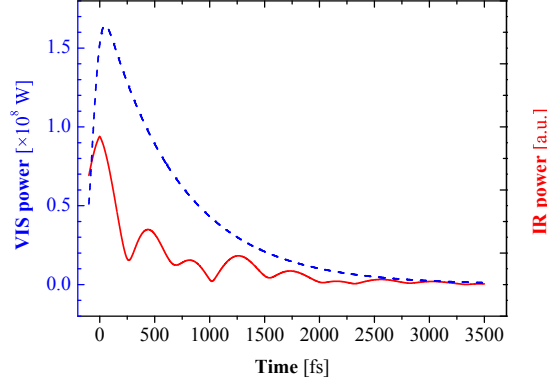


Figure 2.7: Time profile of VIS pulse - (*dashed line*) and molecular vibrations of typical CH stretches (*solid line*).

The spectral resolution of the SFG signal depends on the temporal pulse width of the VIS beam. To illustrate these dependencies, Fig. 2.7 shows a calculation of the time profile of the VIS beam (dashed line) and the resulting time profile of three typical molecular vibrations (solid line). The time profile of the molecular vibrations exceeds several ps, therefore the duration of the VIS pulse needs to be on the same order to resolve these vibrations into an SFG spectrum in the frequency domain. This pulse duration can be achieved by directing the fs VIS beam through a Fabry-Perot etalon to obtain a prolonged asymmetric time profile. For the calculation of the corresponding VIS time profile after the pulse shaper, the specifications of the etalon described in the Sec. 2.3.2 were used. The cavity lifetime τ is determined by:

$$\tau = \frac{1}{\pi \text{FSR}}. \quad (2.15)$$

To obtain an approximation of the transmitted intensity, the incoming Gaussian-shaped beam was convoluted with an exponential decay function having a time constant given by the cavity lifetime τ :^[31]

$$I_{\text{VIS,out}}(t) \approx I_{\text{VIS,in}}(t) * e^{-t\tau} \Theta(t), \quad (2.16)$$

where $I_{\text{VIS,in}}$ and $I_{\text{VIS,out}}$ are the time-dependent intensities of the VIS beam before and after the etalon, respectively. Since there is no intensity in the cavity before the

2.3 Sum-frequency generation Spectroscopy (SFG)

pulse reaches the etalon, Eq. (2.16) was weighted with the Heaviside function $\Theta(t)$. To calculate the time profile representing the polarization fields in the frequency domain three Lorentzian oscillators χ_i with equal intensities and widths of 20 cm^{-1} at 2880 , 2925 and 2945 cm^{-1} were used (solid line in Fig. 2.7). Finally, the sum of these three oscillators was Fourier-transformed into the time domain and the intensity is given by:

$$I(t) = |\mathcal{F}^{-1}(\chi_i(\omega_i))|. \quad (2.17)$$

A powerful additional application of this pulse shaping technique is background suppression. As shown in Fig. 2.3, an SF component originating from the substrate is also present. Introducing a delay to the time asymmetric pulse can filter out certain parts of the spectrum, in particular the non-resonant signal generated from the substrate. Fig. 2.8 shows how the non-resonant signal can be removed. The simulated spectrum $I(nm)$ in Fig. 2.8 (1) were calculated with:

$$I(nm) = \left| \chi_{NR} + \sum \chi_{R_i} \right|^2 \quad (2.18)$$

with a broad Gaussian shaped non-resonant

$$\chi_{NR} = A e^{-2\left(\frac{\omega_{IR} - \omega_n}{w}\right)^2} e^{i\phi_i} \quad (2.19)$$

and sharp Lorentzian resonant contributions.

$$\chi_{R_i} = \left| \frac{A_i}{(\omega_{IR} - \omega_i) + i\Gamma_i} \right| e^{i\phi_i} \quad (2.20)$$

The widths w were 14 nm and 0.7 nm for the Gaussian and the Lorentzian peaks, respectively. The phase ϕ of non-resonant was set to be $\frac{\pi}{2}$ different than the resonant contributions. By looking at the Fourier transformed spectrum it is already observable that the non-resonant contribution from metallic substrates have a very short life time of about 6 fs attributed to the electron life time of substrates like gold. This allows for the separation of the gold signal from the longer resonant contributions from e.g. CH stretching vibrations with lifetimes of about 1 ps .

Fig. 2.9 is an example of the application of this new method. Delay-dependent spectra of an alkanethiol SAM on a gold substrate (see Section. 3.2) are shown. At around 480 fs delay the non-resonant background is completely removed.

2. METHODS

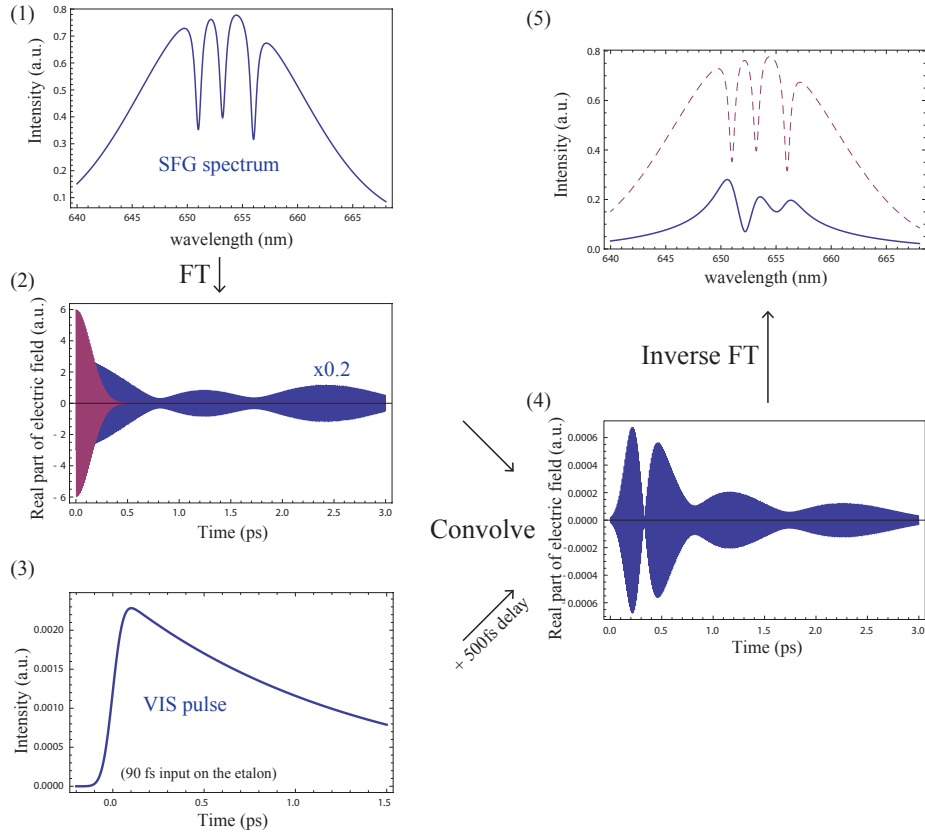


Figure 2.8: Etalons pulse shaping - (1) simulated SFG spectrum (2) Fourier transform of (1), showing the non-resonant (red) and resonant part (blue scaled by factor five) (3) etalon shaped VIS pulse as in Fig. 2.7 (4) Convolution of 500 fs shifted VIS pulse with Fourier transform of simulated spectrum (5) Inverse Fourier transformation of (4), showing the spectrum obtained with a delay shift of 500 fs (blue), and the original spectrum for direct comparison (dashed) - All graphs were calculated and plotted with Mathematica[®].

2.3 Sum-frequency generation Spectroscopy (SFG)

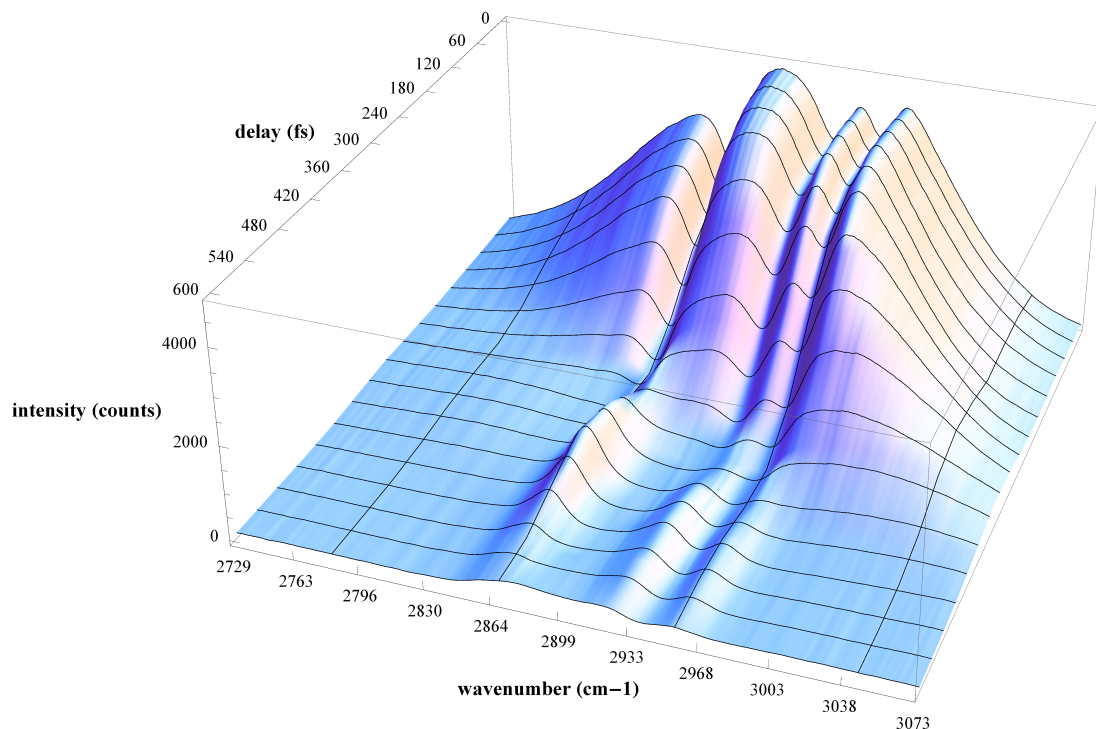


Figure 2.9: Alkane thiol ppp SFG spectrum with different time delays -

The dispersion of the IR pulse results in a frequency-dependent temporal pulse profile. The maximum of the non-resonant signal therefore occurs even before 0 fs delay on the lower wavenumber side of the spectrum, while the maximum for higher wavenumbers is up to 200 fs later. There is a dispersion of about 100 fs per 100 cm^{-1} . The possible sources of this dispersion are numerous, e.g.: lenses, windows and the Ge filter. This problem could be reduced by making all optical components in the beam path as thin as possible and/or by adding a compensator.

For the relatively simple alkanethiol SAM sample, the positions of the dips in the spectra with zero delay fit with the position of the peaks in the background removed spectra. This indicates that the relative phase ϕ between background and resonant signal is $\sim \pi$. This type of sample was usually used as a standard sample for calibrating the SFG spectrometer.

2. METHODS

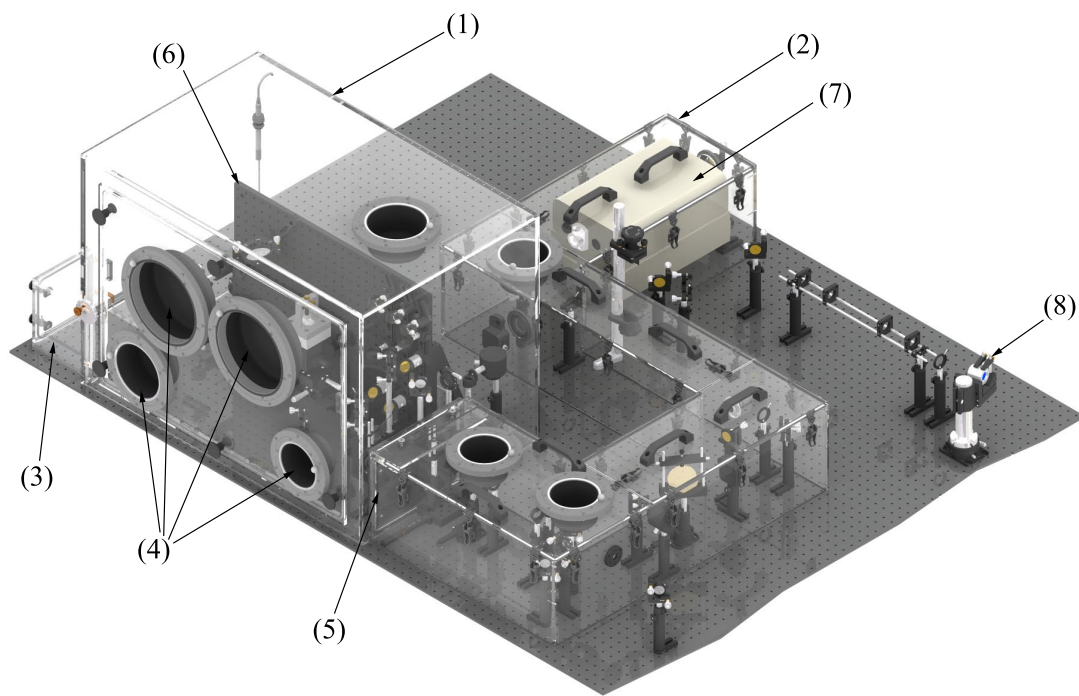


Figure 2.10: Image (isometric view) of the purging chamber - (1) main chamber, (2) channel, (3) transfer chamber, (4) Neoprene[®] gloves, (5) vertical lockable flapping door, (6) breadboard, (7) NDFG, and (8) Fabry-Perot etalon.

2.3.2.2 Purging chamber

In order to prevent IR beam absorption by ambient gaseous H_2O and CO_2 , the SFG spectrometer setup was supplemented with a home-built purging chamber (Fig. 2.10). This air-proof chamber covers the optical path of the IR beam from the NDFG module to the spectrograph. The enclosure is made entirely of acrylic glass and is divided in two sections: a four-compartment channel (volume $V \approx 0.14 \text{ m}^3$) that stretches between the NDFG and the sample stage, and a main chamber ($V \approx 0.30 \text{ m}^3$) that completely surrounds the sample stage. The channel and the chamber have built-in thin optical BaF_2 and BK7 windows (Laser Components) mounted in Teflon holders to allow entrance of OPA (signal and idler) and VIS beams, respectively. The main chamber is supplemented by a small side chamber with a lockable vertical panel permitting sample transfer without disrupting the air purge. Both channel and chamber are air-dried ($\leq 1\% \text{ RH}$) by an FTIR purging gas generator (75-45-12VDC, Parker-Balston; 14 L/min) coupled to two additional coalescing pre-filters to remove air particulates and hydrocarbon residues. The humidity and temperature in the chamber are monitored by a thermohygrometer (Hytelog-USB, Hygrosens) mounted on the top panel. When the chamber is not purged, the optical components in the channel can be accessed through removable covers, while those in the chamber can be reached by removal of the front panel. The channel and chamber can be separated from each other by a vertical lockable flapping door, keeping one compartment purged while the other is open. When the purging chamber is in operation, the mirrors important for beam alignment in the channel and the chamber can be reached externally by small Neoprene[®] gloves. The entire sample holder area (including the transfer chamber) can be accessed via two pairs of ambidextrous, fully rotatable Neoprene[®] gloves fixed directly to the front panel. All other components necessary to adjust IR and REF beam intensity (e.g. Ge plate, reference crystal, variable density filter) are motorized and remotely controlled. Two independent side panels, one on the channel and one on the chamber, provide the necessary entry ports for liquid tubes as well as for various electrical cables.

2.3.2.3 Sample stage

The sample stage is comprised of a set of input lenses and mirrors (Laser Components), a multi-axial sample holder, and a set of output mirrors (Fig. 2.11). All these

2. METHODS

components are constrained to the same plane of incidence by fixation directly on an aluminium breadboard (M4560, Thorlabs) positioned vertically on the optical table. Each input beam path consists of a lower mirror/intermediate lens/upper mirror series mounted independently on its own flexible rail system. CaF_2 (or BaF_2) lenses are used for the IR and REF beams, and BK7 lens for the VIS beam (Laser Components), respectively. The sample holder is made of a 3-axis (xyz) rolling block with manual micrometric drives (RB13M/M, Thorlabs; 13 mm travel) coupled to a 1-axis (θ) manual goniometer (GO90, Owis; $\pm 15^\circ$ rotation). The rotation axis of the goniometer is coincident with the sample surface. A pair of magnetically-coupled kinematic plates are then used to dock the measuring cells. A bottom base plate is fastened directly on top of the goniometer, while the top mounting plate is fixed to the base of the measuring cell. This system permits a quick exchange of measuring cells while the position and orientation of the probing plane is preserved. The output beam path is made of a series of three mirrors. The first mirror is larger and acts as a collector for the REF, SFG and VIS beams. It is mounted on an independent rail system that enables the operator to follow the displacement of the beams induced by the goniometer tilting. The two last mirrors guide the REF and SFG beams to the entrance slit of the spectrograph.

2.3.3 Data analysis

The intensity of the SFG signal I_{SFG} is related to the IR (I_{IR}) and the VIS (I_{VIS}) intensities by the relation:

$$\begin{aligned} I_{SFG} &\propto \left| \mathbf{P}^{(2)} \right|^2 \\ &\propto \left| \chi^{(2)} \right|^2 I_{IR} I_{VIS} \end{aligned} \quad (2.21)$$

In Eq. (2.21), $\chi^{(2)}$ consists of two different contributions: one from the substrate (non-resonant) and one from the adsorbate (resonant):[32]

$$\begin{aligned} \chi^{(2)} &= \chi_{NR}^{(2)} + \chi_R^{(2)} \\ &= \chi_{NR}^{(2)} + \sum_k \left| \frac{A_k}{(\omega_{IR} - \omega_k) + i\Gamma_k} \right| e^{i\phi_k}, \end{aligned} \quad (2.22)$$

where the non-resonant contribution $\chi_{NR}^{(2)}$ is generated by electronic interband transitions occurring within metal substrates.[33] The resonant contribution $\chi_R^{(2)}$ is generated

2.3 Sum-frequency generation Spectroscopy (SFG)

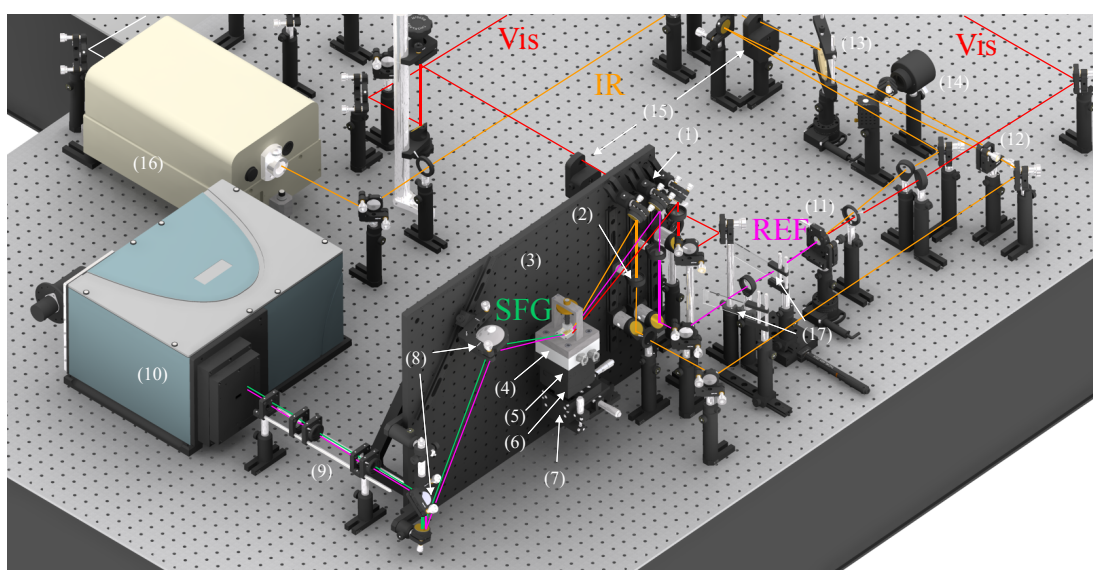


Figure 2.11: Image (isometric view) of the sample stage area (purging chamber not shown) - (1) input mirrors, (2) input lenses, (3) breadboard, (4) measuring cell, (5) kinematic plates, (6) 1-axis goniometer, (7) 3-axis rolling block, (8) output mirrors, (9) telescope, (10) spectrometer, (11) SFG crystal for REF signal, (12) BaF₂ plate as beam splitter, (13) Ge plate for filtering, (14) pyro electric IR pulse energy meter, (15) remote shutters, (16) NDFG stage, and (17) variable density filters. The IR, REF, SFG, and VIS beams are represented by orange, purple, green, and red solid lines, respectively. The reflected IR and VIS beams are not shown for clarity.

2. METHODS

from molecular vibrations and modeled as a sum of Lorentzian oscillators with amplitude A_k , resonance frequency ω_k , linewidth Γ_k , and phase difference ϕ_k relative the non-resonant contribution.

The spectral data is fitted by Eq. (2.21) using a Gaussian shape for the non-resonant signal (reflecting the fs IR profile) and Lorentzian oscillators for the resonant contributions. The phase ϕ_k depends on the metal used and delivers orientational information about adsorbed species. However, defining a correct Gaussian profile together with the resonant contributions and phases can be tedious and care needs to be taken to perform reliable data analysis. The method of removing the non-resonant background as described in section 2.3.2.1 can be useful in determining good starting values and defining boundaries for the fitting parameters. With this method, the position of the vibrational resonances can be confidently set to particular values. The width of peaks from the similar vibrational resonances e.g. the group of CH stretching vibrations, can be set to the same value for each resonance ($\sim 18 \text{ cm}^{-1}$), since their lifetimes are comparable. This drastically reduces the amount of free parameters. In order to fit the remaining parameters, an Origin script using a the Levenberg–Marquardt algorithm and a fit control allowing fixing and constraining particular parameters was used.

Most SFG spectra in this work are shown as the absolute value of the resonant parts of the $\chi^{(2)}$ tensor shown in Eqn. 2.21. The fitted non-resonant intensity is analytically removed during the data processing procedures.

The presence of a non-resonant SFG contribution can be advantageous for alignment procedures as it is generally much stronger in comparison to the resonant contributions. The total SFG signal covers about 200 cm^{-1} in a fs system. This means that broad resonant bands with widths similar to or wider than the spectral range of the IR pulse can only be detected and analyzed when the non-resonant background contribution is known. For this reason, a REF beam generated prior to the sample stage (see Sec. 2.3.2), is included in the SFG setup, which enables reliable subtraction of non-resonant background contributions for this cases. This REF beam can also be used to normalize the spectra in order to compensate for intensity drifts.

The setup described here is capable of measuring the signal and the reference beams simultaneously by recording them both on the same CCD chip. The focuses of the beams at the entrance slit are tuned with a telescope to match the f -number of the spectrometer, resulting in recorded images only a few pixels in height. The reference

2.3 Sum-frequency generation Spectroscopy (SFG)

beam is tuned to be slightly non-collinear with the signal originating from the sample allowing the separation of both signals on the CCD chip. Figure 2.12 shows the resulting image on the CCD.

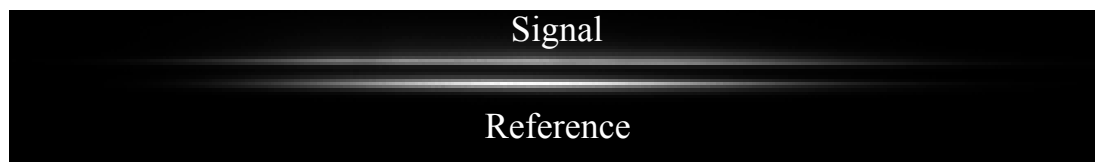


Figure 2.12: CCD image of the SFG signals from a Au sample and the reference line. -

After defining two regions of interest, one covering the sample and one the reference signal, the individual spectra are obtained by vertical binning. These spectra can then be processed in real time by a user-defined routine written for the spectrograph software (Andor SOLIS, v. 4.12) dividing the sample signal by the reference signal. Background-corrected SFG spectra are recorded and displayed at a rate of up to 30 frames/s. Videos can also be obtained for analyzing dynamic processes of interest.

2.3.3.1 Sensitivity determination

Understanding the minimum detection capabilities of a spectroscopic system is important in determining whether or not measurements of a particular sample will be useful. In order to experimentally determine the lower detection limit of our SFG system, mixed SAMs consisting of increasingly deuterated molecules were fabricated via solution deposition and measured in the CH stretching region. Details about the fabrication are in Section 3.2

SFG spectra were accumulated for 1 min, analyzed according to the procedures outline in Sec. 2.3.3, and plotted without the non-resonant background contribution. The resonant SFG intensity as a function of surface coverage of the undeuterated dodecanethiol was then calculated (Fig. 2.13). X-ray photoelectron and IR spectroscopy measurements were also performed to ensure sample quality.

The residual peaks present in the spectrum of the fully deuterated monolayer can be assigned to CH_2 vibrations and are related to incomplete deuteration. However, the peak at 2880 cm^{-1} arising from the symmetric vibrations of the terminal CH_3 group could be used to accurately assess the SFG intensity as a function of concentration, and

2. METHODS

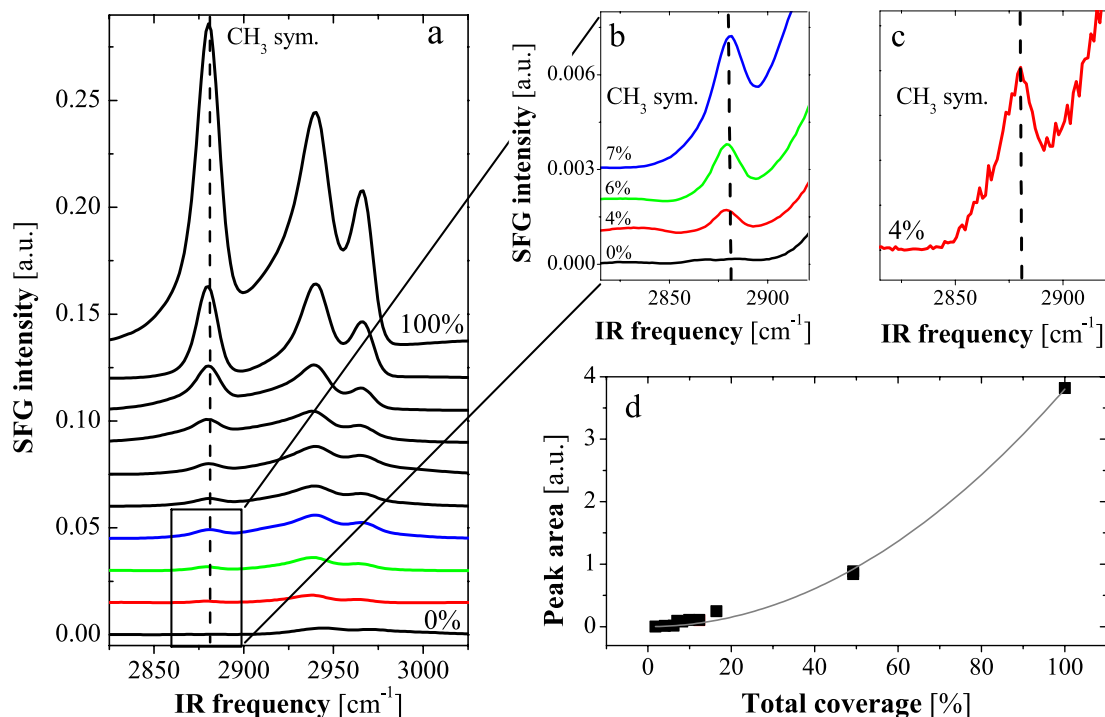


Figure 2.13: Calculation of the lower detection level of the SFG system - (a) Spectra of a fully deuterated SAM (0%, bottom trace), a fully undeuterated SAM (100%, top trace), and mixtures in between (from top: 50%, 16%, 12%, 10%, 8%, 7%, 6% and 4%). All spectra were background subtracted, smoothed with a Savitzky-Golay routine using 15 data points, and plotted as the resonant contributions as described in Sec. 2.3.3. (b) Magnified spectra of the four lowest surface coverages highlighting the decrease in the CH₃ symmetric stretch. (c) Unsmoothed spectrum at 4% surface coverage for SNR determination. (d) Intensity of the symmetric CH₃ vibration as a function of surface coverage with the corresponding quadratic fit. The peak area was quantified using Lorentzian fits of the resonant SFG spectra.

2.3 Sum-frequency generation Spectroscopy (SFG)

hence the sensitivity of the spectrometer. Note that this peak was completely absent in the fully deuterated monolayer but still present in the mixed monolayer with the lowest undeuterated content tested (4% surface coverage, corresponding to 0.19 molecules per nm² assuming 0.21 nm² per alkanethiol molecule[34]) (Fig. 2.13b). The intensity of the SFG signal is given by:

$$I_{SFG} \propto N^2 |\langle \beta \rangle|^2 \quad (2.23)$$

where $\langle \beta \rangle$ is the average molecular hyperpolarizability and N the molecular surface coverage. This quadratic relationship was supported by the experimental data. Ultimately, the lower detection limit of this system was found experimentally to be 4% with an SNR of 100. Theoretically, it should be possible to achieve a signal at 2% coverage with an SNR of 25, or even at 1% coverage with an SNR of 6.25. This detection limit is lower than previously reported values for other homodyne-detected systems (10% coverage) and comparable to heterodyne-detected systems, with lower reported limits of 1% coverage.[31]

2.3.4 Thin-layer analysis (TLA) cell

To study thin films on solid supports in aqueous environments, a cell inspired by the IR spectroscopy cell of Skoda *et al.*[35] was designed. In this arrangement the sample is probed through a thin aqueous layer located between it and an IR-transparent prism (Fig. 2.14). Overall, the TLA cell consists of five parts: (i) a base with (ii) a thermostated reservoir, (iii) a sample support, (iv) an IR-transparent prism, and (v) a vertical threaded rod fixed to a bridge for applying force to the prism.

The temperature of the TLA cell can be controlled by a thermostated bath (Ministat 230cc, Huber). A Delrin[®] base holds an aluminum block which contains a serpentine cooling channel to increase the heat exchange rate. Acetal quick disconnect couplings (PMC series, Colder Products) with water stops allow quick mounting and unmounting without spilling cooling liquid. A kinematic mount attached to the bottom of the cell allows it to be removed and another cell put in its place as described in Sec. 2.3.2.3.

The support shown in Fig. 2.14 is designed for standard Au-coated silicon wafers, however, any kind of flat surfaces can be placed under the prism. This design allows easy exchange between different samples. It also allows the reuse of costly prisms as

2. METHODS

they do not need to be coated. For special sample shapes, the Teflon[®] support under the prism can be removed and replaced by other application-specific sample supports.

A hemicylindrical CaF_2 prism with optically polished curved and basal surfaces (Crystec; 10×20 mm) was chosen for this cell. This shape prevents reflection losses regardless of the angle, as all incoming beams are normal to the surface. Because of the curved surface, the outgoing SFG beam is slightly diverging in the incidence plane. However, the f -number of the SFG beam can be readjusted in the horizontal plane by the telescope in front of the vertical slit of the spectrometer. The focusing on the other axis is not crucial here since the dispersion plane of the grating is horizontal. A Teflon[®] prism adapter was fabricated to apply mechanical force to the top of the prism in order to adjust the thickness of the aqueous layer. This force can be varied by the round nut on top of the cell which drives the threaded rod into the adapter.

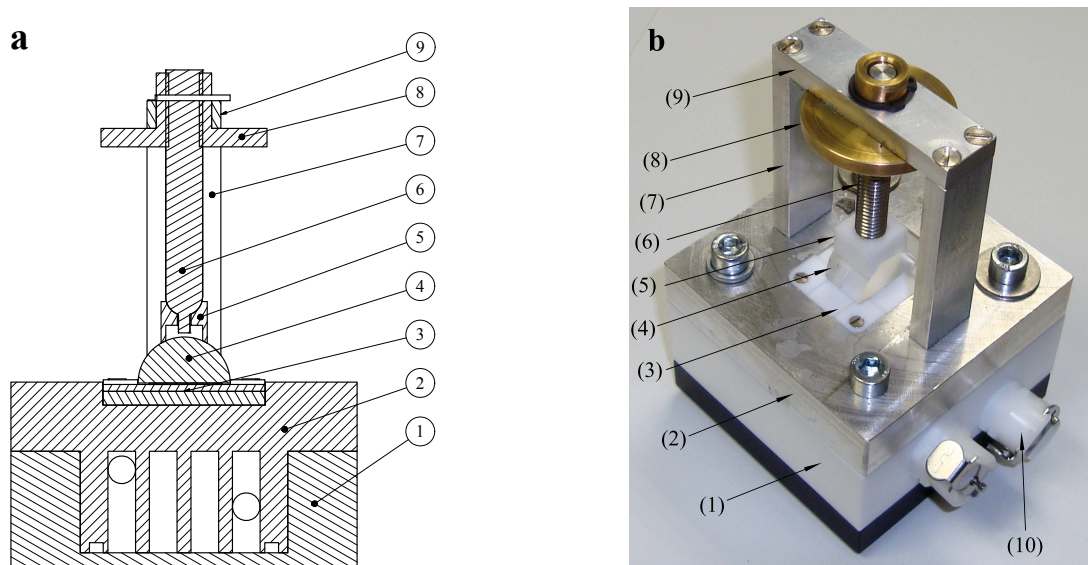


Figure 2.14: Thin layer analysis cell - (a) Cross-sectional view. (b) Photograph. The labels denote: (1) base, (2) thermostated reservoir, (3) sample support, (4) hemicylindrical IR-transparent prism, (5) prism adapter, (6) threaded rod, (7) pillar, (8) round nut, (9) bridge, and (10) quick disconnect couplings.

This cell could also be applied to many other fields of study in surface science including investigation of biomolecules at interfaces such as DNA or peptides.^[18, 36, 37] The TLA cell is now being used by all group members for detecting changes in thin films at solid/liquid interfaces.

2.4 Ellipsometry

Ellipsometry is surface analytical tool, which measures the changes in the polarization state upon reflection from a sample. At optimized conditions both thicknesses and refractive index of thin films can be determined, as long as the sample is able to reflect light. The simplicity of this technique makes it ideal for additional characterization of samples. For a successful ellipsometry experiment a good model describing the samples layer composition must be known. At maximum two arbitrary parameters can be fitted simultaneously with the obtained data.

2.4.1 Theory

Upon reflection from a sample, incident light with a particular polarization state differs in its polarization state afterwards. These changes can be measured and quantified. There are two eigenpolarization states: p-polarization where the electric field of light is oscillating within the plane of incidence and s-polarization where the electric field of the light is oscillating normal to this plane of incidence. The incident and reflected beams can be described by:

$$\vec{E}_{inc} = \begin{pmatrix} |E_P^i| e^{i\delta_P^i} \\ |E_S^i| e^{i\delta_S^i} \end{pmatrix} \quad \vec{E}_{refl} = \begin{pmatrix} |E_P^r| e^{i\delta_P^r} \\ |E_S^r| e^{i\delta_S^r} \end{pmatrix} \quad (2.24)$$

The changes upon reflection are described with the so-called ellipsometric angles, Ψ and Δ :

$$\Delta = (\delta_P^r - \delta_S^r) - (\delta_P^i - \delta_S^i) \quad (2.25)$$

$$\tan \Psi = \frac{|E_P^r|/|E_P^i|}{|E_S^r|/|E_S^i|} \quad (2.26)$$

The reflectivity properties of a sample are given by the corresponding reflectivity coefficients r_p and r_s . These are complex quantities that account for the changes in phase and amplitude of the reflected electric fields with respect to the incident fields as described by:

$$r_p = \frac{|E_P^r|}{|E_P^i|} e^{i(\delta_P^r - \delta_P^i)} \quad r_s = \frac{|E_S^r|}{|E_S^i|} e^{i(\delta_S^r - \delta_S^i)} \quad (2.27)$$

2. METHODS

combined with the equations above, the basic equation of ellipsometry is obtained:

$$\tan \Psi e^{i\Delta} = \frac{r_p}{r_s} \quad (2.28)$$

Eqn. 2.28 relates the ellipsometric angles Ψ and Δ with the reflectivity coefficients for p and s light.

For ultrathin polymeric films with thicknesses in the nm range the changes in reflectivity are very small and therefore Ψ is not changed in a detectable way. In this case the data analysis relies only on Δ and only one parameter of the model can be fitted, usually either the refractive index or the thickness.

2.4.2 Experimental design

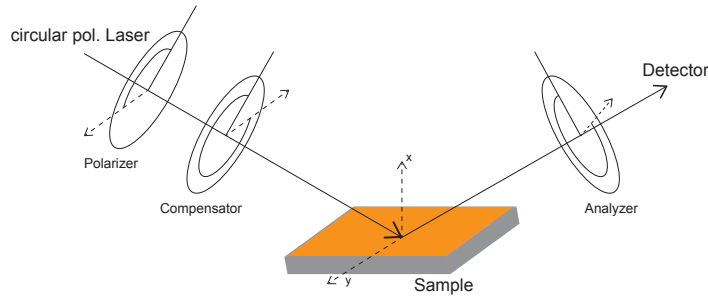


Figure 2.15: Ellipsometer in a PCSA-configuration -

There are many available designs of implementation and an overview is presented by Azzam and Bashara.[38] A common scheme is shown in Fig. 2.15. The main components are a polarizer P which produces linearly polarized light, a compensator C which introduces a defined phase retardation of one field component with respect to the orthogonal field component, the sample S, the analyzer A, and a detector. This setup allows for the determination of the ellipsometric angles with various operation modes. The *Nullellipsometry* mode was applied in this work. The setting of the optical components is chosen such that the light at the detector vanishes. A given elliptical state of polarization of the incident light leads to linearly polarized light after reflection and can be completely extinguished with an analyzer. The following equation relates the reflectivity coefficients r_p and r_s to the settings of the components [39]:

$$\frac{r_p}{r_s} = -\tan A \frac{\tan C + \rho_c \tan(C - P)}{1 - \rho_c \tan C \tan(C - P)} \quad (2.29)$$

for a vanishing intensity $I = 0$ at the detector, using a quarter wave plate as compensator ($\tan C = 0, \delta_C = \pi/2 \Rightarrow \rho_c = -i$), is C fixed at $\pm 45^\circ$. With eqn. 2.29 the ellipsometry equation 2.28 then simplifies to:

$$\begin{aligned} \tan \Psi e^{i\Delta} = \frac{r_p}{r_s} &= \tan A_0 e^{i(2P_0 + \frac{\pi}{2})} & C = -45^\circ \\ \tan \Psi e^{i\Delta} = \frac{r_p}{r_s} &= -\tan A_0 e^{i(-2P_0 + \frac{\pi}{2})} & C = 45^\circ \end{aligned} \quad (2.30)$$

This equation links Ψ and Δ to the null settings of the ellipsometer. For further measurements, the ellipsometer (Multiskop, www.optrel.de, [40]) was used as a Nullellipsometer with an angle of incidence of 70° (Fig. 2.16). A HeNe laser with 633 nm wavelength was used as light source.

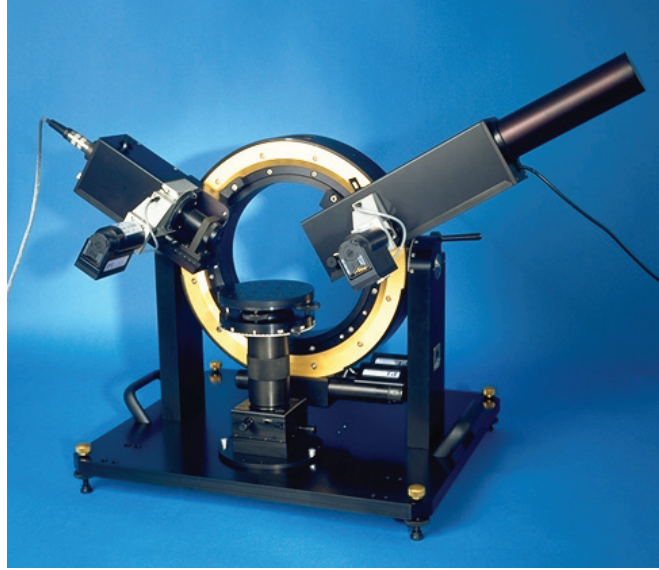


Figure 2.16: Ellipsometer - Optrel Multiskop used for the ellipsometry measurements

In order to measure *in situ*, a special sample cell for aqueous environment from Optrel was used. This cell had a reservoir for ~ 20 ml water and was kept in good thermal contact with a solid steel plate including an inlet and outlet for a circulating bath. The instrumental setup included a tiny temperature sensor on top of the sample in the water away from the beam path. For this purpose a small PT100 wire was used.

2. METHODS

2.5 Contact angle

By measuring the contact angle the surface free energy of a solid and surface tension of the pendant drop or captive bubble can be determined. The change in interfacial tension, $\gamma_{br,liq}$ and $\gamma_{br,air}$, at the polymer-water and polymer-air interface, respectively, is of prime importance for the understanding molecular phase transitions. Using Dupre's definition of the interfacial tension,

$$\gamma_{br,liq} = \gamma_{br} + \gamma_{liq} - \eta \quad (2.31)$$

with γ_{br} and γ_{liq} the surface tensions of the solid polymer and the liquid, respectively, and η the adhesion energy, together with Young's equation,

$$\eta = \gamma_{liq}(1 + \cos \theta) \quad (2.32)$$

the difference between the interfacial tensions of the brush in saturated water vapor and water, $\Delta\gamma_{br}$ is:

$$\Delta\gamma_{br} = \gamma_{br,air} - \gamma_{br,liq} = \gamma_{liq} \cos(\theta) \quad (2.33)$$

Since interfacial tensions are excess free energies per unit area, $\Delta\gamma_{br}$ obey specific thermodynamic rules and its variation follows a Gibbs adsorption equation:[\[41, 42\]](#)

$$d\Delta\gamma_{br} = -\Delta S_{br}dT - \Delta\Gamma_{liq}d\mu_{liq} - \Delta\Gamma_{br}d\mu_{br} \quad (2.34)$$

where ΔS_{br} is the difference of excess surface entropy between the brush/air and brush/liquid interfaces, μ_{br} (and μ_{liq}) are the chemical potentials of the brush and the liquid, respectively, and $\Delta\Gamma_{br}$ (and $\Delta\Gamma_{liq}$) are the differences of excess concentration in monomer segments and in water, respectively, between the brush/air and brush/liquid interfaces. So both the chemical potentials and excess entropy can contribute to a contact angle change.

The contact angle measurements were performed with the captive bubble method, also called inverse contact angle. Normal contact angle measurements with sessile drops have the disadvantage of working in air and also of rapid water evaporation at higher temperatures. In the captive bubble method, however, the samples are in an aqueous environment facing down and an air bubble is generated with an inverse needle and

sticking captively under the surface. An air bubble ~ 2 mm diameter is trapped below the sample (see Fig 2.17a and 2.17b) and the shape of the drop is then fit near the triple line by arcs of a circle with the *DROPimage Standard* software provided with the instrument. Left and right contact angles are averaged to obtain the contact angle.

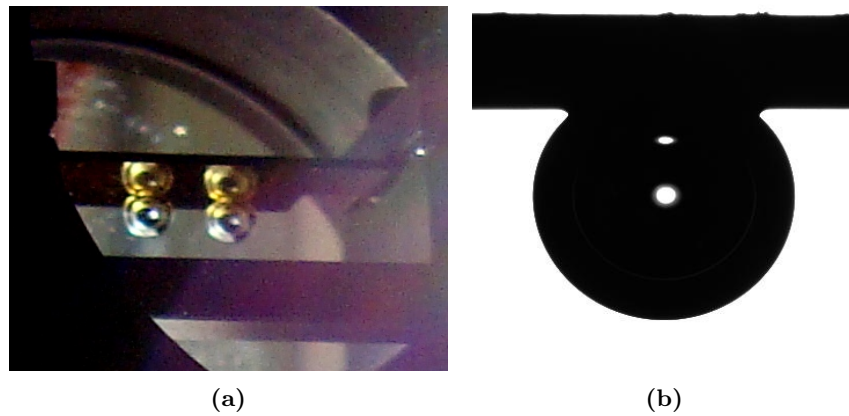


Figure 2.17: Photograph of two 2 mm captive air bubbles under a gold sample (a); typical image acquired from the instrument's camera, for determining the contact angles. (b)

For the captive bubble measurements in this work a Contact Angle Advanced Goniometer from Rame-Hart Instrument Co. (www.ramehart.com, USA) was used. It included a temperature control for the water reservoir.

REFERENCES

References

- [1] B. Kasemo, “Biological surface science,” *Surf. Sci.*, vol. 500, pp. 656–677, 2002. [18](#)
- [2] D. G. Castner and B. D. Ratner, “Biomedical surface science: Foundations to frontiers,” *Surf. Sci.*, vol. 500, pp. 28–60, 2002. [18](#)
- [3] B. Ratner, A. Hoffman, F. Schoen, and J. Lemons, *Biomaterials Science: an Introduction to Materials in Medicine*. Elsevier Science and Technology Books, 1997. [18](#)
- [4] F. M. Geiger, “Second harmonic generation, sum frequency generation, and $\chi^{(3)}$: Dissecting environmental interfaces with a nonlinear optical swiss army knife,” *Annu. Rev. Phys. Chem.*, vol. 60, pp. 61–83, 2009. [18](#)
- [5] Y. R. Shen and V. Ostroverkhov, “Sum-frequency vibrational spectroscopy on water interfaces: Polar orientation of water molecules at interfaces,” *Chem. Rev.*, vol. 106, pp. 1140–1154, 2006. [19](#)
- [6] Z. Chen, Y. R. Shen, and G. A. Somorjai, “Studies of polymer surfaces by sum frequency generation vibrational spectroscopy,” *Annu. Rev. Phys. Chem.*, vol. 53, pp. 437–465, 2002. [19](#)
- [7] S. Roke, “Nonlinear optical spectroscopy of soft matter interfaces,” *ChemPhysChem*, vol. 10, pp. 1380–1388, 2009. [19](#)
- [8] M. B. Raschke and Y. R. Shen, “Nonlinear optical spectroscopy of solid interfaces,” *Curr. Opin. Solid State Mater. Sci.*, vol. 8, pp. 343–352, 2004. [19](#)
- [9] H. C. Allen, N. N. Casillas-Ituarte, M. R. Sierra-Hernandez, X. Chen, and C. Y. Tang, “Shedding light on water structure at air–aqueous interfaces: ions, lipids, and hydration,” *Phys. Chem. Chem. Phys.*, vol. 11, pp. 5538–5549, 2009. [19](#)
- [10] C. S. Tian and Y. R. Shen, “Sum-frequency vibrational spectroscopic studies of water/vapor interfaces,” *Chem. Phys. Lett.*, vol. 470, pp. 1–6, 2009. [19](#)
- [11] S. Gopalakrishnan, D. F. Liu, H. C. Allen, M. Kuo, and M. J. Shultz, “Vibrational spectroscopic studies of aqueous interfaces: Salts, acids, bases, and nanodrops,” *Chem. Rev.*, vol. 106, pp. 1155–1175, 2006. [19](#)
- [12] G. L. Richmond, “Molecular bonding and interactions at aqueous surfaces as probed by vibrational sum frequency spectroscopy,” *Chem. Rev.*, vol. 102, pp. 2693–2724, 2002. [19](#)
- [13] M. A. Leach and G. L. Richmond, “Recent experimental advances in studies of liquid/liquid interfaces,” *Faraday Discuss.*, vol. 129, pp. 1–21, 2005. [19](#)

REFERENCES

- [14] A. J. Hopkins, C. L. McFearin, and G. L. Richmond, "Investigations of the solid-aqueous interface with vibrational sum-frequency spectroscopy," *Curr. Opin. Solid State Mater. Sci.*, vol. 9, pp. 19–27, 2005. [19](#)
- [15] J. Kim, G. Kim, and P. S. Cremer, "Investigations of polyelectrolyte adsorption at the solid/liquid interface by sum frequency spectroscopy: Evidence for long-range macromolecular alignment at highly charged quartz/water interfaces," *J. Am. Chem. Soc.*, vol. 124, no. 29, pp. 8751–8756, 2002. [19](#)
- [16] V. Ostroverkhov, G. A. Waychunas, and Y. R. Shen, "Vibrational spectra of water at water/ α -quartz (0 0 0 1) interface," *Chem. Phys. Lett.*, vol. 386, no. 1-3, pp. 144–148, 2004. [19](#)
- [17] M. A. Even, C. Chen, J. Wang, and Z. Chen, "Chemical structures of liquid poly(ethylene glycol)s with different end groups at buried polymer interfaces," *Macromolecules*, vol. 39, no. 26, pp. 9396–9401, 2006. [19](#)
- [18] O. M. Mermut, D. C. Philips, R. L. York, K. R. McCrea, R. S. Ward, and G. A. Somorjai, "In situ adsorption studies of a 14-amino acid leucine-lysine peptide onto hydrophobic polystyrene and hydrophilic silica surfaces using quartz crystal microbalance, atomic force microscopy, and sum frequency generation spectroscopy," *J. Am. Chem. Soc.*, vol. 128, no. 11, pp. 3598–3607, 2006. [19](#), [40](#)
- [19] P. L. Hayes, E. H. Chen, J. L. Achtyl, and F. M. Geiger, "An optical voltmeter for studying cetyltrimethylammonium interacting with fused silica/aqueous interfaces at high ionic strength," *J. Phys. Chem. A*, vol. 113, no. 16, pp. 4269–4280, 2009. [19](#)
- [20] P. T. Wilson, L. J. Richter, W. E. Wallace, K. A. Briggman, and J. C. Stephenson, "Correlation of molecular orientation with adhesion at polystyrene/solid interfaces," *Chem. Phys. Lett.*, vol. 363, no. 1-2, pp. 161–168, 2002. [19](#)
- [21] R. L. York, Y. Li, G. J. Holinga, and G. A. Somorjai, "Sum frequency generation vibrational spectra: the influence of experimental geometry for an absorptive medium or media," *J. Phys. Chem. A*, vol. 113, no. 12, pp. 2768–2774, 2009. [19](#)
- [22] K. A. Becraft and G. L. Richmond, "In situ vibrational spectroscopic studies of the $\text{CaF}_2/\text{H}_2\text{O}$ interface," *Langmuir*, vol. 17, no. 25, pp. 7721–7724, 2001. [19](#)
- [23] P. L. Hayes, J. N. Malin, C. T. Konek, and F. M. Geiger, "Interaction of nitrate, barium, strontium and cadmium ions with fused quartz/water interfaces studied by second harmonic generation," *J. Phys. Chem. A*, vol. 112, no. 4, pp. 660–668, 2008. [19](#)
- [24] M. J. Stein, T. Weidner, K. McCrea, D. G. Castner, and B. D. Ratner, "Hydration of sulphobetaine and tetra(ethylene glycol)-terminated self-assembled monolayers studied by sum frequency generation spectroscopy," *J. Phys. Chem. B*, vol. 113, no. 33, pp. 11550–11556, 2009. [19](#)

REFERENCES

- [25] N. Nishi, D. Hobara, M. Yamamoto, and T. Kakiuchi, “Total-internal-reflection broad-bandwidth sum frequency generation spectroscopy of hexadecanethiol adsorbed on thin gold film deposited on CaF_2 ,” *Anal. Sci.*, vol. 19, pp. 887–890, 2003. [20](#)
- [26] Y. Nishikawa, T. Nagasawa, and K. Fujiwara, “Silver island films for surface-enhanced infrared absorption spectroscopy: effect of island morphology on the absorption enhancement,” *Vib. Spectrosc.*, vol. 6, pp. 43–53, 1993. [20](#)
- [27] X. Wei, S.-C. Hong, X. Zhuang, T. Goto, and Y. R. Shen, “Nonlinear optical studies of liquid crystal alignment on a rubbed polyvinyl alcohol surface,” *Physical Review E*, vol. 62, pp. 5160–5172, 2000. [23](#)
- [28] F. Vidal and A. Tadjeddine, “Sum-frequency generation spectroscopy of interfaces,” *Rep. Prog. Phys.*, vol. 68, pp. 1095–1127, 2005. [23](#)
- [29] T. Weidner, N. T. Samuela, K. McCrea, L. J. Gamble, R. S. Ward, and D. G. Castner, “Assembly and structure of α -helical peptide films on hydrophobic fluorocarbon surfaces,” *Biointerphases*, vol. 5, pp. 9–16, 2010. [25](#)
- [30] L. J. Richter, T. P. Petralli-Mallow, and J. C. Stephenson, “Vibrationally resolved sum-frequency generation with broad-bandwidth infrared pulses,” *Opt. Lett.*, vol. 23, no. 20, pp. 1594–1596, 1998. [25](#)
- [31] I. V. Stiopkin, H. D. Jayathilake, A. N. Bordenyuk, and A. V. Benderskii, “Heterodyne-detected vibrational sum frequency generation spectroscopy,” *J. Am. Chem. Soc.*, vol. 130, pp. 2271–2275, 2008. [28](#), [39](#)
- [32] C. D. Bain, “Sum-frequency vibrational spectroscopy of the solid/liquid interface,” *J. Chem. Soc. Faraday Trans.*, vol. 91, pp. 1281–1296, 1995. [34](#)
- [33] L. Dreesen, C. Humbert, M. Celebi, J. J. Lemaire, A. A. Mani, P. A. Thiry, and A. Pere-mans, “Influence of the metal electronic properties on the sum-frequency generation spectra of dodecanethiol self-assembled monolayers on $\text{Pt}(111)$, $\text{Ag}(111)$ $\text{Au}(111)$ single crystals,” *Appl. Phys. B*, vol. 74, pp. 621–625, 2002. [34](#)
- [34] R. Maoz, J. Sagiv, D. Degenhardt, H. Möhwald, and P. Quint, “Hydrogen-bonded multilayers of self-assembling silanes: structure elucidation by combined fourier transform infra-red spectroscopy and x-ray scattering techniques,” *Supramol. Sci.*, vol. 2, pp. 9–24, 1995. [39](#)
- [35] M. Skoda, R. Jacobs, S. Zorn, and F. Schreiber, “Optimizing the pmirras signal from a multilayer system and application to self-assembled monolayers in contact with liquids,” *J. Electron Spectrosc. Relat. Phenom.*, vol. 172, pp. 21–26, 2009. [39](#)
- [36] C. Howell, R. Schmidt, V. Kurz, and P. Koelsch, “Sum-frequency-generation spectroscopy of dna films in air and aqueous environments,” *Biointerphases*, vol. 3, no. 3, pp. FC47–FC51, 2008. [40](#)

REFERENCES

- [37] S. R. Walter and F. M. Geiger, “Dna on stage: Showcasing oligonucleotides at surfaces and interfaces with second harmonic and vibrational sum frequency generation,” *J. Phys. Chem. Lett.*, vol. 1, pp. 9–15, 2010. [40](#)
- [38] R. M. Azzam and N. Bashara, *Ellipsometry and Polarized Light*. Amsterdam: North Holland Publication, 1979. [42](#)
- [39] R. C. Jones, “A new calculus for the treatment of optical systems,” *J. Opt. Soc. Am.*, vol. 31, pp. 488–493, 1941. [42](#)
- [40] M. Harke, R. Teppner, O. Schulz, H. Orendi, and H. Motschmann, “Description of a single modular optical setup for ellipsometry, surface plasmons, waveguide modes, and their corresponding imaging techniques including brewster angle microscopy,” *Rev. Sci. Instrum.*, vol. 68, pp. 3130–3135, 1997. [43](#)
- [41] A. M. Jonas, K. Glinel, R. Oren, B. Nysten, and W. T. S. Huck, “Thermo-responsive polymer brushes with tunable collapse temperatures in the physiological range,” *Macromolecules*, vol. 40, pp. 4403–4405, 2007. [44](#)
- [42] J. S. Rowlinson and B. Widom, *Molecular Theory of Capillarity*. Clarendon Press, 1982. [44](#)

REFERENCES

3

Materials and sample preparation

3.1 Gold substrates

The gold substrates were prepared by thermal evaporation of 100 nm gold (99.99% purity) onto polished single-crystalline Si (100) wafers (Silicon Sense) that had been pre-coated with a 5 nm titanium adhesion layer. Such evaporated films are polycrystalline in nature with a predominantly (111) orientation^[2] and a grain size of 20-50 nm as observed by atomic force microscopy and their fabrication is a standard procedure as described in ^[1]. Gold coated Si wafers are standard substrates for thiol- or disulfide-derived SAMs. The substrates were cleaned in warm piranha solution (70% H₂SO₄ / 30% H₂O₂) for 10 minutes and rinsed thoroughly with HPLC-grade water immediately prior to SAM preparation. Immediately prior to further chemistry steps the wafers were cleaned by a UV/ozone cleaner (42-220, Jelight) for 2.5 hrs.

3.2 Alkane thiol

The clean wafers were rinsed and placed in either pure or mixed 3 mM solutions of 1-dodecanethiol (Sigma-Aldrich) and deuterated 1-dodecanethiol (C/D/N Isotopes; 98.9% deuteration) in ethanol and incubated at room temperature for 18 hrs. Samples were then removed from the solutions, rinsed in ethanol, dried under flowing N₂, and immediately measured.

3. MATERIALS AND SAMPLE PREPARATION

3.3 pNIPAM

3.3.1 NBT-pNIPAM

There are several well-established methods of preparing pNIPAM samples. In this work, thin films of pNIPAM attached to solid supports were investigated by methods including atom transfer radical polymerization (ATRP), [3, 4, 5] initiated either by UV light [6] and electron beam radiation. [7] The samples were prepared at the University of Heidelberg as follows.

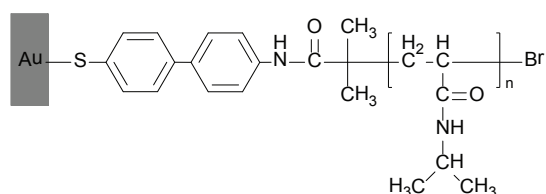


Figure 3.1: - Chemical structure of NBT-pNIPAM

The HPLC-purified chemicals used in this study were purchased from Sigma-Aldrich (Germany) and used as-received. A 4'-nitro-1,1'-biphenyl-4-thiol (NBT)-SAM was used. With an electron beam the NO group was reduced into an amine group, which then becomes the coupling group for surface initiated (SI) polymerization of N-isopropylacrylamide (NIPAM). To initiate the SI-atom transfer radical polymerization (SI-ATRP), a bromoisobutyl-bromid (BIBB) is reacted with the amide group, [7] resulting in a film structure as schematically shown in Fig. 3.1. The grafting density is determined by the surface density of amino group and of initiators after BIBB treatment and is assumed to be approximately 10^{13} - 10^{14} molecules cm^{-2} . [8] The thickness of the films used in this study was determined in the dry state with ellipsometry to be about 10 nm.

3.3.2 Spincoated pNIPAM

The spin-coated samples were coated with pNIPAM purchased from Sigma-Aldrich on the same gold-coated wafers following the cleaning procedure. For the spincoating a mixture of 2g pNIPAM, 6g H_2O and 6g Aceton was dropped on a wafer rotating at 4800 rpm for 20 s. The thickness of the polymer films was measured with ellipsometry to be about 1-2 μm .

3.3.3 ATRP pNIPAM

Another set of pNIPAM films was prepared by the Zauscher group located at the Duke University, Durham, USA, following another protocol.

ATRP initiator deposition: $\text{BrC}(\text{CH}_3)_2\text{COO}(\text{CH}_2)_{11}\text{SH}$ was dissolved in 99% ethanol to a final concentration of 1 mM. Gold chips were immersed in the thiol solution overnight. Then the chips were rinsed with ethanol and water for 1 minute and dried in nitrogen.

Polymerization: 1.5 g (17 mmol) of NIPAAm monomer dissolved in 5 mL of water was filtered into the catalyst-complex solution through a 0.45 mm Millipore Millex filter. The polymerization solution was then transferred into flasks containing the sample substrates with immobilized thiol-ATRP initiator. The flasks were sealed with rubber septa and kept at room temperature under nitrogen, followed by 15 minutes of nitrogen bubbling. The organometallic catalyst was formed in a nitrogen atmosphere by adding CuBr (1.8 mg, 0.013 mmol) and PMDETA (14mL, 0.064 mmol) in a 1:5 molar ratio to 1.0 mL of MeOH as solvent. The mixture was then sonicated for 1-2 min to facilitate the formation of the CuBr/PMDETA complex, followed by nitrogen bubbling. The catalyst solution was then injected into the reaction flask and reacted for 2 hours. After the desired reaction time, substrates were removed from the polymerization solution, exhaustively rinsed with DI water to remove all traces of the polymerization solution, and subsequently dried in a stream of nitrogen.

NIPAAm (99%), Sodium Acrylate(97%), Copper (I) bromide (CuBr, 99.9%), Methanol (MeOH, 99.9%) were obtained from Sigma-Aldrich (Milwaukee, WI). DI (Millipore, Billerica, MA) water and methanol were used as polymerization solvents. N,N,N,N,N-Pentamethyldiethylenetriamine (PMDETA) was used as received from Acros Organics (Hampton, NH). The thiol initiator $\text{BrC}(\text{CH}_3)_2\text{COO}(\text{CH}_2)_{11}\text{SH}$ was synthesized following references:[9, 10].

3.4 Oligo ethylene-glycols

The molecular structure of EG_6OX and EG_yOH is $\text{HS}-(\text{CH}_2)_{11}(\text{OCH}_2\text{CH}_2)_y\text{OX}$ ($\text{X} = \text{H}, \text{CH}_3$; $y=1-5$). The PEG molecules are comprised of $\text{HS}-(\text{CH}_2)_2(\text{OCH}_2\text{CH}_2)_y\text{OX}$ ($\text{X} = \text{H}, \text{CH}_3$; $y\approx 44$) and are a distribution of different chain lengths centred around 44 EG units. EG_6OCH_3 was synthesized in a three-step reaction according to a protocol

3. MATERIALS AND SAMPLE PREPARATION

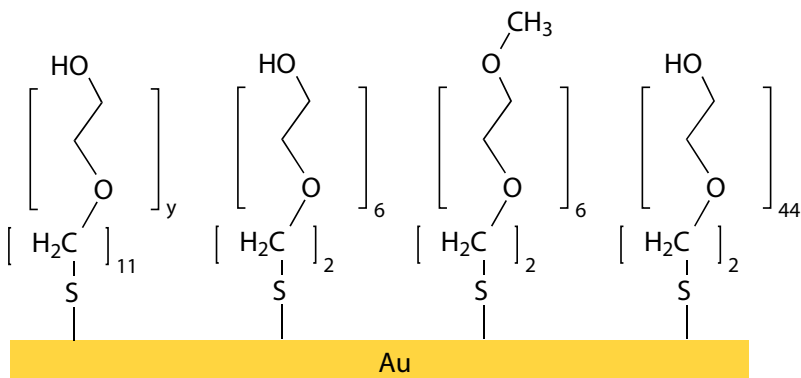


Figure 3.2: Chemical structure of EG_yOX and PEGOX -

described in [11, 12]. EG₆OH was bought from Obiter Research, LLC (Champaign IL). All PEGs were bought from Rapp Polymere GmbH (Tuebingen, Germany), and EG₁₋₅OH was obtained from ProChimia Surfaces Sp. z o.o. (Sopot, Poland). For SAM formation, 1 mM solutions of EG₆OX and EG_yOH in ethanol and 50 μ M solutions of PEG in DMF were prepared. Prior to immersion, the samples were placed in a UV light-emitting photochemical reactor (Southern New England Ultra Violet Company, Branford CT) for 2 h for surface cleaning, then immersed in the thiol solution for 36 h in the dark at room temperature. After removal, the SAMs were first rinsed with the same solvent that was used for the assembly procedure, then with ethanol, dried in a flow of nitrogen, and finally stored under argon.

To verify a successful SAM formation, the samples were analyzed with three different methods: contact angle goniometry, spectral ellipsometry, and X-ray photoelectron spectroscopy (XPS). Sessile drop (Millipore) water contact angles were measured by goniometry under ambient conditions. Droplets were dispensed from a micropipet. The reported values are the average of three measurements taken for different samples with the no contact between the tip and the droplet. Film purity and thickness were analyzed by XPS using a Leybold-Heraeus MAX 200 X-ray photoelectron spectrometer with a magnesium anode as the X-ray source, $K\alpha = 1253.6$ eV. The calculation of the film thickness with XPS was done by quantifying the attenuation of the gold substrate signal due to the adsorption of the SAMs following the description in previous investigations.[13, 14] The resulting spectra are shown in Fig. 3.3 and 3.4. SAM thickness measurements were also performed with a Horiba Jobin Yvon UVISEL spectral

ellipsometer operating in a wavelength range between 250 and 800 nm. The organic film was modeled as a single Cauchy layer at a constant refractive index of 1.5.

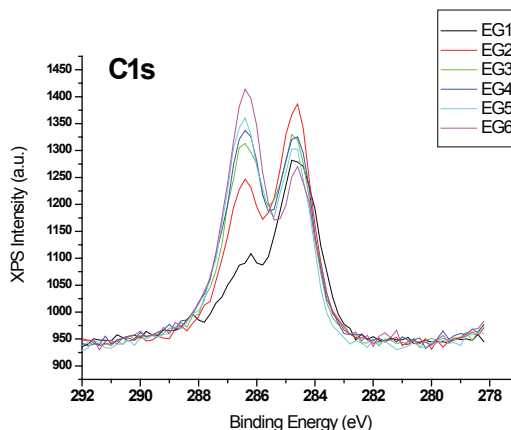


Figure 3.3: detail C1s XPS spectra - ethylene glycols on gold; the C-O peak at 286.5 eV increases with molecular weight and the C-C peak at 284.5 eV is constant, due to the relative long linker. Graphic: Sören Schilp

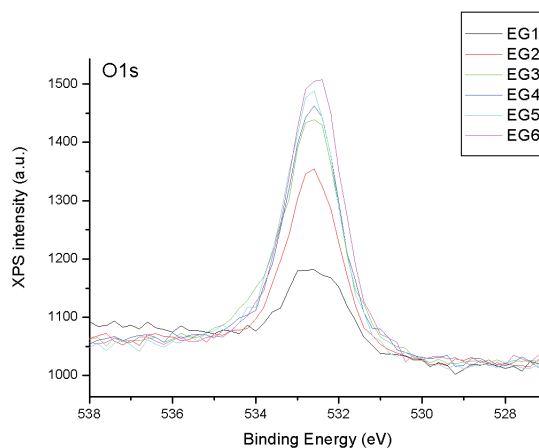


Figure 3.4: detail O1s XPS spectra - ethylene glycols on gold, Graphic: Sören Schilp

3.5 Aqueous environments

For *in situ* SFG measurements, salts used were purchased from Sigma-Aldrich (Munich, Germany). A 0.01 M PBS solution (13 g/kg K_2HPO_4 , 25 g/kg KH_2PO_4), and artificial sea water (ASW) (23.926 g/kg NaCl, 4.008 g/kg Na_2SO_4 , 0.667 g/kg

3. MATERIALS AND SAMPLE PREPARATION

ceKCl, 0.196 g/kg NaHCO_3 , 0.098 g/kg KBr, 0.026 g/kg H_3BO_3 , 0.003 g/kg NaF, 0.05327 g/kg $\text{MgCl}_2 \cdot 6\text{H}_2\text{O}$, 0.01033 g/kg $\text{CaCl}_2 \cdot 2\text{H}_2\text{O}$, 0.00009 g/kg $\text{SrCl}_2 \cdot 6\text{H}_2\text{O}$) were used. The concentrations of 0.1 M CaCl_2 , 0.5 M NaCl were chosen to roughly match the concentration in ASW.

References

- [1] C. Vericat, M. E. Vela, G. A. Benitez, J. A. M. Gago, X. Torrelles, and R. C. Salvarezza, "Surface characterization of sulfur and alkanethiol self-assembled monolayers on au(111)," *J. Phys.-Condens. Mat.*, vol. 18, pp. R867–R900, 2006. [51](#)
- [2] K. Heister, M. Zharnikov, M. Grunze, and L. S. O. Johansson, "Adsorption of alkanethiols and biphenylthiols on au and ag substrates: A high-resolution x-ray photoelectron spectroscopy study," *J. Phys. Chem. B*, vol. 105, pp. 4058–4061, 2001. [51](#)
- [3] M. Kaholek, W. K. Lee, B. LaMattina, K. C. Caster, and S. Zauscher, "Fabrication of stimulus-responsive nanopatterned polymer brushes by scanning-probe lithography," *Nano Lett.*, vol. 4, no. 2, pp. 373–376, 2004. [52](#)
- [4] D. M. Jones, A. A. Brown, and W. T. S. Huck, "Surface-initiated polymerizations in aqueous media: Effect of initiator density," *Langmuir*, vol. 18, no. 4, pp. 1265–1269, 2002. [52](#)
- [5] S. Balamurugan, S. Mendez, S. S. Balamurugan, M. J. O'Brien, and G. P. Lopez, "Thermal response of poly(n-isopropylacrylamide) brushes probed by surface plasmon resonance," *Langmuir*, vol. 19, no. 7, pp. 2545–2549, 2003. [52](#)
- [6] Q. He, A. Kuller, M. Grunze, and J. B. Li, "Fabrication of thermosensitive polymer nanopatterns through chemical lithography and atom transfer radical polymerization," *Langmuir*, vol. 23, no. 7, pp. 3981–3987, 2007. [52](#)
- [7] S. Schilp, N. Ballav, and M. Zharnikov, "Fabrication of a full-coverage polymer nanobrush on an electron- beam-activated template," *Angew. Chem. Int. Ed.*, vol. 47, pp. 6786–6789, 2008. [52](#)
- [8] Q. He, A. Kueller, S. Schilp, F. Leisten, H. A. Kolb, M. Grunze, and J. B. Li, "Fabrication of controlled thermosensitive polymer nanopatterns with one-pot polymerization through chemical lithography," *Small*, vol. 3, no. 11, pp. 1860–1865, 2007. [52](#)
- [9] D. M. Jones, J. R. Smith, W. T. S. Huck, and C. Alexander, "Variable adhesion of micropatterned thermoresponsive polymer brushes: Afm investigations of poly (n-isopropylacrylamide) brushes prepared by surface-initiated polymerizations," *Advanced Materials*, vol. 14, no. 16, pp. 1130–1134, 2002. [53](#)
- [10] M. Kaholek, W. K. Lee, S. J. Ahn, H. W. Ma, K. C. Caster, B. LaMattina, and S. Zauscher, "Stimulus-responsive poly(n-isopropylacrylamide) brushes and nanopatterns prepared by surface-initiated polymerization," *Chem. Mater.*, vol. 16, no. 19, pp. 3688–3696, 2004. [53](#)
- [11] C. Pale-Grosdemange, E. S. Simon, K. L. Prime, and G. M. Whitesides, "Formation of self-assembled monolayers by chemisorption of derivatives of oligo(ethylene glycol) of structure $\text{hs}(\text{ch}_2)_{11}(\text{och}_2\text{ch}_2)_m\text{oh}$ on gold," *J. Am. Chem. Soc.*, vol. 113, pp. 12–20, 1991. [54](#)

REFERENCES

- [12] K. L. Prime and G. M. Whitesides, “Adsorption of proteins onto surfaces containing end-attached oligo(ethylene oxide): A model system using self-assembled monolayers,” *J. Am. Chem. Soc.*, vol. 115, pp. 10714–10721, 1993. [54](#)
- [13] P. Harder, M. Grunze, R. Dahint, G. M. Whitesides, and P. E. Laibinis, “Molecular conformation in oligo(ethylene glycol)-terminated self-assembled monolayers on gold and silver surfaces determines their ability to resist protein adsorption,” *J. Phys. Chem. B*, vol. 102, no. 2, pp. 426–436, 1998. [54](#)
- [14] B. D. Ratner and D. G. Castner, *Surface Analysis - The Principal Techniques*. Chichester, U.K.: Wiley & Sons, 1997. [54](#)

4

Theoretical model and Simulations of SFG spectra

A theoretical procedure for the treatment of the angular dependence of the vibrational sum-frequency generation in multilayered media has been developed. This procedure is based on the transfer matrix method which allows for the study of the influence of beam angles, layer thicknesses, and molecular angles on the detected SF signal emitted from such media. The accuracy of the method has been experimentally verified by comparing simulations with data obtained from sum-frequency-generation on a $\text{CaF}_2/\text{H}_2\text{O}/\text{polymer}/\text{Au}$ layered sample.

4.1 Introduction

In recent years SFG has been applied to the investigation of multiple buried interfaces, including self-assembled monolayers (SAMs) [1] and thin polymer films [2]. Most of these systems can be considered as multilayered since they often involve multiple adsorbate layers supported on a solid substrate (e.g. metal or glass) and in contact with aqueous thin films. Yet the presence of layered media with layers at thicknesses comparable to the wavelengths of the incoming and outgoing light beams creates interference effects that significantly affect the detected SFG signal.

To account for these effects, several models have recently been proposed that specifically include the influence of layer thickness on the SFG signal [3, 4, 5, 6, 7]. Nevertheless, it has been shown for a single interface that other factors can also be of

4. THEORETICAL MODEL AND SIMULATIONS OF SFG SPECTRA

importance when it comes to the enhancement of the SF signal intensity, namely the incident angles of the input beams, the molecular angles of the adsorbates, and the absorption of the intervening media [8, 9]. However, up until now, no model has provided a quantitative analysis of any of these factors comprehensively on the SFG signal in the context of layered media. Although inclusion of these factors into the previous models is technically feasible, the application of algebraic methods such as the Airy method to systems with a large number of layers (e.g. $N \geq 3$) makes any analytical treatment quite cumbersome and impractical for numerical implementation.

In this chapter a theoretical model of the sum-frequency signal generated from a multilayered media is developed. The model makes use of the well-known transfer matrix method which treats the boundary conditions at each interface, and the propagation of light through each homogeneous layer in terms of matrices on the basis of forward- and backward-traveling waves [10, 11]. The matrices relate the field components on both sides of the interface and the layer, respectively, thus reducing the description of the whole layered media to a simple matrix multiplication. Although this approach is completely analogous to simultaneously solving the boundary conditions at all interfaces, it has the distinct advantage of being much more flexible when it comes to solving systems with a large number of layers. This model also provides an extension to previous models in that it facilitates the inclusion of all angular- and layer-dependent factors. Finally, experimental data obtained from a $\text{CaF}_2/\text{H}_2\text{O}/\text{polymer}/\text{Au}$ layered system is presented and compared with simulations.

4.2 Theory

The model presented here considers the propagation (reflection and transmission) of a light beam and a sum-frequency-generation beam in a multilayered medium. Vector fields are specified by boldfaced symbols and matrices by ordinary symbols.

4.2.1 Model description

As a model, let us consider a finite, multilayered medium of total thickness d_{tot} embedded between two semi-infinite media, an ambient medium M_0 , and a substrate medium M_{N+1} (Fig. 4.1). The layered medium consists of N distinct layers M_k ($1 \leq k \leq N$) of thicknesses $d_k \equiv z_k - z_{k-1}$ ($z_0 \equiv 0$) separated by $(k + 1)$ parallel, optically plane

interfaces $I_{(k-1)k}$ and $I_{k(k+1)}$ located at $z = z_{k-1}$ and $z = z_k$, respectively. Each layer has a thickness on the order of the wavelength of the incident beams. Let us assume for simplicity that all media are homogeneous, isotropic, linear and non-magnetic ($\mu = \mu_0$). Moreover, each medium, with the exception of M_0 , is considered as absorbing and characterized by a complex refractive index $\tilde{n}_k = n_{\text{re},k} + in_{\text{im},k}$ ($1 \leq k \leq N + 1$), where $n_{\text{re},k}, n_{\text{im},k}$ are the real and imaginary refractive indices, respectively. The laboratory system is specified by the (x, y, z) axes with the z axis normal to the layers and with the $x-z$ and $x-y$ planes as the incident and interfacial planes, respectively. Let us further assume that incident light beams can be represented as a plane, uniform, monochromatic, and time-harmonic waves with an arbitrary polarization state (elliptical) and an optical angular frequency ω_l ($l = 1, 2, \dots$). These beams are obliquely incident to M_0 on the layered medium at I_{01} under an angle $\theta_{0,l}^+$ relative to the interface normal. The primary incident wave gives rise to both a primary reflected wave back towards M_0 at an angle $\theta_{0,l}^-$ and a primary transmitted wave to M_1 . The latter wave, in turn, becomes a secondary incident wave on I_{12} which again gives rise to both secondary reflected and transmitted waves towards M_1 and M_2 at angles $\theta_{1,2}^-$ and $\theta_{2,3}^+$, respectively. The secondary reflected wave then undergo a series of multiple reflections and transmissions between I_{01} and I_{12} . The whole process repeat itself through the layered medium until the last interface is reached, where there is only a transmitted wave into the substrate.

4.2.2 Transfer matrix method

The problem of finding the relationship between the field amplitudes throughout a multilayered medium is conveniently dealt with by the so-called transfer matrix method.[12, 13, 14] This method takes into account the effect of the interfaces as well as those from the layers on the field amplitudes between successive interfaces. Each side of an interface $I_{(k-1)k}$ is represented by a dynamical matrix D_k , whereas the bulk of the k -th layer is represented by a propagation matrix, P_k . Finally, the field amplitudes in each layer are related by the sequential product of these matrices.

According to Maxwell equations, the \mathbf{E} field of frequency ω at a depth z in the k -th layer ($1 \leq k \leq N$) can be viewed as the superposition of the \mathbf{E} fields associated with partial downward- (+) and upward- (-) propagating waves in the k -th layer and is given by

4. THEORETICAL MODEL AND SIMULATIONS OF SFG SPECTRA

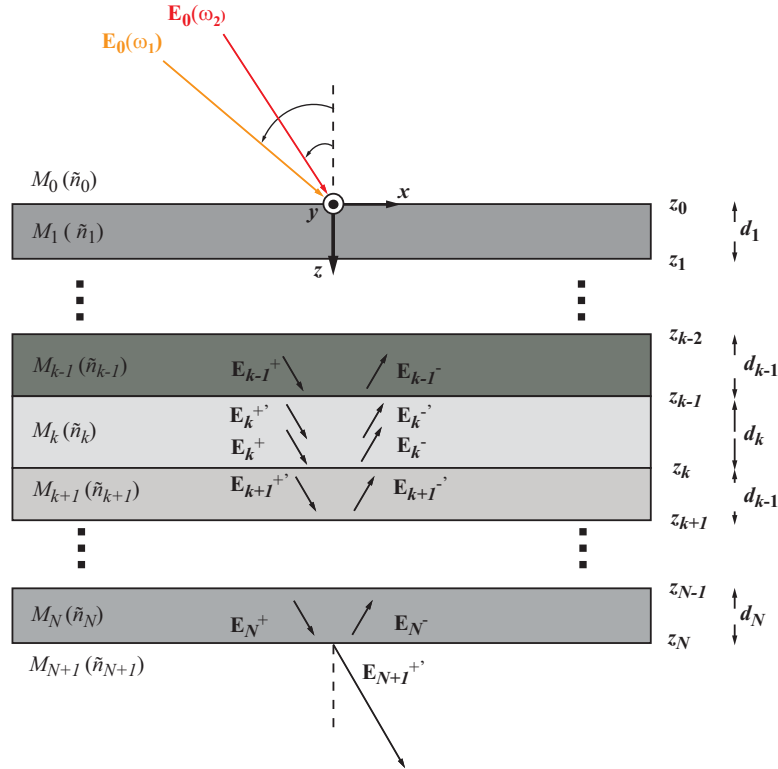


Figure 4.1: Layered medium composed of k layers and $k+1$ interfaces embedded between ambient and substrate media. - The coordinate axes as well as the fields of the forward- and backward-propagating waves above and below the interfaces surrounding the k -th layer are also shown.

$$\mathbf{E}_k(z, t) = \mathbf{E}_k^-(z, t) + \mathbf{E}_k^+(z, t) \quad (4.1)$$

with

$$\mathbf{E}_k^\pm(z, t) \equiv \mathbf{E}_k^\pm(\omega; z, t) = \mathbf{E}_{0k}^\pm \exp[i(\pm \tilde{k}_{kz} z + k_x x) - \omega t], \quad (4.2)$$

where $\tilde{k}_{kz} = \tilde{n}_k(\omega) k_0 \cos \theta_k^+$ denotes the magnitude of the complex wave vector along z in the k -th layer and k_0 the wave vector in vacuum. From Snell's law, the component of the wave vector parallel to the interfaces, k_x , must be the same in every layer ($k_x = k_{kx}$) for any given wavelength. The wave vector for a wave in the k -th layer thus satisfies the relation $k_x^2 + \tilde{k}_{z,k}^2 = \tilde{n}_k^2 k_0^2$.

By using a matrix formulation, one can express the \mathbf{E} field in Eq. (4.1) as a two-component column vector (omitting the time dependence),

$$\mathbf{E}_k^\rho(z) = \begin{bmatrix} E_k^+(z) \\ E_k^-(z) \end{bmatrix}. \quad (4.3)$$

For any given k -th layer, the relationship between the \mathbf{E} and \mathbf{H} field amplitudes adjacent to (i.e. above and below) an arbitrary interface $I_{(k-1)k}$ ($1 \leq k \leq N$) is provided by the continuity of their tangential components at $z = z_{k-1}$ and can be expressed as

$$\begin{aligned} \mathbf{E}_k^\rho(z = z_{k-1}^+) &= \mathbf{T}_{(k-1)k}^\rho \mathbf{E}_k'^\rho(z = z_{k-1}^-) \\ &= (\mathbf{D}_{k-1}^{\rho-1} \mathbf{D}_k^\rho) \mathbf{E}_k'^\rho(z = z_{k-1}^-) \end{aligned} \quad (4.4)$$

with

$$\mathbf{D}_k^\rho = \begin{cases} \begin{bmatrix} \cos \theta_k & \cos \theta_k \\ n_k & n_k \end{bmatrix} & , \rho = p \\ \begin{bmatrix} 1 & 1 \\ n_k \cos \theta_k & -n_k \cos \theta_k \end{bmatrix} & , \rho = s \end{cases} \quad (4.5a)$$

where \mathbf{T}_{ij}^ρ is the so-called transfer matrix. The primes distinguish between fields above and below the interface.

4. THEORETICAL MODEL AND SIMULATIONS OF SFG SPECTRA

The transfer matrix at the interface I_{ij} takes the same form for both polarization type and is given by

$$\mathbf{T}_{ij}^\rho = \frac{1}{t_{ij}^\rho} \begin{bmatrix} 1 & r_{ij}^\rho \\ r_{ij}^\rho & 1 \end{bmatrix} \quad (4.6)$$

with the p - and s -polarized Fresnel reflection and transmission coefficients at interface I_{ij} , r_{ij}^ρ, t_{ij}^ρ , are defined in terms of the electric field amplitudes as:

$$r_{ij}^\rho \equiv \frac{E_{0i}^-}{E_{0i}^+} \bigg|_{E_j' = 0} = \begin{cases} \frac{n_i^2 N_j - n_j^2 N_i}{n_i^2 N_j + n_j^2 N_i}, & \rho = p \\ \frac{N_i - N_j}{N_i + N_j}, & \rho = s \end{cases} \quad (4.7a)$$

$$t_{ij}^\rho \equiv \frac{E_{0j}'}{E_{0i}^+} \bigg|_{E_j' = 0} = \begin{cases} \frac{2N_i}{n_i^2 N_j + n_j^2 N_i}, & \rho = p \\ \frac{2N_i}{N_i + N_j}, & \rho = s \end{cases} \quad (4.7b)$$

where $N = n \cos \theta$. Moreover, the relationship between the two sets of Fresnel coefficients requires that $\mathbf{T}_{ij}^{-1} = \mathbf{T}_{ji}$ and $\mathbf{T}_{ij} \mathbf{T}_{jk} = \mathbf{T}_{ik}$.

For either polarization state, these coefficients satisfy the well-known Stokes relations

$$\begin{aligned} r_{ij}^\rho &= -r_{ji}^\rho, & r_{ik}^\rho &= r_{ij}^\rho + r_{jk}^\rho (1 + r_{ij}^\rho r_{jk}^\rho)^{-1} \\ t_{ij}^\rho t_{ji}^\rho &= 1 - (r_{ij}^\rho)^2, & t_{ij}^\rho t_{jk}^\rho &= t_{ik}^\rho (1 + r_{ij}^\rho r_{jk}^\rho). \end{aligned} \quad (4.8)$$

The amplitude and phase changes of the field amplitudes occurring inside the k -th layer (i.e. between interfaces $I_{(k-1)k}$ and $I_{k(k+1)}$) are related by the propagation matrix \mathbf{P}_k of the layer as:

$$\mathbf{E}_k' (z_k + d_k) = \mathbf{P}_k \mathbf{E}_k^\rho (z_k) \quad (4.9)$$

with

$$\mathbf{P}_k(z) = \begin{bmatrix} \exp(i\delta_k(z)) & 0 \\ 0 & \exp(-i\delta_k(z)) \end{bmatrix} \quad (\mathbf{P}_0 \equiv \mathbf{I}) \quad (4.10)$$

and

$$\delta_k(z) \equiv \begin{cases} 0, & z = z_0 \\ 2\pi k_0 n_k(\omega) z \cos \theta_k, & z > z_0 \end{cases} \quad (4.11)$$

where $\delta_k(z)$ is the phase shift imposed by the propagation of the \mathbf{E} field at a depth z in the k -th layer. The upward propagation of the fields can be easily obtained by getting $P_k(-z) = \bar{P}_k(z) = P_k^{-1}(z)$.

From Eqs. (4.4) and (4.9), the field amplitudes inside the $(k-1)$ -th and k -th layers can be related through

$$\mathbf{E}_{k-1}^\rho = T_{(k-1)k}^\rho P_k \mathbf{E}_k^\rho \quad (4.12)$$

The repeated application of Eq. (4.12) for $(k-1)$ layers and k interfaces yields a relationship between the field amplitudes in the ambient medium and in the k -th layer as:

$$\mathbf{E}_0^\rho = T_{0k}^\rho \mathbf{E}_k^\rho \quad (4.13)$$

with

$$T_{0k}^\rho = \left[\prod_{\kappa=1}^k P_{\kappa-1} T_{(\kappa-1)\kappa}^\rho \right] P_k \quad (1 \leq k \leq N) \quad (4.14)$$

where T_{0k} is the overall transfer matrix from M_0 to M_k . The overall transfer matrix in the opposite direction can be easily obtained by putting $T_{k0} = T_{0k}^{-1}$.

Similarly to Eq. (4.6), T_{0k} can be expressed in terms of the overall complex Fresnel reflection and transmission coefficients as:

$$T_{0k}^\rho = \frac{1}{t_{0k}^\rho} \begin{bmatrix} 1 & -r_{0k}^\rho \\ r_{0k}^\rho & 1 \end{bmatrix} \quad (4.15)$$

with the Fresnel coefficients r_{0k}^ρ and t_{0k}^ρ given in terms of the matrix elements of T_{0k} such as

4. THEORETICAL MODEL AND SIMULATIONS OF SFG SPECTRA

$$r_{0k}^\rho \equiv \frac{E_0^-}{E_0^+} \bigg|_{E_k'^- = 0} = \frac{T_{21}}{T_{11}} \quad (4.16a)$$

$$t_{0k}^\rho \equiv \frac{E_k'^+}{E_0^+} \bigg|_{E_k'^- = 0} = \frac{1}{T_{11}} \quad (4.16b)$$

4.2.3 Fundamental fields in the layered media

The transfer matrix method in Eq. (4.13) can easily be used with multiple beams, as in the case of sum-frequency-generation. Indeed, the fundamental fields $\mathbf{E}_{k,l}^\rho$ of frequencies ω_l ($l = 1, 2$) propagating at a depth z in the k -th layer can be related to the incident fields $\mathbf{E}_{0,l}^\rho$:

$$\mathbf{E}_{k,l}^\rho(z) \equiv \mathbf{E}_k^\rho(\omega_l; z) = \mathbf{T}_{k0,l}^\rho \mathbf{E}_{0,l}^\rho \quad (4.17)$$

with

$$\mathbf{T}_{k0,l}^\rho = \mathbf{P}_{k,l}^{-1} \left[\prod_{\kappa=k}^1 \mathbf{T}_{\kappa(\kappa-1),l}^\rho \mathbf{P}_{\kappa-1,l}^{-1} \right] \quad (1 \leq k \leq N; l = 1, 2) \quad (4.18)$$

where $\mathbf{T}_{k0,l}$ is the overall transfer matrix of the fundamental fields in the layered medium, from M_k to M_0 .

Similarly, Eq. (4.18) can be expressed in terms of the overall complex Fresnel reflection and transmission coefficients:

$$\mathbf{T}_{k0,l}^\rho = \frac{1}{t_{k0,l}^\rho} \begin{bmatrix} 1 & r_{k0,l}^\rho \\ r_{k0,l}^\rho & 1 \end{bmatrix} \quad (4.19)$$

where the Fresnel reflection and transmission coefficients $r_{k0,l}^\rho, t_{k0,l}^\rho$ can be expressed as

$$r_{k0,l}^\rho \equiv \frac{E_{k,l}^-}{E_{k,l}^+} \bigg|_{E_{0,l}^+ = 0} = -\frac{T_{12}}{T_{11}}, \quad (4.20a)$$

$$t_{k0,l}^\rho \equiv \frac{E_{0,l}^-}{E_{k,l}^+} \bigg|_{E_{0,l}^+ = 0} = \frac{\det(\mathbf{T}_{k0,l})}{T_{11}} \quad (\det(\mathbf{T}_{k0,l}) = T_{11}T_{22} - T_{12}T_{21}). \quad (4.20b)$$

Finally, the amplitudes of the fundamental fields reflected and transmitted to the k -th layer are given by

$$E_{k,l} = T_{k0,l} \begin{bmatrix} 1 \\ r_{k0,l}^\rho \end{bmatrix} \quad (4.21a)$$

$$E_{k+1,l} = T_{k0,l}^\rho \begin{bmatrix} 1 \\ t_{k0,l}^\rho \end{bmatrix} \quad (4.21b)$$

As an example, let us consider a two layers ($N = 2$) system. Then, from Eq. (4.18), the overall transfer matrices from M_1 , M_2 and M_3 to M_0 are given, respectively, by

$$T_{10,l} = \frac{1}{t_{10,l}} \begin{bmatrix} 1 & r_{10,l} \\ r_{10,l} & 1 \end{bmatrix}, \quad (4.22a)$$

$$\begin{aligned} T_{20,l} &= T_{21,l} P_{1,l}^{-1} T_{10,l} \\ &= \frac{1}{t_{21,l} t_{10,l}} \begin{bmatrix} \exp(-i\delta_{1,l}) + r_{10,l} r_{21,l} \exp(i\delta_{1,l}) & r_{10,l} \exp(-i\delta_{1,l}) + r_{21,l} \exp(i\delta_{1,l}) \\ r_{21,l} \exp(-i\delta_{1,l}) + r_{10,l} \exp(i\delta_{1,l}) & r_{10,l} r_{21,l} \exp(-i\delta_{1,l}) + \exp(i\delta_{1,l}) \end{bmatrix}, \end{aligned} \quad (4.22b)$$

$$\begin{aligned} T_{30,l} &= T_{32,l} P_{2,l}^{-1} T_{21,l} P_{1,l}^{-1} T_{10,l} \\ &= \frac{1}{t_{32,l} t_{21,l} t_{10,l}} \begin{bmatrix} T_{11} & T_{12} \\ T_{21} & T_{22} \end{bmatrix} \end{aligned} \quad (4.22c)$$

with

$$T_{11} = (\exp(-i\delta_{1,l}) + r_{10,l} r_{21,l} \exp(i\delta_{1,l})) + r_{32,l} (r_{21,l} \exp(-i\delta_{1,l}) + r_{10,l} \exp(i\delta_{1,l})) \quad (4.23a)$$

$$T_{12} = (r_{10,l} \exp(-i\delta_{1,l}) + r_{21,l} \exp(i\delta_{1,l})) + r_{32,l} (r_{10,l} r_{21,l} \exp(-i\delta_{1,l}) + \exp(i\delta_{1,l})) \quad (4.23b)$$

$$T_{21} = r_{32,l} (\exp(-i\delta_{1,l}) + r_{10,l} r_{21,l} \exp(i\delta_{1,l})) + (r_{21,l} \exp(-i\delta_{1,l}) + r_{10,l} \exp(i\delta_{1,l})) \quad (4.23c)$$

$$T_{22} = r_{32,l} (r_{10,l} \exp(-i\delta_{1,l}) + r_{21,l} \exp(i\delta_{1,l})) + (r_{10,l} r_{21,l} \exp(-i\delta_{1,l}) + \exp(i\delta_{1,l})). \quad (4.23d)$$

By using the Stokes relations, one obtains the overall reflection coefficient for one, two and three layers in the form

$$R_{10,l} = r_{01,l} \quad (4.24a)$$

$$R_{20,l} = \frac{r_{01,l} + r_{12,l} \exp(2i\delta_{1,l})}{1 + r_{01,l} r_{12,l} \exp(2i\delta_{1,l})} \quad (4.24b)$$

$$R_{30,l} = \frac{r_{01,l} + r_{12,l} \exp(2i\delta_{1,l}) + r_{23,l} \exp(2i(\delta_{1,l} + \delta_{2,l})) + r_{01,l} r_{12,l} r_{23,l} \exp(2i\delta_2)}{1 + r_{01,l} r_{12,l} \exp(2i\delta_{1,l}) + r_{12,l} r_{23,l} \exp(2i\delta_{2,l}) + r_{01,l} r_{23,l} \exp(2i(\delta_{1,l} + \delta_{2,l}))} \quad (4.24c)$$

The fundamental fields amplitudes at a depth z inside M_1 and M_2 are then deduced from Eq. (4.17):

4. THEORETICAL MODEL AND SIMULATIONS OF SFG SPECTRA

$$\mathbf{E}_{1,l}(z) = \begin{bmatrix} E_{1,l}^+(z) \\ E_{1,l}^-(z) \end{bmatrix} = \mathbf{P}_{1,l}^{-1}(z) \mathbf{T}_{10,l} \begin{bmatrix} 1 \\ R_{20,l} \end{bmatrix} E_{0,l}^+ = \begin{bmatrix} t_{01,l}^\rho e^{i\delta(z)} (1 + r_{01,l} r_{12,l} e^{2i\delta_{1,l}})^{-1} \\ t_{01,l}^\rho r_{12,l} e^{i(2\delta_1 - \delta(z))} (1 + r_{01,l} r_{12,l} e^{2i\delta_{1,l}})^{-1} \end{bmatrix} E_{0,l}^+, \quad (4.25a)$$

$$\begin{aligned} \mathbf{E}_{2,l}(z) &= \begin{bmatrix} E_{2,l}^+(z) \\ E_{2,l}^-(z) \end{bmatrix} = \mathbf{P}_{2,l}^{-1}(z) \mathbf{T}_{20,l} \begin{bmatrix} 1 \\ R_{30,l} \end{bmatrix} E_{0,l}^+ \\ &= \begin{bmatrix} t_{01,l}^\rho e^{i\delta_{2,l}(z)} (1 + r_{01,l} r_{12,l} e^{2i\delta_{1,l}} + r_{12,l} r_{23,l} e^{2i\delta_{2,l}} + r_{01,l} r_{23,l} e^{2i(\delta_{1,l} + \delta_{2,l})})^{-1} \\ t_{01,l}^\rho r_{12,l} e^{i(2\delta_{1,l} - \delta_{2,l}(z))} (1 + r_{01,l} r_{12,l} e^{2i\delta_{1,l}} + r_{12,l} r_{23,l} e^{2i\delta_{2,l}} + r_{01,l} r_{23,l} e^{2i(\delta_{1,l} + \delta_{2,l})})^{-1} \end{bmatrix} E_{0,l}^+ \end{aligned} \quad (4.25b)$$

4.2.4 Sum-frequency fields

In this section a theoretical approach developed for the treatment of SFG signal at a single interface and outlined previously by Sipe [15] is extended in a straightforward manner to any given interface within a layered medium. Without loss of generality, let's assume two coplanar, non-collinear, co-propagating waves with frequency ω_l ($l = 1, 2$) incident on the interface $I_{(k-1)k}$ between two centrosymmetric layers, M_{k-1} and M_k , with refractive indices \tilde{n}_{k-1} and \tilde{n}_k , respectively. The region that contributes to the generated nonlinear signal is assumed to be a field-induced polarization sheet located close to the interface $I_{(k-1)k}$ at position $z = z_{k-1}^+$ within M_k . The thickness δz of the polarization sheet is assumed to be much smaller than any wavelength.

Following Eq. (4.17), the \mathbf{E} -fields of frequency ω_l found at the polarization sheet in M_{k+1} can be written such as

$$\mathbf{E}_{k,l}^\rho(z = z_{k-1}^+) = \mathbf{T}_{k0,l}^\rho \mathbf{E}_{0,l}^\rho \quad (4.26)$$

Within the electric dipole approximation the surface fields $\mathbf{E}_{k,l}^\rho(z = z_{k-1}^+)$ at the polarization sheet are coupled by the second-order nonlinear susceptibility $\chi_k^{(2)}$ which vanishes only in centrosymmetric media, not at the interface where the symmetry is broken. Compared with section 2.3.1, the induced polarization field at the sum-frequency (SF), $\omega_3 = \omega_1 + \omega_2$, in the k -th layer is given by

$$\mathbf{P}_{k,3}^{(2)}(z = z_{k-1}^+) = \varepsilon_0 \chi_{k,3}^{(2)} : \mathbf{E}_{k,1}(z = z_{k-1}^+) \mathbf{E}_{k,2}(z = z_{k-1}^+) \quad (4.27)$$

where ε_0 is the permittivity of vacuum.

The SF fields generated by the induced polarization field are emitted upward and downward, towards M_{k-1} and M_k , respectively, and are written as:

$$\mathbf{E}_3^I = T_{0k,l}^\rho \mathbf{P}_{k,3}^{(2)}(z = z_{k-1}^+) \quad (4.28a)$$

$$\mathbf{E}_3^{II} = T_{0N,l}^\rho r_{34,l}^\rho T_{N(k-1),l}^\rho \mathbf{P}_{k,3}^{(2)}(z = z_{k-1}^+) \quad (4.28b)$$

where \mathbf{E}_3^I is the SF-field "reflected" from the nonlinear polarization sheet and \mathbf{E}_3^{II} is the SF-field transmitted until the substrate, reflected, and then emitted through the entire layer stack towards M_0 . Usually, the \mathbf{E}_3^{II} is much stronger and is therefore used in most simulations.

Due to **k**-matching condition, the SF wave is emitted in both reflection and transmission directions from the polarization sheet at a specific angle is given by

$$\sin \theta_{k,3} = \frac{1}{n_{k,3}\omega_3} (n_{k,1}\omega_1 \sin \theta_{k,1} + n_{k,2}\omega_2 \sin \theta_{k,2}). \quad (4.29)$$

Finally, the overall SF field generated from the layered medium is the sum of the SF fields generated at the $(k+1)$ interfaces and can be written as

$$\mathbf{E}_3 = \sum_{i=1}^{N+1} \mathbf{E}_3^{\{i\}}. \quad (4.30)$$

The overall intensity of the SF signal generated from the layered medium is proportional to the square of the absolute value of the SF field such that

$$I_3 \propto |\mathbf{E}_3|^2 \quad (4.31)$$

4.2.5 Molecular second order nonlinear susceptibility

The $\chi^{(2)}$ for the second order nonlinear polarization sheet in Eq. 4.27 had yet to be determined. In this section the value for the resonant contributions will be derived. This tensor relates the linear polarization of the sample to the second order nonlinear polarization, giving rise to the SF signal. The macroscopic second-order susceptibility tensors $\chi_{ijk}^{(2)}$ are related to the microscopic hyperpolarizability tensor elements β_{ijk} in the molecular coordinates system $S(a, b, c)$ through the ensemble average, denoted by $\langle \rangle$, over all possible molecular orientations. [16]

$$\chi_{ijk}^{(2)}(\Omega) = \varepsilon_0 N_s \sum_{\alpha, \beta, \gamma} \langle R_{ijk}^{\alpha\beta\gamma}(\Omega) \rangle \beta_{\alpha\beta\gamma}^{((2)} \quad (4.32)$$

4. THEORETICAL MODEL AND SIMULATIONS OF SFG SPECTRA

where $R_{ijk}^{\alpha\beta\gamma}(\Omega) = R_{i\alpha}(\psi)R_{j\beta}R_{k\gamma}$ is the 27×27 Euler transformation matrix between the molecular-fixed coordinate system $S(a, b, c)$ and the laboratory-fixed coordinate system $S(x, y, z)$ through a set of Euler angles ($\Omega = \phi, \theta, \psi$). The 729 elements composing this matrix have been tabulated by Hirose et al.[17]

N_s is the molecular surface density. The orientation of the different chemical groups (CH_2 , CH_3 , etc.) can be described by three Euler angles, a tilt angle θ relative to the Z -axis, a twist angle ψ around the molecular z -axis, and an azimuthal angle ϕ around the Z axis. The possible need for local field corrections due to induced dipoles is neglected, since the polarizability of the polymer or even the substrate is small.[18]

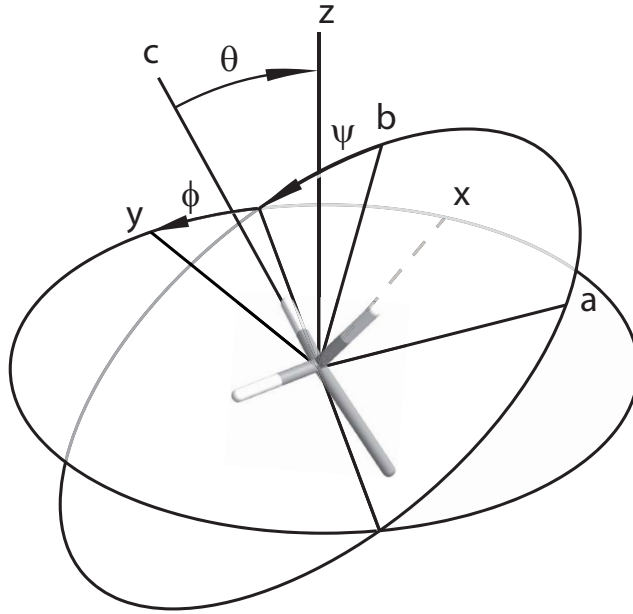


Figure 4.2: Orientational angles relating the molecular-fixed and surface-fixed coordinate systems - The (a,b,c) and (x,y,z) axis systems corresponds to the CH_3 group and to the polymer molecular, respectively. The symbols ϕ, θ, ψ represent the azimuthal about the z -axis, the tilt angle relative to the z -axis, and the twist angle.

For the actual transformation of the microscopic $\beta_{\alpha\beta\gamma}$ to β_{ijk} :

$$\beta_{ijk} = \sum_{\alpha\beta\gamma} R(\Omega)_{ijk,\alpha\beta\gamma} \beta_{\alpha\beta\gamma} \quad (4.33)$$

with $(i, j, k = x, y, z; \alpha, \beta, \gamma = a, b, c)$

The SFG spectra can have, in principle, contributions from all the 27 different elements of the macroscopic susceptibility tensor:

$$\chi_{\text{eff}}^{(2)} = \sum_{i,j,k} \chi_{\text{eff},ijk}^{(2)} \quad (i, j, k = x, y, z) \quad (4.34)$$

However in the SFG literature only three independent experimental polarization combinations are commonly used, namely, *ssp*, *sps*, and *ppp*. This fact reduces the amount of necessary elements of $\chi^{(2)}$ to the following in the laboratory coordinate system:[17]

$$\chi_{\text{eff},ssp}^{(2)} = \chi_{yyx}^{(2)} + \chi_{yyz}^{(2)} \quad (4.35a)$$

$$\chi_{\text{eff},sps}^{(2)} = \chi_{xyy}^{(2)} + \chi_{yzy}^{(2)} \quad (4.35b)$$

$$\chi_{\text{eff},ppp}^{(2)} = \chi_{xxx}^{(2)} + \chi_{xxz}^{(2)} + \chi_{xzx}^{(2)} + \chi_{zxx}^{(2)} + \chi_{zzx}^{(2)} + \chi_{zxx}^{(2)} + \chi_{zzz}^{(2)} \quad (4.35c)$$

Symmetry considerations for the molecular layer simplify the molecular β significantly. Since it is mostly the symmetric and asymmetric stretching vibrations of CH_3 which are analyzed and used as the basis of interpretations in this work, the focus will be on their symmetry. For this molecular group the hyperpolarizability elements $\beta_{i,j,k}$ which are not vanishing in the corresponding C_{3v} symmetry group are shown in Table. 4.1 (see [17])

non vanishing β elements	vibrational mode
$aaa = -bba = -abb = -bab$	asymmetric
$aac = bbc$	symmetric
$caa = cbb$	asymmetric
$aca = bcb$	asymmetric
ccc	symmetric

Table 4.1: non vanishing β elements assuming a C_{3v} symmetry

Next, we transform the non-zero elements of β into the laboratory coordinate system by using equation(4.33). The corresponding parts of the laboratory $\chi^{(2)}$ are shown in Table. 4.2 and 4.3. Since the terms for each element would be too lengthy, an isotropic twist angle ψ was assumed, and an ensemble average of this angle $\langle\psi\rangle$ is included in the tabulated calculation results. The consequence of the the isotropic twist angle is a free rotation of a methyl group around the molecular axis. This ensemble average of all the trigonometric functions $f_{\text{trig}}(\psi)$ appearing after the transformation is calculated as

4. THEORETICAL MODEL AND SIMULATIONS OF SFG SPECTRA

$$\langle f_{trig}(\psi) \rangle = \frac{1}{8\pi^2} \int_0^{2\pi} \int_0^{2\pi} \int_0^\pi f_{trig}(\psi) \sin \theta d\theta d\omega d\psi = 0 \quad (4.36)$$

with $f_{trig}(\psi) = \sin \psi, \sin 2\psi, \sin 3\psi, \cos \psi, \cos 2\psi, \cos 3\psi$

Table 4.2: Nonlinear susceptibility elements of the symmetric stretching modes for molecular groups with C_{3v} symmetry under different polarization configurations. An isotropic twist angle ψ was assumed.

Element	Symmetric stretching (<i>ss</i>)
<i>ppp</i>	
$\chi_{xxx}^{(2)}$	$-\langle S_\theta \rangle \langle C_\phi \rangle \beta_{aac} + \langle S_\theta^3 \rangle \langle C_\phi^3 \rangle (\beta_{aac} - \beta_{ccc})$
$\chi_{xxz}^{(2)}$	$\langle C_\theta \rangle \beta_{aac} - (\langle C_\theta \rangle - \langle C_\theta^3 \rangle) \langle C_\phi^2 \rangle (\beta_{aac} - \beta_{ccc})$
$\chi_{xzx}^{(2)}$	$-(\langle C_\theta \rangle - \langle C_\theta^3 \rangle) \langle C_\phi^2 \rangle (\beta_{aac} - \beta_{ccc})$
$\chi_{xzz}^{(2)}$	$(\langle S_\theta \rangle - \langle S_\theta^3 \rangle) \langle C_\phi \rangle (\beta_{aac} - \beta_{ccc})$
$\chi_{zxx}^{(2)}$	$-(\langle C_\theta \rangle - \langle C_\theta^3 \rangle) \langle C_\phi^2 \rangle (\beta_{aac} - \beta_{ccc})$
$\chi_{zxz}^{(2)}$	$(\langle S_\theta \rangle - \langle S_\theta^3 \rangle) \langle C_\phi \rangle (\beta_{aac} - \beta_{ccc})$
$\chi_{zzx}^{(2)}$	$-(\langle S_\theta^2 \rangle \beta_{aac} + \langle C_\theta^2 \rangle \beta_{ccc}) \langle S_\theta \rangle \langle C_\phi \rangle$
$\chi_{zzz}^{(2)}$	$\frac{3}{4} (\langle C_\theta \rangle - \langle C_\theta^3 \rangle) \beta_{aac} + \langle C_\theta^3 \rangle \beta_{ccc}$
<i>spp</i>	
$\chi_{yyx}^{(2)}$	$-(\langle S_\theta \rangle \langle C_\phi^3 \rangle + \langle S_\theta \rangle (\langle C_\phi \rangle - \langle C_\phi^3 \rangle)) \beta_{aac} + \langle S_\theta^3 \rangle (\langle C_\phi \rangle - \langle C_\phi^3 \rangle) (\beta_{aac} - \beta_{ccc})$
$\chi_{yyz}^{(2)}$	$\langle C_\theta \rangle \beta_{aac} - (\langle C_\theta \rangle - \langle C_\theta^3 \rangle) \langle S_\phi^2 \rangle (\beta_{aac} - \beta_{ccc})$
<i>sps</i>	
$\chi_{yyy}^{(2)}$	$\langle S_\theta^3 \rangle (\langle C_\phi \rangle - \langle C_\phi^3 \rangle) (\beta_{aac} - \beta_{ccc})$
$\chi_{yyz}^{(2)}$	$-(\langle C_\theta \rangle - \langle C_\theta^3 \rangle) \langle S_\phi^2 \rangle (\beta_{aac} - \beta_{ccc})$

4.2.6 Non-resonant $\chi^{(2)}$

SF signal originating not from the interfacial molecular layer rather than from the substrate will be described here. Since the samples were prepared on gold substrates, the non-resonant signal from gold will be discussed. Following [19] for $\chi^{(2)}$ in laboratory

Table 4.3: Nonlinear susceptibility elements of the asymmetric stretching modes for molecular groups with C_{3v} symmetry under different polarization configurations. An isotropic twist angle ψ was assumed.

Element	Asymmetric stretching (<i>as</i>)
<i>ppp</i>	
$\chi_{xxx}^{(2)}$	$-[(S_\theta)(\langle C_\phi \rangle - \langle C_\phi^3 \rangle) - (\langle S_\theta \rangle - \langle S_\theta^3 \rangle)\langle C_\phi^3 \rangle](\beta_{aca} + \beta_{caa})$
$\chi_{xxz}^{(2)}$	$-(\langle C_\theta \rangle - \langle C_\theta^3 \rangle)\langle C_\phi^2 \rangle(\beta_{aca} + \beta_{caa})$
$\chi_{xzx}^{(2)}$	$-(\langle C_\theta \rangle - \langle C_\theta^3 \rangle)\langle C_\phi^2 \rangle\beta_{caa} + [\langle C_\theta \rangle - (\langle C_\theta \rangle - \langle C_\theta^3 \rangle)\langle C_\phi^2 \rangle]\beta_{aca}$
$\chi_{xzz}^{(2)}$	$\langle S_\theta \rangle(\langle C_\theta^2 \rangle\beta_{aca} - \langle S_\theta^2 \rangle\beta_{caa})\langle C_\phi \rangle$
$\chi_{zxx}^{(2)}$	$-(\langle C_\theta \rangle - \langle C_\theta^3 \rangle)\langle C_\phi^2 \rangle\beta_{aca} + [\langle C_\theta \rangle - (\langle C_\theta \rangle - \langle C_\theta^3 \rangle)\langle C_\phi^2 \rangle]\beta_{caa}$
$\chi_{zzx}^{(2)}$	$-\langle S_\theta \rangle(\langle S_\theta^2 \rangle\beta_{aca} - \langle C_\theta^2 \rangle\beta_{caa})\langle C_\phi \rangle$
$\chi_{zzx}^{(2)}$	$(\langle S_\theta \rangle - \langle S_\theta^3 \rangle)\langle C_\phi \rangle(\beta_{aca} + \beta_{caa})$
$\chi_{zzz}^{(2)}$	$(\langle C_\theta \rangle - \langle C_\theta^3 \rangle)(\beta_{aca} + \beta_{caa})$
<i>spp</i>	
$\chi_{yyx}^{(2)}$	$\langle S_\theta^3 \rangle(\langle C_\phi \rangle - \langle C_\phi^3 \rangle)(\beta_{aca} + \beta_{caa})$
$\chi_{yyz}^{(2)}$	$-(\langle C_\theta \rangle - \langle C_\theta^3 \rangle)\langle S_\phi^2 \rangle(\beta_{aca} + \beta_{caa})$
<i>sps</i>	
$\chi_{yxy}^{(2)}$	$[(S_\theta)(\langle C_\phi \rangle - \langle C_\phi^3 \rangle) - (\langle S_\theta \rangle - \langle S_\theta^3 \rangle)(\langle C_\phi \rangle - \langle C_\phi^3 \rangle)]\beta_{caa} - [\langle S_\theta \rangle\langle C_\phi^3 \rangle + (\langle S_\theta \rangle - \langle S_\theta^3 \rangle)(\langle C_\phi \rangle - \langle C_\phi^3 \rangle)]\beta_{aca}$
$\chi_{yzy}^{(2)}$	$[\langle C_\theta \rangle - (\langle C_\theta \rangle - \langle C_\theta^3 \rangle)\langle S_\phi^2 \rangle]\beta_{aca} - (\langle C_\theta \rangle - \langle C_\theta^3 \rangle)\langle S_\phi^2 \rangle\beta_{caa}$

coordinates will apply:

$$\chi_{xxx}^{(2)} = \chi_{xxz}^{(2)} = \chi_{zzx}^{(2)} = \chi_{yyx}^{(2)} = \chi_{yxy}^{(2)} = \chi_{zxx}^{(2)} = \chi_{zyy}^{(2)} = 0 \quad (4.37a)$$

$$\chi_{xxz}^{(2)} = -\frac{\epsilon_0 \omega_p^4}{64\pi^2 n_e e \omega_1 \omega_2 (\omega_1 + \frac{i}{\tau})(\omega_2 + \frac{i}{\tau})} \frac{2\omega_1}{\epsilon_2 \omega_3} \quad (4.37b)$$

$$\chi_{yyz}^{(2)} = \chi_{xxz}^{(2)} \quad (4.37c)$$

$$\chi_{xzx}^{(2)} = -\frac{\epsilon_0 \omega_p^4}{64\pi^2 n_e e \omega_1 \omega_2 (\omega_1 + \frac{i}{\tau})(\omega_2 + \frac{i}{\tau})} \frac{2\omega_1}{\epsilon_1 \omega_3} \quad (4.37d)$$

$$\chi_{yzy}^{(2)} = \chi_{xzx}^{(2)} \quad (4.37e)$$

$$\chi_{zzz}^{(2)} = -\frac{\epsilon_0 \omega_p^4}{64\pi^2 n_e e \omega_1 \omega_2 (\omega_1 + \frac{i}{\tau})(\omega_2 + \frac{i}{\tau})} \frac{1}{\epsilon_1 \epsilon_2} a \quad (4.37f)$$

with the electron charge e , the plasma frequency $\omega_p = 1.37031 \cdot 10^{16} \text{ s}^{-1}$ of gold, the electron density $n_e = 5.90 \cdot 10^{28} \text{ m}^{-3}$, the electron lifetime $\tau = 6.095 \cdot 10^{-15} \text{ s}^{-1}$ and $\epsilon_i = 1 - \frac{\omega_p^2}{\omega_i(\omega_i + \frac{i}{\tau})}$. [20] Furthermore, for a :

4. THEORETICAL MODEL AND SIMULATIONS OF SFG SPECTRA

$$a = 3\epsilon_1\epsilon_2\tau \left(-\frac{1}{i\omega_1 + \tau\omega_1^2} + \frac{1}{i\omega_2 + \tau\omega_2^2} \right) - \frac{\epsilon_1\epsilon_2\omega_1^2(i + \tau\omega_1)^2\omega_2^2(i + \tau\omega_2)^2\omega_3(i + \tau\omega_3) \left(\epsilon_3 \ln \left[\frac{\epsilon_1}{\epsilon_2} \right] + \epsilon_1 \ln \left[\frac{\epsilon_2}{\epsilon_3} \right] + \epsilon_2 \ln \left[\frac{\epsilon_3}{\epsilon_1} \right] \right)}{\tau^2(\omega_1 - \omega_2)(i + \tau(\omega_1 + \omega_2))(\omega_1 - \omega_3)(\omega_2 - \omega_3)(i + \tau(\omega_1 + \omega_3))(i + \tau(\omega_2 + \omega_3))\omega_p^4} \quad (4.38)$$

All equations are implemented in a Mathematic notebook, allowing for the calculation of the SF intensity.

4.2.7 Relative phases of different SFG sources

An experimentally very important parameter in SFG spectroscopy is the relative phase between the resonant and non-resonant $\chi^{(2)}$. Knowing this parameter makes the fitting procedure much easier. In general, there are two major influences on the phase: first, the optical path difference between the two SFG sources, and second, the absolute phase Φ of each source. The path difference in this work is usually neglected, since it is much smaller than any wavelength. Of greater interest are the absolute phases, defined as

$$\Phi = \arg(\chi_{ijk}^{(2)}) \quad (4.39)$$

Substituting in the values for gold will lead to a phase $\Phi_{gold,xxz} = -62^\circ$. This is dependent upon the parameters given for gold, with is the electron lifetime as the critical value. Higher electron densities and higher plasma frequencies do not influence the phase. Other $\chi_{gold,ijk}^{(2)}$ have slightly different values as well, meaning that with different polarization combinations the relative phase will be affected. For all the previously discussed resonant $\chi^{(2)}$ there will be $\Phi_{res,C_{3\nu}} = +90^\circ$. Therefore, the relative phase is $\Phi_{rel} = \Phi_{gold} - \Phi_{res,C_{3\nu}} \sim 152^\circ$.

4.3 Experimental confirmation

To verify the previous equations, an angle-dependent measurement of the vibrational and non-resonant SF generation was performed (Fig. 4.3). Both pulses were adjusted to 5 μ J and the angular separation between IR and visible input beams was $\sim 7^\circ$. The polarization configuration of the incident IR and visible beams were adjusted to a p-polarization by a set of polarizer and a half-wave plate.

For the SFG experiment, a thin water film ($\sim 1 \mu\text{m}$) was compressed between a gold wafer coated with a self-assembled monolayer of dodecanethiol (DDT; $\text{CH}_3(\text{CH}_2)_{11}\text{HS}$) and the basal face of an hemicylindrical CaF_2 prism. The DDT SAM was fabricated

using a standard procedure as described in section 3.1. The thin-layer cell was mounted on a goniometer such that the center of rotation was located at the beam overlap on the sample.

Both reflected and SFG beams were filtered through a short-pass filter and spectra were taken by full vertical binning with an acquisition time of 21 s. A polarizer was used to select the appropriate polarization state of the emitted SF beam. The SF beam was realigned and maximized following every rotation of the thin-layer cell. Spectral processing of the experimental data was performed via normalization to the non-resonant background signal from the gold substrate.

The SF signal intensity simulations were performed using the home-built program written in Mathematica (v.7.0, Wolfram Research, Canada) based on the equations given in section 4. This program took into account the fact that the measured resonant contributions were analyzed by normalization to the non-resonant background signal.

The SFG spectra of DDT-coated gold in water for different incidence angles are shown in Fig. 4.3. These spectra are very similar to previously published results similar samples.[21]

4.4 Simulations and Discussions

For the simulation of the measured spectra the wavelengths were set to $\lambda_{\text{VIS}} = 800\text{nm}$, $\lambda_{\text{IR}} = 3400\text{nm}$ and $\lambda_{\text{SFG}} = 652\text{nm}$. The optical material properties of water were taken from [22, 23, 24, 25] to be $n(\text{VIS}) = 1.329 + 1.4 \cdot 10^{-7}i$, $n(\text{SFG}) = 1.331 + 1.4 \cdot 10^{-7}i$ and $n(\text{IR}) = 1.34 + 0.0005i$, CaF_2 to be $n(\text{VIS}) = 1.43053$, $n(\text{SFG}) = 1.43248$ and $n(\text{IR}) = 1.4154$ and for gold from [26] to be $n(\text{VIS}) = 0.16 + 5.39i$, $n(\text{SFG}) = 0.19 + 3i$ and $n(\text{IR}) = 1.9 + 21i$. The optical constants of the polymer film based on values obtained by ellipsometry were $n(\text{VIS}, \text{SFG}) = 1.5 + 0.0001i$ and $n(\text{IR}) = 1.5 + 0.01i$. The twist angle ψ and the azimuthal angle ϕ were assumed to be isotropically distributed. The five non-vanishing molecular elements of $\beta_{\alpha\beta\gamma}$ were all set to $1 \cdot 10^{-26} \text{ m}^4 \text{ V}^{-1} \text{ s}^{-1}$, since in literature the different hyperpolarizabilities tensor elements are usually all of the same order of magnitude, and differ by maximum by factor of five.[16, 27, 28]

Simulations for the non-resonant gold signal and both the symmetric and asymmetric stretch were performed and plotted together with the experimental data (see Fig. 4.3). Using the chosen parameters, the non-resonant signal fit with the data, although the values depended heavily on the thickness of the water film. The only remaining free parameter for the simulations of the resonant SFG was the molecular polar angle θ , which was determined via fitting the experimental data to be $\sim 20^\circ$.

4. THEORETICAL MODEL AND SIMULATIONS OF SFG SPECTRA

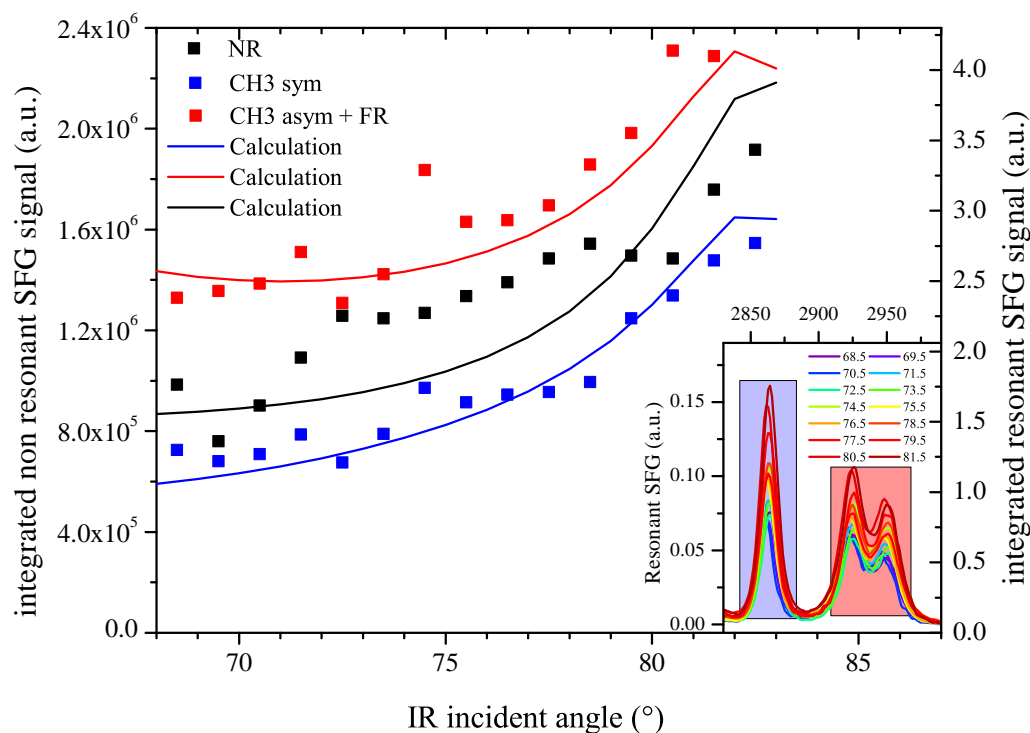


Figure 4.3: Integrated area of resonant CH_3 stretching peaks and non-resonant background from DDT-coated Au in water for *ppp* polarization at different incidence angles. - Points and curves denotes experimental and simulated data, respectively. The inset shows SF spectra of DDT-coated Au in water for *ppp* polarization at different incidence angles. The maxima in the spectra are assigned to the following vibrational modes: symmetric CH_3 stretching at 2880 cm^{-1} and its Fermi resonance at 2914 cm^{-1} , and asymmetric CH_3 stretching at 2954 cm^{-1} . The water film thickness was about 600 nm.

Since the initial simulations fit well with the measurements, further simulations were performed to obtain a general view on how the SF signal can be influenced by several parameters such as, incident angle, composition of the sample layer, molecular orientation, and different polarization combinations.

4.4.1 Dependence of SF intensity on film thickness

The SF intensity depends on the incident electric fields. Electric field amplitudes of p-polarized light inside a multi layer stack were calculated and are shown in Fig. 4.4 as function of depth inside the aqueous media and polymer film. The dimensions are chosen to roughly match an average sample of pNIPAM. A discontinuity of the amplitude over the interface is clearly observable. Furthermore, the gap in amplitude between the forward and backward traveling EM wave shown on the right (b) fits with the loss of amplitude which occurs in the thin layer.

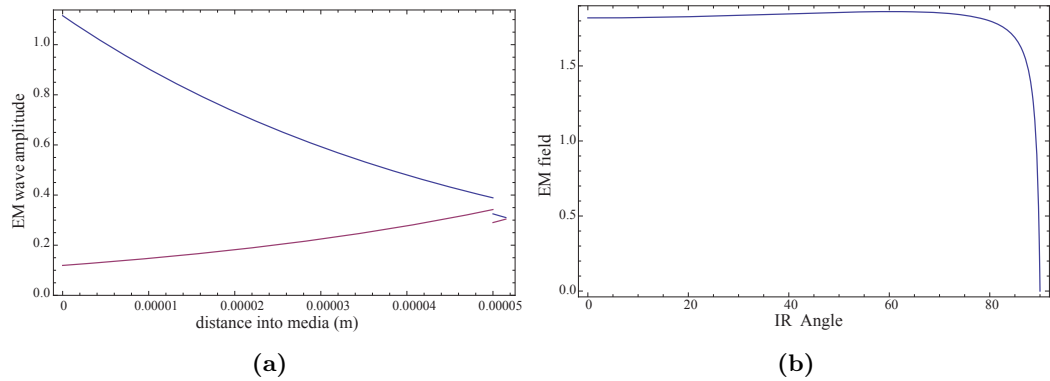


Figure 4.4: (a) Simulated amplitude of downward- (*blue*) and upward- (*purple*) propagating \mathbf{E} field fields as function of depth. (b) \mathbf{E} field amplitude as function of IR incidence angle.

Both the water film thickness and the incident angle are combined in the simulations shown in Fig. 4.5. Since we already know from Fig. 4.4 how the field amplitude decreases due to absorption, the thickness parameter in this simulation is only varied between 0.1 and 2.0 μm . In this range the interference effects will be visible. The sample stage geometry allowed for an easy tilting of the sample, permitting the IR and VIS to be changed in parallel during this angle dependent experiment. The IR angle was always kept 7° smaller than the VIS angle. The molecular angles were fixed to $\theta = 30^\circ$ and $\phi = 15^\circ$ and β_{ijk} are all set to $1 \cdot 10^{-22}$.

The thickness of the water film needs to be about 1 μm in order to get the best

4. THEORETICAL MODEL AND SIMULATIONS OF SFG SPECTRA

signal for the *ppp* polarization at the most commonly used incident angle of about 60° . The minima at $\sim 30^\circ$ incident angle is a function of the molecular polar angle θ and can be shifted to every other angle. The angular dependence of the non-resonant SF signal is comparable in each polarization combination, however the water film thickness has different effects, especially for water films on the order of the wavelength. There is a huge signal for *ppp* for the angle of 83° , where total internal reflection is occurring for water films of about 500 nm. The narrow fringes appearing in the molecular SF simulations are due to multiple reflections of the resonantly generated SF beam in between the gold and the CaF_2 /water interface, and are most pronounced for thicknesses on the order of the wavelength.

4.4.2 Dependence of SF intensity on molecular angles

The following simulations showing the dependency of the SF response as function of the polar molecular angle θ in Fig. 4.6 and the azimuthal angle ϕ in Fig. 4.8 are important for the orientational interpretation of SFG spectra. The water film was set to 1.0 μm .

First as shown in Fig. 4.6, there is no SFG for *sps* symmetric and *ssp* asymmetric resonances. The asymmetric resonance could be triggered if the azimuthal angle was tuned away from zero degree. (see Fig. 4.7) However, this would still not result in the appearance of the *sps* symmetric resonance. This allows on to distinguish between those two modes. Other than this effect, the results do not changing much by setting the azimuthal angle ϕ to 30° from the normal. Another general rule for SFG spectroscopy is that in all simulated spectra other than *ppp* asymmetric, no SFG will be generated at the combinations of same polar and incident angles.

There are particular azimuthal angles where no SF can be generated. But the dynamic for the azimuthal angle it is a bit more complicated; an increase of a signal does not necessarily indicate an increase of the angle. Depending on the initial angular conformation either an increase or decrease could result.

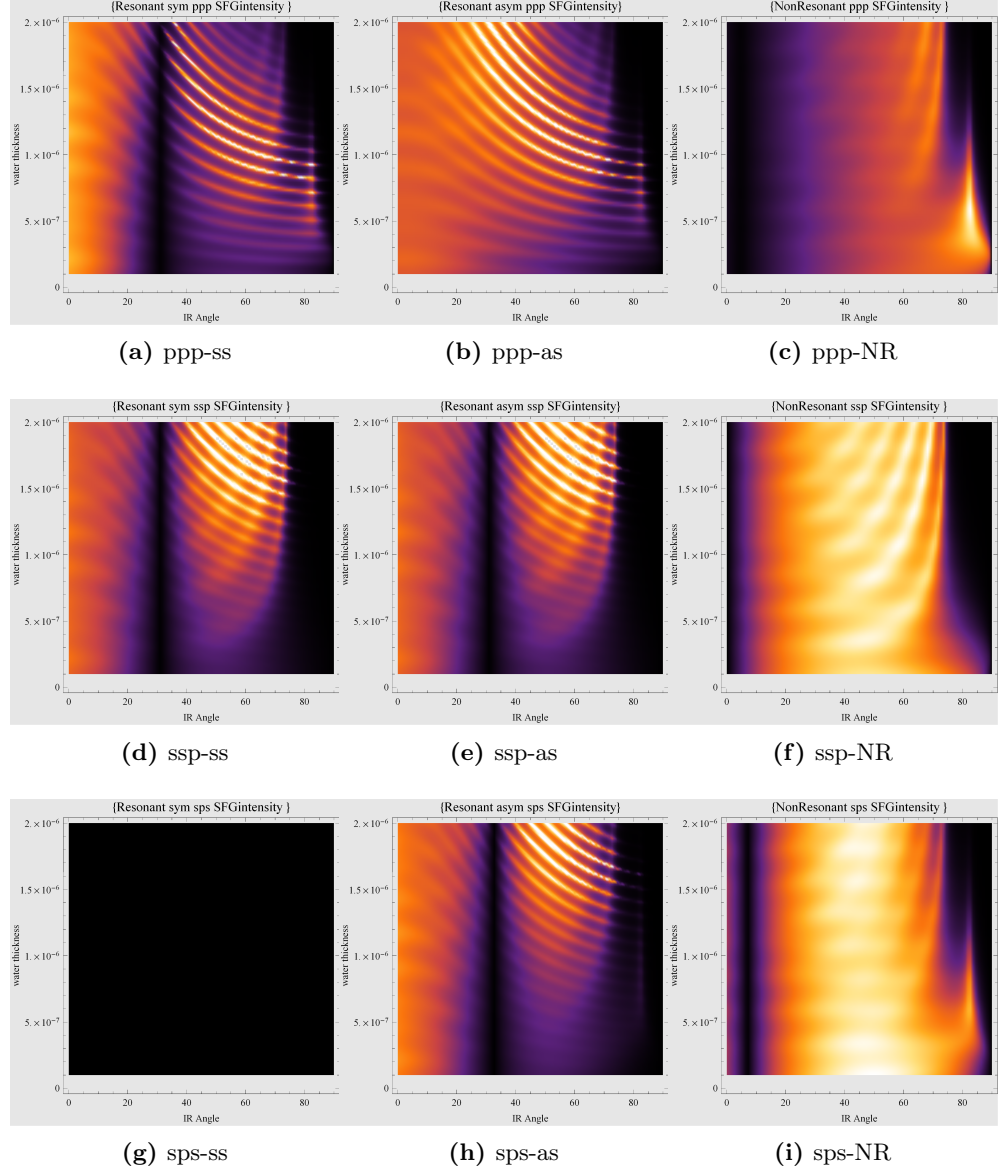


Figure 4.5: Simulated SFG intensity of CH_3 stretching vibrational modes as function of incidence angle from a thin layer model for various water film thicknesses (0.1-2.0 μm) for *ppp*, *ssp*, and *sps* polarizations. Molecular angles are set to polar tilt $\theta = 30^\circ$ and azimuthal turn $\phi = 15^\circ$. (a,d,g) resonant symmetric stretching *ss*, (b,e,h) resonant asymmetric stretching *as* and (c,f,i) non-resonant background

4. THEORETICAL MODEL AND SIMULATIONS OF SFG SPECTRA

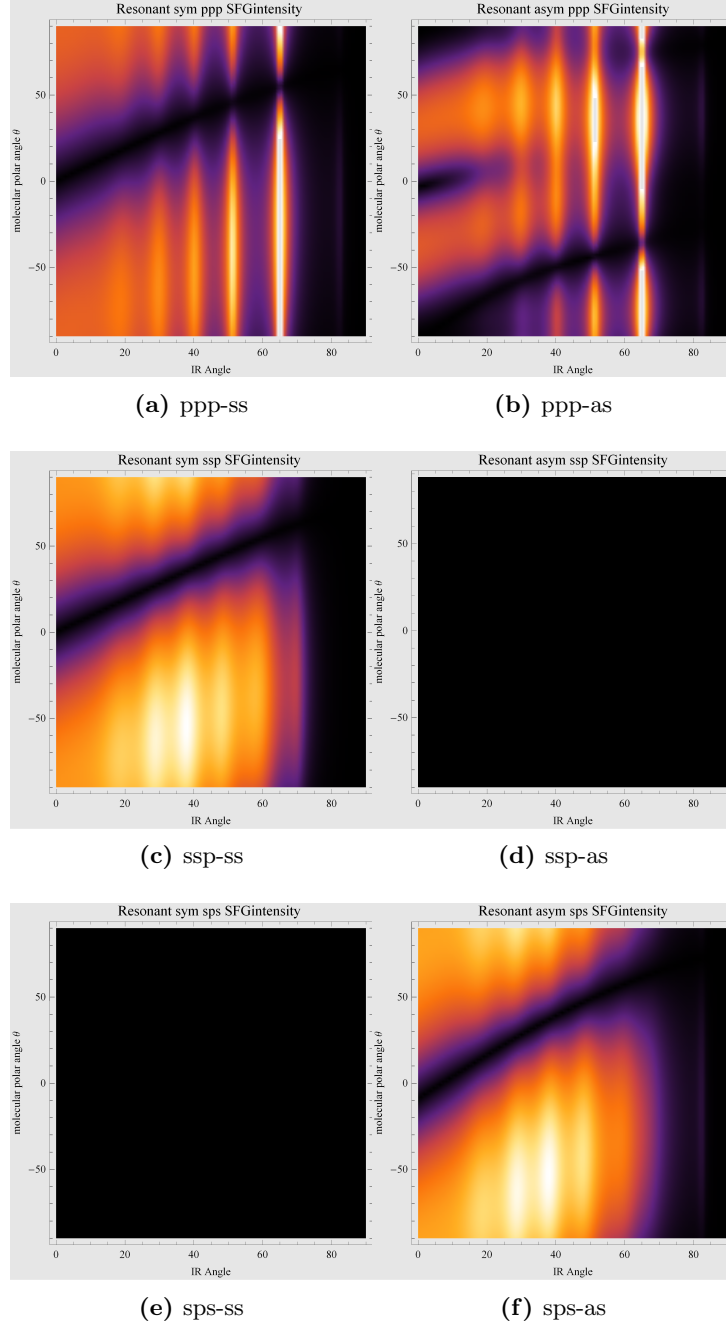


Figure 4.6: Simulated SFG intensity of asymmetric and symmetric CH_3 stretching vibrational modes as function of polar angle θ from a thin layer model with water film thickness $1.0 \mu\text{m}$ and for *ppp*, *ssp*, and *sps* polarizations. (a,c,e) resonant symmetric stretching, (b,d,f) resonant asymmetric stretching. The azimuthal angle ϕ is fixed at 0° .

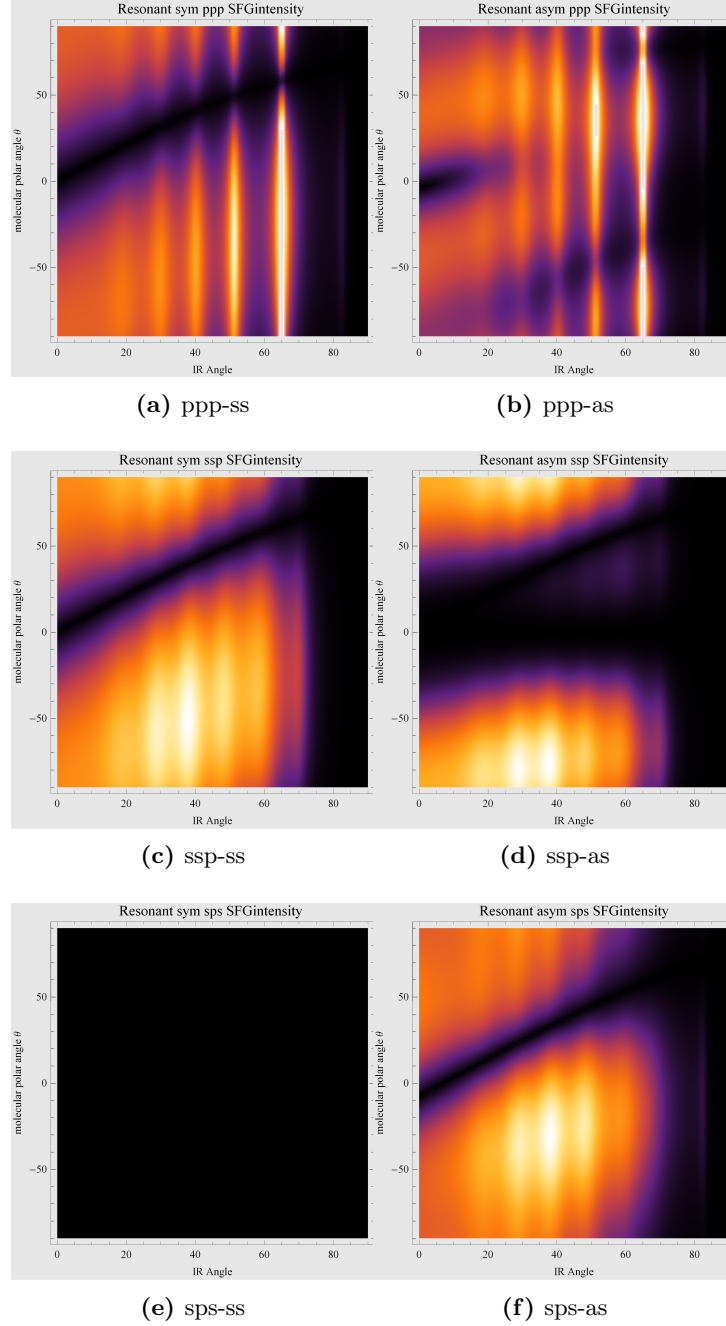


Figure 4.7: Simulated SFG intensity of asymmetric and symmetric CH_3 stretching vibrational modes as function of polar angle θ from a thin layer model with water film thickness $1.0 \mu\text{m}$ and for *ppp*, *ssp*, and *sps* polarizations. (a,c,e) resonant symmetric stretching, (b,d,f) resonant asymmetric stretching. The azimuthal angle ϕ is fixed at 30° .

4. THEORETICAL MODEL AND SIMULATIONS OF SFG SPECTRA

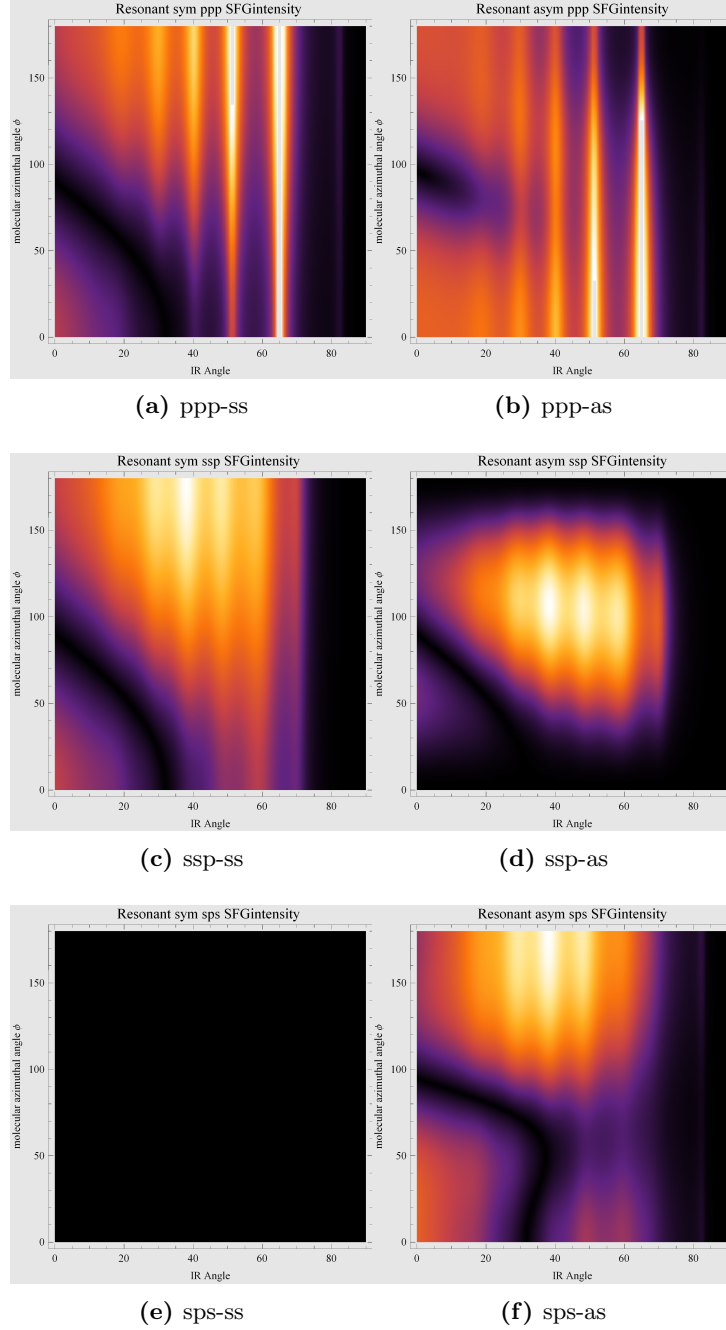


Figure 4.8: Simulated SFG intensity of asymmetric and symmetric CH_3 stretching vibrational modes as function of twist angle ϕ from a thin layer model with water film thickness $1.0 \mu\text{m}$ and for *ppp*, *ssp*, and *sps* polarizations. (a,c,e) resonant symmetric stretching, (b,d,f) resonant asymmetric stretching. The polar angle θ is fixed at 30° .

References

- [1] M.-O. Diesner, C. Howell, V. Kurz, D. Verreault, and P. Koelsch, “In vitro characterization of surface properties through living cells,” *J. Phys. Chem. Let.*, vol. 1, pp. 2339–2342, 2010. [59](#)
- [2] V. Kurz, M. Grunze, and P. Koelsch, “In-situ characterization of thermo-responsive poly(*n*-isopropylacrylamide) films with sum-frequency generation spectroscopy,” *ChemPhysChem*, vol. 11, pp. 1425–1429, 2010. [59](#)
- [3] C. Hirose, H. Ishida, K. Iwatsu, N. Watanabe, J. Kubota, A. Wada, and K. Domen, “*In situ* sfg spectroscopy fo film growth. i. general formulation and the analysis of the signal observed during the deposition of formic acid on pt(110)-(1×2) surface,” *J. Chem. Phys.*, vol. 108, pp. 5948–5956, 1998. [59](#)
- [4] A. G. Lambert, D. J. Neivandt, A. M. Briggs, E. W. Usadi, and P. B. Davies, “Interference effects in sum frequency spectra from monolayers on composite dielectric/metal substrates,” *J. Phys. Chem. B*, vol. 106, pp. 5461–5469, 2002. [59](#)
- [5] S. J. McGall, P. B. Davies, and D. J. Neivandt, “Interference effects in sum frequency vibrational spectra of thin polymer films: an experimental and modeling investigation,” *J. Phys. Chem. B*, vol. 108, pp. 16030–16039, 2004. [59](#)
- [6] W. S. Kolthammer, D. Barnard, N. Carlson, A. D. Edens, N. A. Miller, and P. N. Saeta, “Harmonic generation in thin films and multilayers,” *Phys. Rev. B*, vol. 72, p. 045446, 2005. [59](#)
- [7] Y. Tong, Y. Zhao, N. Li, M. Osawa, P. B. Davies, and S. Ye, “Interference effects in the sum frequency generation spectra of thin organic films. i. theoretical modeling and simulation,” *J. Chem. Phys.*, vol. 133, pp. 034704/1–034704/13, 2010. [59](#)
- [8] J. Löbau and K. Wolfrum, “Sum-frequency spectroscopy in total internal reflection geometry: Signal enhancement and access to molecular properties,” *J. Opt. Soc. Amer. B*, vol. 14, pp. 2505–2512, 1997. [60](#)
- [9] R. L. York, Y. Li, G. J. Holinga, and G. A. Somorjai, “Sum frequency generation vibrational spectra: the influence of experimental geometry for an absorptive medium or media,” *J. Phys. Chem. A*, vol. 113, no. 12, pp. 2768–2774, 2009. [60](#)
- [10] D. S. Bethune, “Optical harmonic generation and mixing in multilayer media: analysis using optical transfer matrix techniques,” *J. Opt. Soc. Am. B*, vol. 6, pp. 910–916, 1989. [60](#)
- [11] N. Hashizume, M. Ohashi, T. Kondo, and R. Ito, “Optical harmonic generation in multi-layered structures: a comprehensive analysis,” *J. Opt. Soc. Am. B*, vol. 12, pp. 1894–1904, 1995. [60](#)

REFERENCES

- [12] F. Abelès, “Recherches sur la propagation des ondes électromagnétiques sinusoïdales dans les milieux stratifiés: application aux couches minces,” *Ann. Phys. (Paris)*, vol. 5, pp. 598–640, 1950. [61](#)
- [13] O. S. Heavens, *Optical Properties of Thin Films*. Dover, 1965. [61](#)
- [14] P. Yeh, *Optical Waves in Layered Media*. John Wiley & Sons, 2005. [61](#)
- [15] J. E. Sipe, “New green-function formalism for surface optics,” *J. Opt. Soc. Am. B*, vol. 4, pp. 481–489, 1987. [68](#)
- [16] X. Zhuang, P. B. Miranda, D. Kim, and Y. R. Shen, “Mapping molecular orientation and conformation at interfaces by surface nonlinear optics,” *Phys. Rev. B*, vol. 59, pp. 12632–12640, 1999. [69](#), [75](#)
- [17] C. Hirose, N. Akamatsu, and K. Domen, “Formulas for the analysis of the surface sfg spectrum and transformation coefficients of cartesian sfg tensor components,” *Appl. Spectr.*, vol. 46, pp. 1051–1072, 1992. [70](#), [71](#)
- [18] C. Flytzanis, “Infrared dispersion of second-order electric susceptibilities in semiconducting compounds,” *Physical Review B*, vol. 6, p. 1264, 1972. [70](#)
- [19] A. V. Petukhov, “Sum-frequency generation on isotropic surfaces: General phenomenology and microscopic theory for jellium surfaces,” *Phys. Rev. B*, vol. 52, pp. 16901–16911, Dec 1995. [72](#)
- [20] R. A. Innes and J. R. Sambles, “Optical characterisation of gold using surface plasmon-polaritons,” *J. Phys. F: Met. Phys.*, vol. 17, pp. 277–287, 1987. [73](#)
- [21] C. Howell, R. Maul, W. Wenzel, and P. Koelsch, “Interactions of hydrophobic and hydrophilic self-assembled monolayers with water as probed by sum-frequency-generation spectroscopy,” *Chem. Phys. Lett.*, vol. 494(4-6), pp. 193–197, 2010. [75](#)
- [22] G. M. Hale and M. R. Querry, “Optical constants of water in the 200-nm to 200- μ m wavelength region,” *Appl. Opt.*, vol. 12, no. 3, pp. 555–563, 1973. [75](#)
- [23] W. M. Irvine and J. B. Pollack, “Infrared optical properties of water and ice spheres,” *Icarus*, vol. 8, no. 1-3, pp. 324 – 360, 1968. [75](#)
- [24] M. R. Querry, B. Curnutie, and D. Williams, “Refractive index of water in the infrared,” *J. Opt. Soc. Am.*, vol. 59, no. 10, pp. 1299–1304, 1969. [75](#)
- [25] J. E. Bertie and Z. Lan, “Infrared intensities of liquids xx: The intensity of the oh stretching band of liquid water revisited, and the best current values of the optical constants of h₂o(l) at 25°C between 15,000 and 1 cm⁻¹,” *Appl. Spectrosc.*, vol. 50, no. 8, pp. 1047–1057, 1996. [75](#)

REFERENCES

- [26] L. G. Schulz and F. R. Tangherlini, “Optical constants of silver, gold, copper, and aluminum. ii. the index of refraction n ,” *J. Opt. Soc. Am.*, vol. 44, no. 5, pp. 362–367, 1954. [75](#)
- [27] C. Hirose, N. Akamatsu, and K. Domen, “Formulas for the analysis of surface sum-frequency generation spectrum by ch stretching modes of methyl and methylene groups,” *J. Chem. Phys.*, vol. 2, pp. 997–1004, 1992. [75](#)
- [28] X. Wei, S.-C. Hong, X. Zhuang, T. Goto, and Y. R. Shen, “Nonlinear optical studies of liquid crystal alignment on a rubbed polyvinyl alcohol surface,” *Physical Review E*, vol. 62, pp. 5160–5172, 2000. [75](#)

REFERENCES

5

Results & Discussion of poly-N-isopropylacrylamide

The molecular arrangement of ultrathin pNIPAM around the LCST was investigated and correlated with the macroscopic behavior, at various thicknesses. *In situ* broadband SFG spectroscopy, ellipsometry and contact angle measurements were applied. The characterization was performed not only below and above the LCST, but at small temperature steps between 20° and 40°C. The accuracy of the SFG data analysis was verified by comparison to ellipsometry and contact angle, as well as Raman and infrared reflection absorption spectra (IRRAS). Furthermore, visualization of the SFG spectra using generalized 2D-correlation spectroscopy analysis allows for the quantification of which vibrational bands were most affected by the perturbation as well as the deduction of a sequential order for the molecular rearrangements.

5.1 Ellipsometry

The ellipsometric data was acquired for films of a thickness above 50 nm and is shown in Fig. 5.1. The fitted thickness in the collapsed state are shown in the legend, with the thicknesses in air given in parenthesis. While the temperature of the liquid cell and the sample was slowly ramped up, the data was acquired using a Multiskop in the Nullellipsometer mode. Every 0.5°C one set of ellipsometric angles was recorded. The ellipsometer was slightly readjusted to compensate for thermal drifts every 0.5°C. Measurements at lower than 10°C were not possible due to water vapor condensation on the windows and those above 50°C were hindered by bubbles building up inside the liquid cell.

5. RESULTS & DISCUSSION OF POLY-N-ISOPROPYLACRYLAMIDE

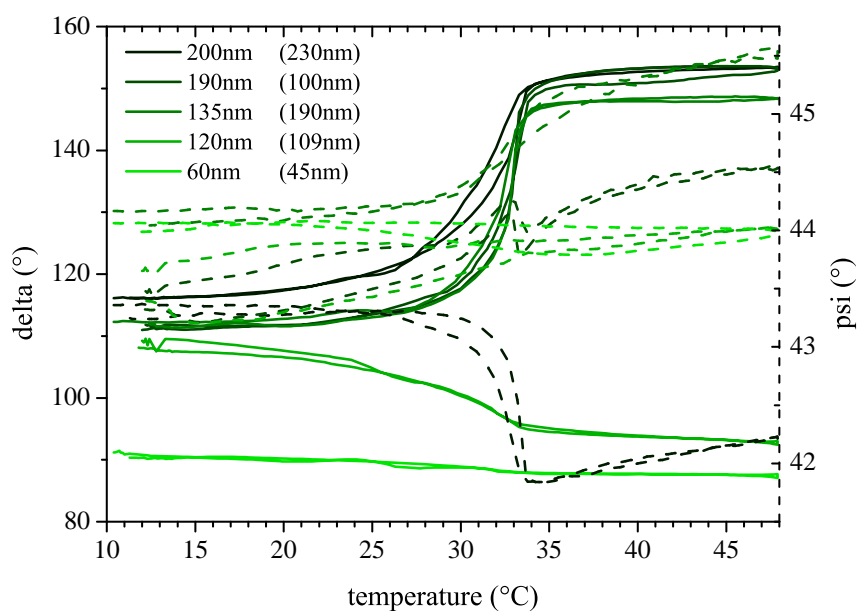


Figure 5.1: *In situ* ellipsometric of data pNIPAM films of different thicknesses
- in the legend: fitted thickness in the collapsed state and in parenthesis thickness in air.
The differences are most likely due to different variations between areas of the sample

The Ψ and Δ values can not tell anything quantitatively, but the dynamics for the Δ values can be observed. The slope of the curve starts changing slowly at 25°C, becoming steeper at around 32°C. There is a slow transition at the beginning, followed by a rapid transition as the LCST is approached. After the collapse at 32°C the film is stabilized and remains in the segregated phase.

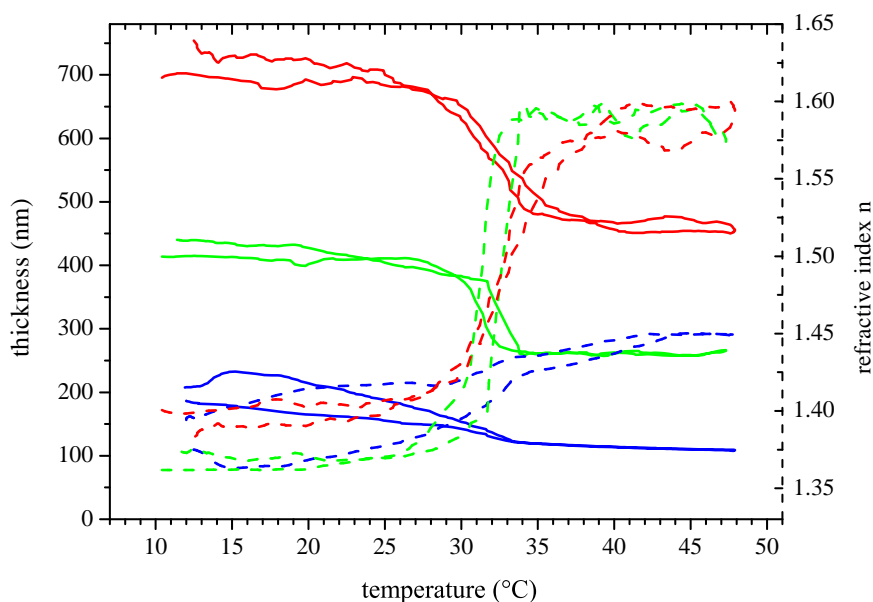


Figure 5.2: Fits of Ellipsometric data for thickness and refractive index of pNIPAM films of different thickness - (dashed) refractive index, (solid thickness)

In order to fit the ellipsometric data, a four layer model was made. This consisted of a silicon substrate, a gold film 80 nm thick, pNIPAM with both thickness and refractive index as free parameters, and an infinite water layer on top. It was assumed, that there was no temperature dependence for the thicknesses and refractive indices for any of the materials other than the pNIPAM. A simulation with a dataset for the temperature dependence of the water refractive index showed no significant impact on the ellipsometric data. In Fig. 5.2 the fits of selected films are presented. The solid lines show the thickness and the dashed lines the refractive index. The fits are not as smooth as the raw data, which is due to the fitting routing used by the software provided with the Multiskop. Finding a good fit for each temperature point is quite tedious and good boundaries for the parameters need to be given. Furthermore, there is no way in which to correct for slight thermally induced misalignments, which may

5. RESULTS & DISCUSSION OF POLY-N-ISOPROPYLACRYLAMIDE

lead to different incident angles on the windows of the sample cell.

All films show the expected LCST transition and decrease their thicknesses by about 30%. The shrinking of the films starts at about 25°C, but above the LCST, the film thicknesses are constant. The refractive index below the LCST is quite close to that of water (1.33257), since a significant amount of water is incorporated inside the polymer chains. Above the LCST, the water is repelled and the solid segregated polymer phase remains with a higher refractive index $n \sim 1.4$ – 1.6 . This process is highly reproducible and only shows a very small degree of hysteresis due to the placement of the temperature sensor and the acquiring of data not at an equilibrated temperature.

5.2 IRRAS and Raman spectroscopy

The pNIPAM films were investigated by IRRAS and with Raman spectroscopy in order to obtain survey spectra for the estimation of SFG intensities. In Raman spectroscopy the signal increases with increased scattering, meaning that the samples of only few nm thickness did not give sufficient signal intensity with the spectrometer used. Spin-coated pNIPAM films a few μm thick were prepared and measured instead. The resulting spectra are shown in Fig. 5.3 and corresponding peak locations and assignments are listed in Table 5.1. The C=O, NH, CC, CO, CN, and CH₂ and CH₃ vibrations are located in the spectral region from 1000–1750 cm⁻¹, whereas peaks the spectral region between 2800–3000 cm⁻¹ emanate exclusively from CH₂ and CH₃ stretching vibrations. Additionally, the region above 3000 cm⁻¹ displays vibrations from NH, amide I and II overtones, amide B, and OH from residual water in the pNIPAM film. Regions, where both IR and Raman intensities are present will be investigated further with SFG spectroscopy.

The IR intensity for the films of different thickness directly polymerized on the surface (section 3.3.3) is shown in Fig. 5.4. Some minor differences between the spin coated and the ATRP pNIPAM films are observable. These are due to the presence of a small amount of other chemical specimens from the polymerization process, as well as and different conformational variations which occur in a thin film grown on a surface, rather than a polymerization in solution without steric restrictions. The intensities of the signal depend on the position of the laser spot and can change up to $\pm 30\%$ due to film inhomogeneities. Despite these issues, the absorption correlates well with the thickness values determined by ellipsometry. The difference in absorbance in both IRRAS spectra also fits well with the different thicknesses of spin coated and ATRP films.

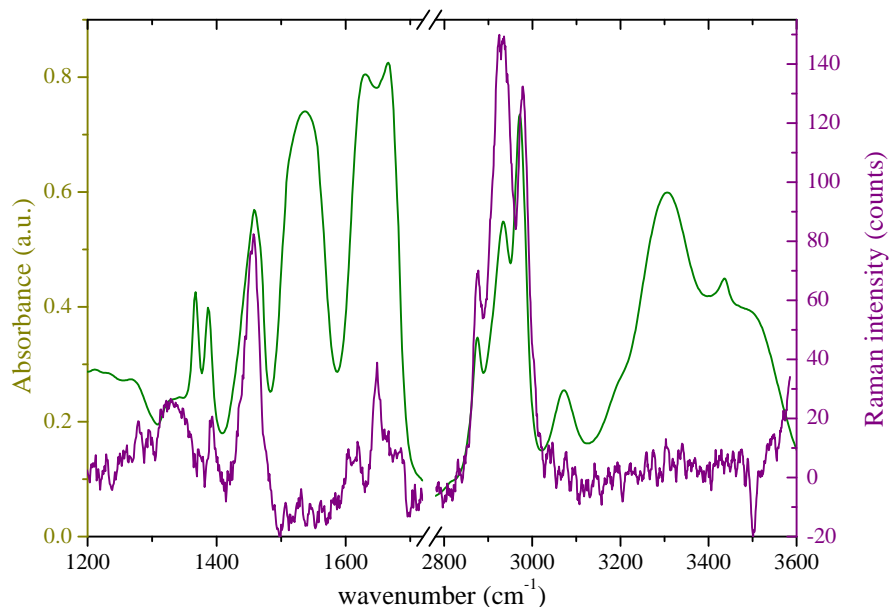


Figure 5.3: IR and Raman spectra of spin coated pNIPAM films on gold - IRRAS (green line) and Raman (purple line)

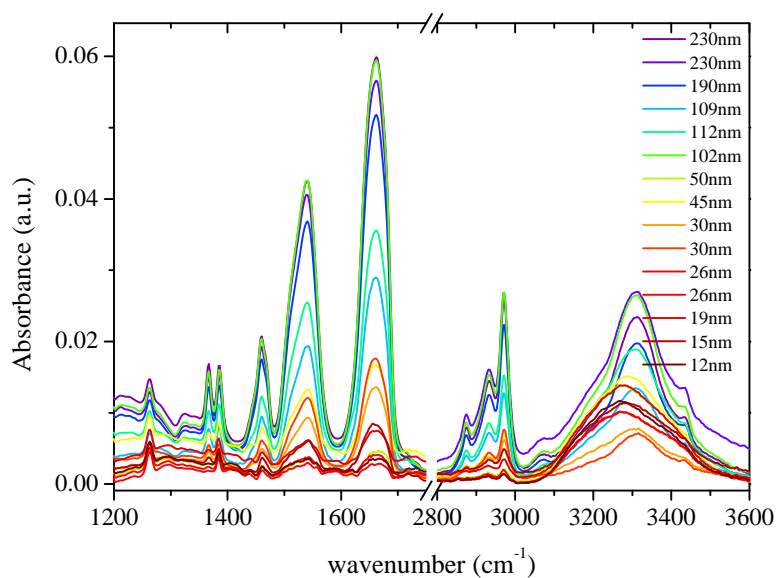


Figure 5.4: IR spectra of pNIPAM films of different thickness polymerized on a surface - (blue) thicker, (red) thinner. The exact thickness measured in air are given in the caption.

5. RESULTS & DISCUSSION OF POLY-N-ISOPROPYLACRYLAMIDE

compound	IR	Raman	description
$\nu(\text{N-H})_b$	3305		Bonded
$\nu(\text{N-H})_f$	3432		Free
Amide I + Amide II	3185		Overtone
Amide B	3060		
$\nu_{as}(\text{CH}_3)$	2968	2968	
$\nu_{as}(\text{CH}_2)$	2927	2927	
$\nu_s(\text{CH}_3)$	2871	2871	
Amide I	1660	1642	-CO...HN-(IR) C=O (Raman)
Amide II	1540	1554	-CONH-(IR) N-H (Raman)
$\delta_{as}(\text{CH}_3)$	1460	1453	bend (scissors deformation)
$\delta_{as}(\text{CH}_2)$	1450		
$\delta_s(\text{CH}_3)$	1387		
$\delta_s(\text{CH}_2)$	1280		
Amide III	1280		
N-C		1160	Stretch
C-C		1131	Skeletal in-phase stretch

Table 5.1: IR[1] and Raman[2, 3] peak assignments of spin coated pNIPAM films.

5.3 Contact angle

To investigate the chemical potentials of the surface, *in situ* captive bubble contact angle measurements were performed. In this technique an equilibrium contact angle is achieved due to a slow uptake or release of water at the water vapor saturated air bubble.[4] In these experiments, a series was performed in which new air bubbles were made for every temperature step on different spots of the 13 nm sample, keeping the entire surface in contact with the water in order to achieve equilibration. The results were similar to experiments performed where only one bubble with an equilibration time of 60 seconds was measured during the entire series, (see the curves for the 13 nm thick film in Fig 5.5). The standard error for these test was quite large, originating mostly from the inhomogeneities of the pNIPAM coating, also observed with IRRAS. The 19 nm thick film was measured during both heating and cooling. A hysteresis of the contact angle due to incompletely equilibrium is observable, since there is no advancing and receding captive contact angle. The small steps in the measurements are due to the poor image resolution of the digital images, as the bubble was only about 120 pixels in height. During the temperature series the position of the bubble on the CCD image was changed by up to five pixels, requiring five readjustments of the baseline and resulting in five small jumps in the curves. The errors are typically in the order of $\pm 2^\circ$ and become smaller with larger contact angles. These errors are only shown for a few data points for clarity, shown as the standard deviation of the contact angle obtained from several bubbles on the same sample.

The thicker the film, the smaller the captive contact angle, in agreement with the findings of other studies examining the advancing contact angle.[5] The thick films are more hydrophilic due to orienting the hydrophobic groups to the inside of the polymer and exposing the hydrophilic groups to the water. For less dense and thinner films there are more single brushes, which can expose their hydrophobic groups to the water due to less steric restrictions. More surprising is that there is no strong distinct transition for any film measured. This result has been already predicted by R. Pelton[6], although it is still somewhat surprising given that it is in contrast to almost all studies using the advancing sessile drop contact angle method. Only the 2.5 nm thick film with 5% grafting density exhibits a small 2° transition of the contact angle (see inset of Fig. 5.5). The overall decrease in contact angles with temperature is in contrast to the previous results from Cheng et al., which were done on plasma-polymerized pNIPAM films.[7] This can be explained by the complexity of the origin of the contact angle, where the chemical potentials of the water and the polymer, as well as excess entropy,

5. RESULTS & DISCUSSION OF POLY-N-ISOPROPYLACRYLAMIDE

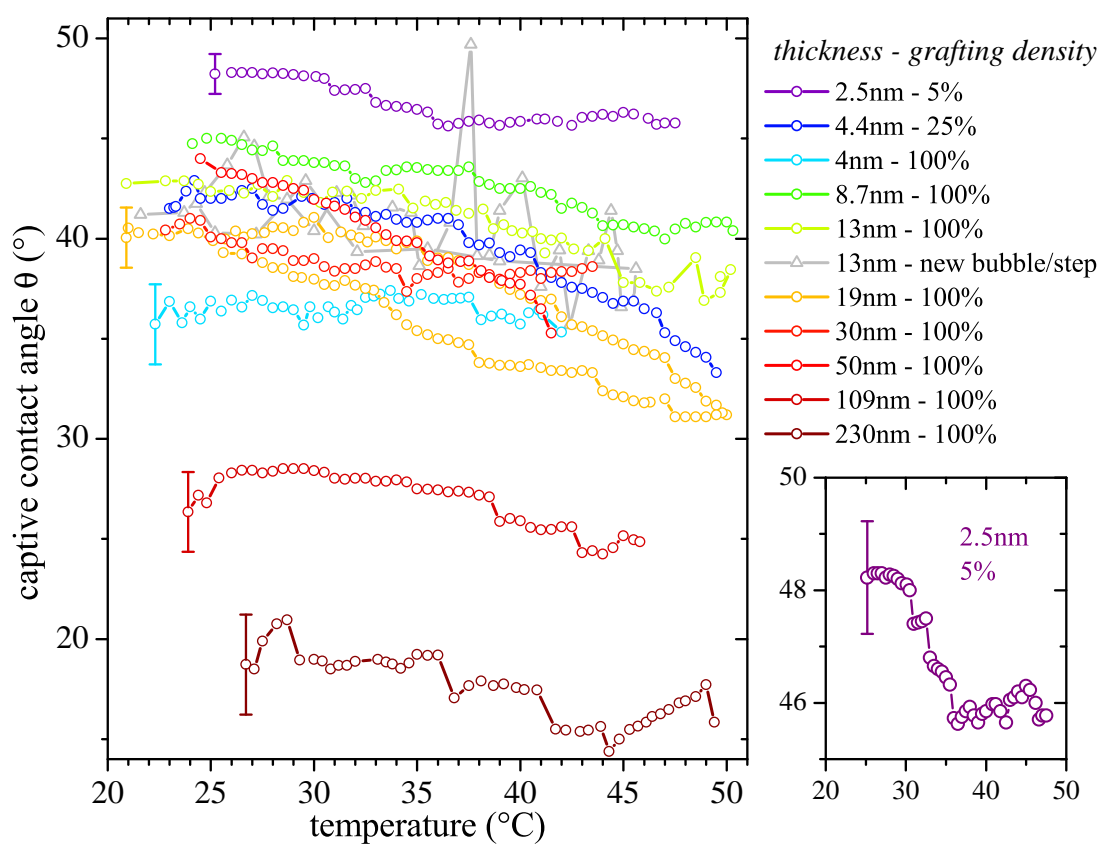


Figure 5.5: Captive bubble contact angle of various pNIPAM films as function of temperature - from thin (blue) to thick (red)

can contribute. For example, the change of entropy upon the LCST depends strongly on the grafting density, the thickness, and the way in which the polymer brushes are synthesized. These properties may also differ from sample to sample.

5.4 SFG of the CH stretching region

5.4.1 NBT-modified pNIPAM

SFG is applied to probe molecular orientation changes. Spectra of different surface initiated ATRP NBT-pNIPAM films on Au were recorded in D₂O solution from well below the LCST to 45°C (above the LCST). Fig. 5.6(a) shows the SFG intensity and fits at various temperatures from a pNIPAM film (see section 3.3.1) acquired with *ppp* polarization combination. In Table 5.2, the corresponding peak positions of pNIPAM below and above the LCST are listed. In this region, spectral contributions are emanating exclusively from CH, CH₂ and CH₃ stretching vibrations. The peak locations themselves are not affected by the LCST phase transition, whereas the peak intensities are significantly changing. Fig. 5.6(b) shows the SFG spectrum before and after the LCST for clarity. The most prominent changes can be observed for the methyl vibrations, which increase significantly as the temperature rises.

In the polarization combination used (*ppp*) and an incident angle of $\sim 60^\circ$ for IR and VIS, the intensities for a symmetric and asymmetric CH₃ stretch are calculated in Fig. 4.6a and 4.6b as function of the polar molecular angle, which is assumed to be changed upon the film collapse. In Figure 4.7a and 4.7b the intensities are also calculated for a small azimuthal twists. In the measured data both vibrational modes (asym. and sym) increase by roughly the same amount, however calculations for this special case predict that one mode can only increase if the other stays constant or decreases. Therefore, the strong enhancement of both the CH₃ stretches in the collapsed state of pNIPAM above the LCST is due to a gain in order of this particular molecular group. This is not unexpected, as in the collapsed state a distinct interface between polymer and water is built. To built an stable hydrophobic interface only the non-polar methyl groups can direct themselves towards the liquid phase. A different average polar angle of the methyl of up to $\sim 20^\circ$ can also be involved.

The three CH₃ peaks at 2975 cm⁻¹, 2985 cm⁻¹ and 2992 cm⁻¹ are associated with the isopropyl groups in the polymer side chains. These features were also found in IR and Raman spectra of isopropyl-formate and its deuterated isotopomers.[10]

The relation between the various contributions in the SFG spectra of Fig. 5.6 can be further visualized using perturbation-based 2D correlation spectroscopy.[11] Fig. 5.7

5. RESULTS & DISCUSSION OF POLY-N-ISOPROPYLACRYLAMIDE

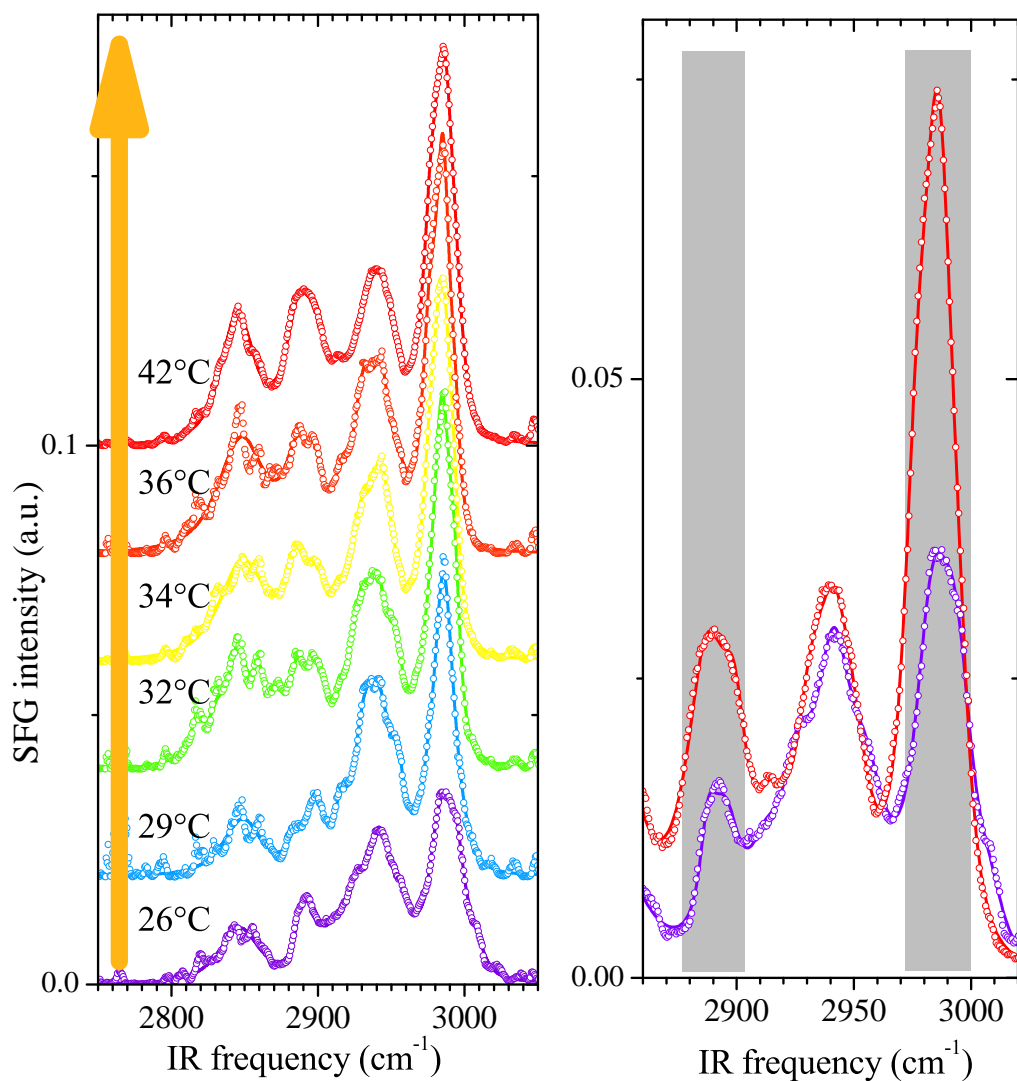


Figure 5.6: NBT modified pNIPAM SFG spectra - In situ spectra in D_2O solution during a temperature sweep from 26° - 42° . Measured spectra and lists are represented as open circles and solid lines, respectively. (b): SFG spectra at 26° (lower curve) and 42° (upper curve) for direct comparison.

5.4 SFG of the CH stretching region

compound	24°C	42°C	Ref.
CH ₂ s	2857	2857	[8]
CH ₃ FR	2889	2887	[9]
CH ₃ s	2943	2941	[10]
CH ₃ as	-	2975	[10]
CH ₃ as	-	2985	[10]
CH ₃ as	2992	-	[10]

Table 5.2: s: symmetric, as: asymmetric, FR: Fermi resonance. Measured peak positions below and above the LCST.

shows a synchronous 2D SFG correlation spectrum in the CH stretching region. Autopoints, appearing at diagonal positions in Fig. 5.8, represent the spectral intensity changes for these bands during the temperature sweep. The most prominent autopoint can be observed for CH₃ contributions around 2980 cm⁻¹, showing that this vibrational band is most affected by the LCST.

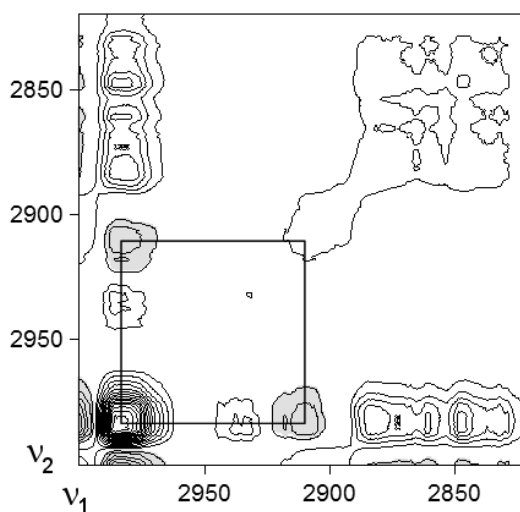


Figure 5.7: Synchronous 2D SFG correlation spectrum - Negative peaks are shaded grey.

Negative cross peaks indicate that the band intensity of one conformation is increasing while the intensity for the other conformation is decreasing. The only negative crosspeaks can be observed at 2914 cm⁻¹ and 2992 cm⁻¹; all other crosspeaks are positive. The peak at 2914 cm⁻¹ may be associated with CH₂ vibrations in the polymer

5. RESULTS & DISCUSSION OF POLY-N-ISOPROPYLACRYLAMIDE

main chain.[9] The peak at 2992 cm^{-1} was found in IR and Raman spectra of crystalline isopropyl-formates.

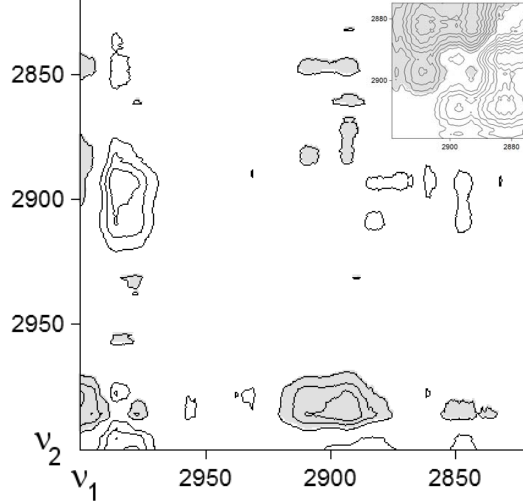


Figure 5.8: Asynchronous 2D SFG correlation spectrum - Negative peaks are grey shaded. The inset shows magnification between 2875 cm^{-1} and 2920 cm^{-1} .

To further analyze the sequential order, we plotted an asynchronous 2D SFG correlation spectrum in Fig. 5.8. The appearance of a positive asynchronous peak located at the spectral coordinate (ν_1, ν_2) indicates that the SFG intensity variation observed during the LCST process at ν_1 occurs predominantly before that at ν_2 . However, the sequential order is reversed if the sign of the corresponding synchronous correlation intensity at the same spectral coordinate (ν_1, ν_2) becomes negative. This is the case for the spectral coordinates $(2975\text{ cm}^{-1}, 2914\text{ cm}^{-1})$, where the asynchronous cross-peak is positive, while the synchronous crosspeak is negative. This indicates that the CH_2 contribution is decreasing before the CH_3 as is increasing, and that this effect gets stronger at higher temperature. The same holds for the spectral coordinate at $(2975\text{ cm}^{-1}, 2992\text{ cm}^{-1})$, which has a positive cross correlation in the asynchronous spectra and a negative crosspeak in the synchronous spectra. The peak at $(2975\text{ cm}^{-1}, 2985\text{ cm}^{-1})$ is positive in both correlation spectra. This means that the change in the CH_3 as contribution at 2975 cm^{-1} is appearing after the change in the other CH_3 as contributions at 2985 cm^{-1} and 2992 cm^{-1} , and the CH_2 as peak at 2914 cm^{-1} . The same separation can be observed for the CH_3 FR peak around 2889 cm^{-1} (see insert in Fig. 5.8).

To further investigate the dynamics of the transition itself, we plotted the fitted

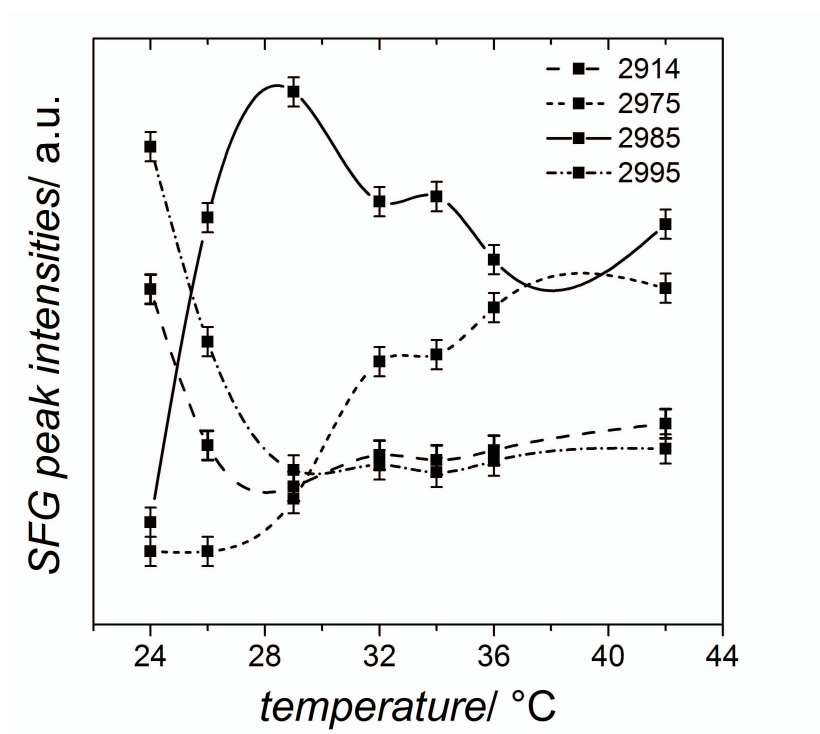


Figure 5.9: SFG peak intensities from the NBT-modified pNIPAM as a function of temperature - CH (2914 cm^{-1}), and CH_3 as (2975 cm^{-1} , 2985 cm^{-1} , and 2995 cm^{-1})
 - The LCST transition occurs at 32°C .

5. RESULTS & DISCUSSION OF POLY-N-ISOPROPYLACRYLAMIDE

peak intensities for various bands as a function of temperature (Fig. 5.9). The peak intensities support the findings of the 2D correlation analysis. In addition, the CH_2 at 2914 cm^{-1} and CH_3 as contribution at 2995 cm^{-1} are changing similarly during the phase transition. The latter one can be found only in crystalline isopropyl-formates, not in the amorphous state. Assuming that with increasing temperature the isopropyl and main chain CH_2 groups of the pNIPAM disorder further in comparison to the brush-like structure, these peaks may be regarded as order indicators of the structure within the pNIPAM film. The peak at 2985 cm^{-1} has a strong contribution in the amorphous IR spectra and a moderate contribution in the crystalline spectra of isopropyl-formates. In the SFG spectra, this peak is increasing in intensity while the peak at 2992 cm^{-1} is decreasing. Interestingly, these peak contributions are changing from 24° to 30°C , indicating a substantial molecular reorganization well below the LCST. This is in agreement with the ellipsometry data presented here and with Schmidt [12] and SPR measurements.[13, 14] However, the peak at 2975 cm^{-1} is increasing strongly only above 29°C , displaying a similar sharp transition as observed from contact angle measurements.[13] This may indicate that the inner structure of the pNIPAM film changes over a large temperature range, while the outer isopropyl groups orient themselves towards the liquid phase in a fairly sharp transition as observed for the CH_3 as peak at 2975 cm^{-1} . The fact that this peak is increasing, while the film structures collapses, further supports this interpretation. The corresponding sharp change in wettability can then be explained by a reorganization of the outer CH_3 groups adjacent to the water layer.

5.4.2 ATRP pNIPAM films

Spectra of the ATRP-pNIPAM films from the Zauscher group (see section 3.3.3) in *ppp* and *ssp* configuration were also acquired. See Fig. 5.10 and Fig. 5.11 for *ppp* and Fig. 5.13 and Fig. 5.14 for *ssp*. These films were much thicker than the previous NBT modified samples. A much more accurate temperature series were performed with the newly built SFG spectrometer system at KIT. Strong peaks from both the symmetric and asymmetric stretches of the methyl appear in the spectra, as well as the Fermi resonance at $\sim 2900\text{ cm}^{-1}$. The insets show the symmetric and asymmetric peak areas as function of temperature. Surprisingly, there is a remarkable difference between both samples. In contrast to the 230 nm thick film, following the findings from the NBT-modified pNIPAM film, the 110 nm film shows a different trend. There is a decrease with temperature for the asymmetric methyl resonance. Since the spectra are all normalized to the non-resonant background, this is not due to laser intensity drifts.

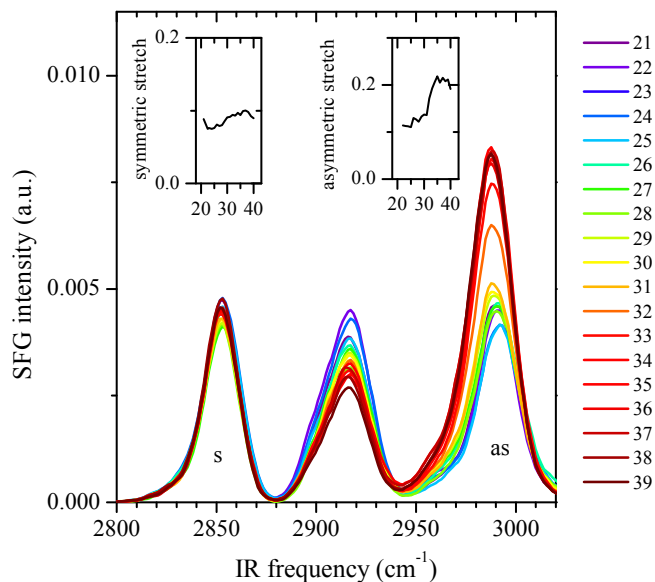


Figure 5.10: Resonant contributions of a *ppp* SFG spectra, showing CH stretching region of a 230 nm thick pNIPAM film on gold in water - the temperature was ramped from 20 to 40°C. Integrated peak areas of the symmetric and asymmetric stretch are shown as insets.

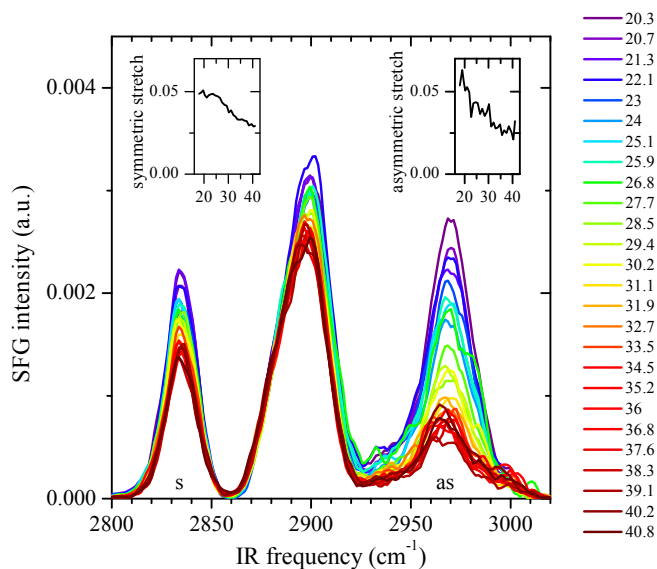


Figure 5.11: Resonant contributions of a *ppp* SFG spectra, showing CH stretching region of a 110 nm thick pNIPAM film on gold in water - the temperature was ramped from 20 to 40°C. Integrated peak areas of the symmetric and asymmetric stretch are shown as insets.

5. RESULTS & DISCUSSION OF POLY-N-ISOPROPYLACRYLAMIDE

In comparison, the other resonances stay relatively constant. This could be explained by a preferential azimuthal angle of the isopropyl groups, indicating that the polymer chains are combed from one side to the other. This type of arrangement would have a big influence on *ppp* spectra as calculated in 4.8a and 4.8b. However, the sample is not uniform enough on the scale of the laser spot size, therefore the ensemble average over the twist angle is zero.

By checking the relative change of spectral features, valuable information can be obtained. For example, in both cases there is a plateau above $\sim 35^\circ\text{C}$ even though spectra were acquired in this temperature region for more than two hours after the LCST was reached compared to just 30 minutes sweeping time from 20 to 30°C . This extended time measurement at the higher temperature state was obtained during the measurement of the hysteresis of the LCST phase transition.

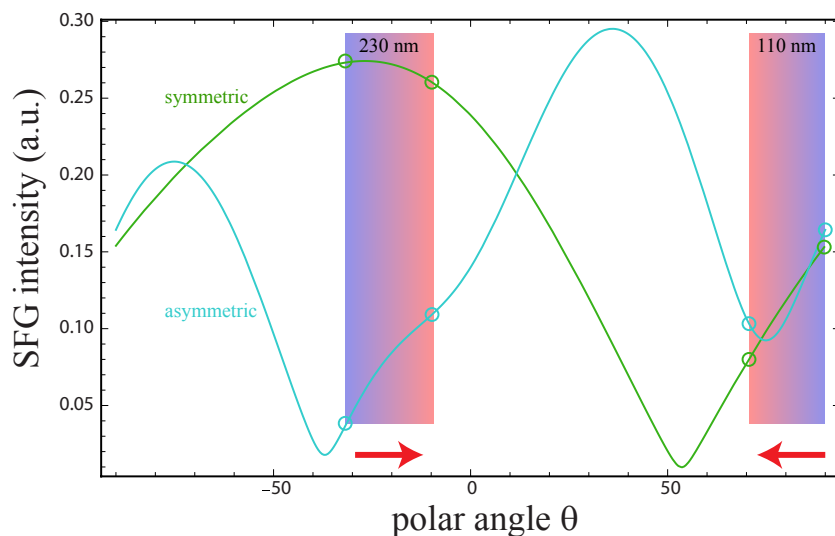


Figure 5.12: Simulated symmetric and asymmetric methyl stretch *ppp* SFG intensity as function of polar molecular angle - the gradient filled rectangular are indicating the range of changes of the polar angle upon the LCST transition for two different films. The red arrows are showing the direction of the temperature change.

The absolute change of the polar angle θ can also be quantified with the help of simulations. Plotting the asymmetric and symmetric SFG response can hint at how the methyl groups are orienting themselves. In Fig. 5.12, the possible angular changes are marked in the simulated curve. Thickness of the water film was set to $1\ \mu\text{m}$, the polymer film to 150 nm, and an isotropically distributed azimuthal ϕ was assumed.

The other parameters are the same as in the simulations described in section 4.3. In the 230 nm film the polar angle of the methyl group is turned from -30° to -10° upon the LCST and for the 110 nm film the methyl is turned from 90° to 70° . Using these turns, the intensity changes fit with the observe spectral dynamic. In both cases the methyl groups orient themselves at a 20° angle towards the interface upon reaching the LCST. Knowing these angles, conclusions for the polymer backbone can be made. Assuming that the isopropyl groups are oriented at an angle normal to the backbone, the polymer chains can then be assumed to be at a normal angle for the the 110 nm film, and tilted by 60° for the 230 nm film. A higher packing density in the 110 nm film would lead to a more straight orientation of the backbones, due to steric restrictions. The thicker film may have a lower density at the interface due to the polydispersity, with a few longer strands sticking out of the interface. These strands have more space and will tilt themselves arbitrarily to maximize the entropy.

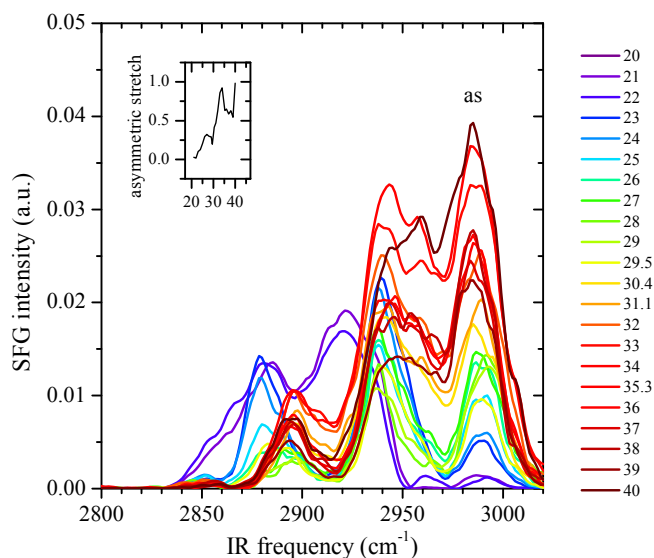


Figure 5.13: Resonant contributions of a *ssp* SFG spectra, showing CH stretching region of a 230 nm thick pNIPAM film on gold in water - the temperature was ramped from 20 to 40°C. Integrated peak areas of the symmetric and asymmetric stretch are shown as insets.

The *ssp* spectra are much easier to analyze, since they are reflecting only about half the amount of hyperpolarizability tensor elements than the *ppp* spectra shown in table 4.2 and 4.3. On the other hand, they are much more difficult to obtain experimentally, these spectra have on average about 50 times less absolute intensity, which is the reason for the poorer quality compared to the *ppp* spectra.

5. RESULTS & DISCUSSION OF POLY-N-ISOPROPYLACRYLAMIDE

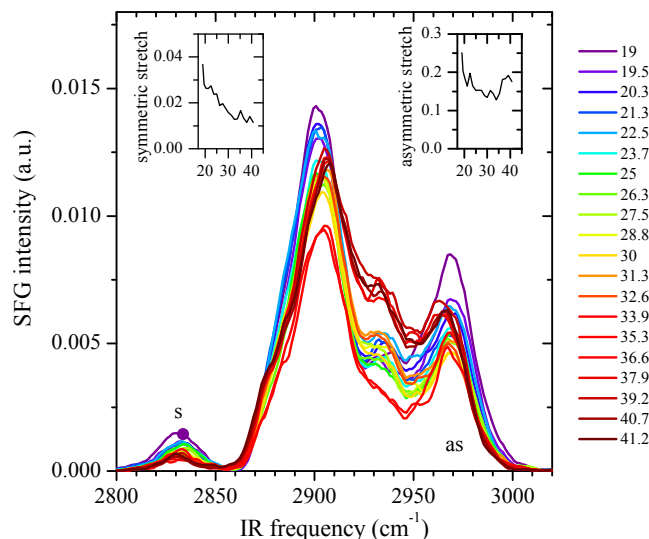


Figure 5.14: Resonant contributions of a *ssp* SFG spectra, showing CH stretching region of a 110 nm thick pNIPAM film on gold in water - the temperature was ramped from 20 to 40°C. Integrated peak areas of the symmetric and asymmetric stretch are shown as insets.

The first astonishing observation is the presence of asymmetric resonance in both spectra, which is not possible for $\phi=0$. (Fig 4.6d) There must therefore be an azimuthal preferential orientation such as the one showed in Fig. 4.8d ($\phi=30^\circ$). All peaks observed in the *ppp* spectra are also present in the *ssp* spectrum, even though some peaks are much smaller. In the 110 nm film spectrum, the small symmetric peak decreases with temperature even more, fitting with the simulated spectra in Fig 4.6c. Here, the intensity is decreasing while the molecular polar angle θ decreases from 90 to 70°. This is in agreement with the findings from the *ppp* spectra of this film. The spectrum of the 230 nm thick film is much more complex. The increasing asymmetric peak fits with the small feature in Fig. 4.8d assuming the proposed change in θ from 30 to 10° and also an azimuthal angle of 30°. All the spectral features at around 2900 cm⁻¹ and 2950 cm⁻¹ are also due to CH₂ resonances, which makes the system too undefined for further quantitative conclusions. However, it can be concluded that there are numerous rearrangement processes occurring, with the maximum change in relative intensities occurring between 25 - 32°.

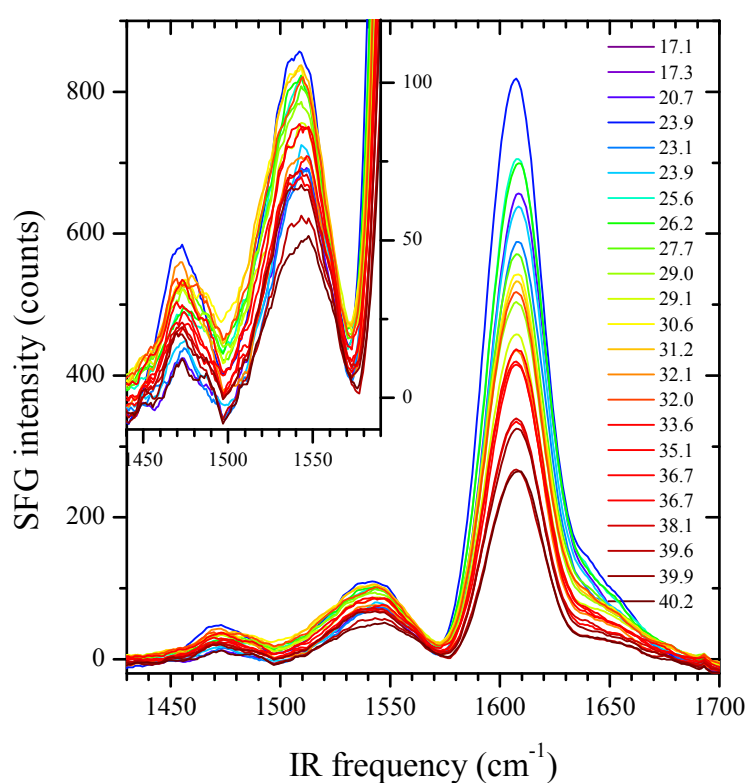


Figure 5.15: Background suppressed SFG spectra, showing Amide region of a 230 nm thick pNIPAM in air during a temperature sweep - inset shows a zoom of the two smaller bands.

5. RESULTS & DISCUSSION OF POLY-N-ISOPROPYLACRYLAMIDE

5.5 SFG of the Amide region

The Amide I region was investigated with SFG in air (see Fig. 5.15) using the purging chamber and the background suppressed mode. The peaks at 1620 cm^{-1} and 1660 cm^{-1} are assigned for the stretch of the C=O group (Amide I), in a hydrated environment and in association with the C=O...H-N, respectively. [15, 16] Additionally, the lower band can be assigned to a C=O hydrated with two water molecules and the upper band a C=O with only one following the procedures of Eaton et al. [17]. As shown in Fig. 5.16, the C=O bands have a quite complex structure with bands up to 1700 cm^{-1} . The peak at 1750 cm^{-1} can be attributed to the "free" C=O.[18] All this indicates the presence of a variety of different chemical environments. The previous temperature sweep data shown in Fig. 5.15 shows both bands decreasing in parallel. This implies that there is still water incorporated in the samples even in dry atmosphere, but that the amount decreases with decreasing temperature. It has also been verified that the peak intensities do not recover after cooling the sample down again.(data not shown) It is likely that exposing the samples to water would be needed to transform them back into a more ordered structure. The peaks at 1540 cm^{-1} and 1560 cm^{-1} are assigned to the N-H stretch (Amide II) and display no significant temperature-dependent changes. Spectral features at around 1470 cm^{-1} were observed as well, and are assigned to CH bending peaks. These peaks remain constant during heating, indicating that there is no orientational change of the film in air. But since these bending peaks carry no information additional to the CH stretching bands and are more difficult to record due to the necessary purging, they are not further analyzed in this work.

Interestingly the signal obtained in air is heavily dependent upon the position on the sample where the measurement is taken. these strong features appeared to be present only in particular domains of the sample. Also, the intensity of these spectral features in air were stronger than the signal from the gold substrate. This can only be the case for signals not only originating from the interface but the bulk of the film as well, which would need to be in crystal like conformation.

Further spectra were recorded for these samples in water. In Fig. 5.16 the black curve shows the spectra in air, the blue one in water at 17°C , and the red one at 36°C . For the air spectra, three different spectra were joined together to obtain a more complete picture of the spectral region. As soon as water is introduced, the signal vanishes due to a random orientation in the mixed phase. After heating a small signal is recovered. The complete vanishing at low temperatures means that there is a different conformation in the collapsed state in water, compared to a dry sample in air. These

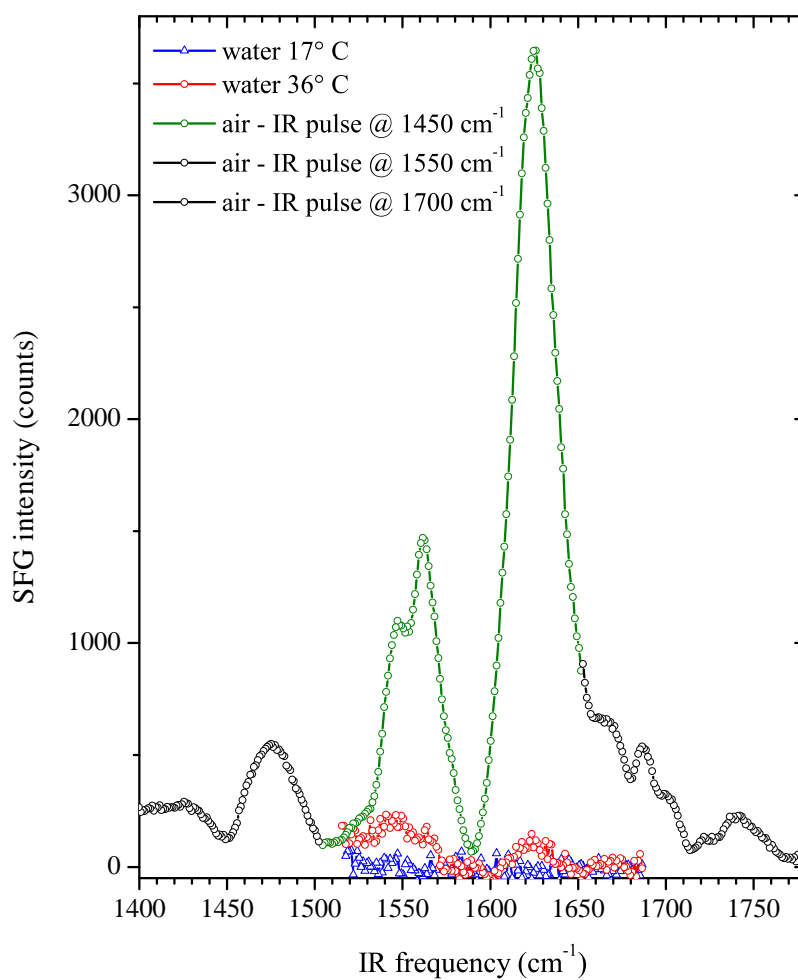


Figure 5.16: Background suppressed SFG spectra, showing Amide I band of 110 nm thick pNIPAM - (black circles) air spectra, (blue triangles) spectra in H₂O at 17° and 36° (red circles).

5. RESULTS & DISCUSSION OF POLY-N-ISOPROPYLACRYLAMIDE

observations were true for all thicknesses of pNIPAM films tested. The small peaks which are recovered above the LCST are an indication of a preferential orientation of C=O in the collapsed state. However, the signal to noise ratio is here not good enough to perform more detailed temperature-dependent studies of the orientational dynamics upon the LCST *in situ* of the C=O stretches.

5.6 SFG of the OH region

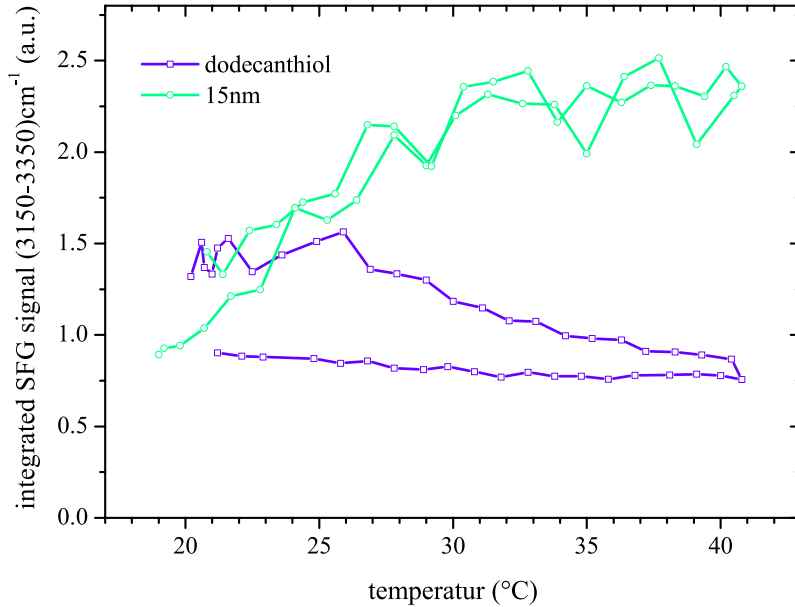


Figure 5.17: Integrated SFG intensity in the spectral region of OH stretches acquired with *ssp* and in the background suppressed mode, normalized with the reference line signal. - (green) 15 nm thick pNIPAM, (blue) control sample of dodecanthiol

In order to study interfacial water organization associated with these films (section 3.3.3), we performed experiments in the OH water vibrational region around 3150 cm^{-1} . These vibrations typically reveal a broad SFG band between 3000 and 3600 cm^{-1} ,^[19, 20] which exceeds the 200 cm^{-1} spectral width of the 90 fs IR beam. Therefore, analysis of the SFG signal in this region requires the use of the REF beam as described in Sec. 2.3.3. Figure 5.17 shows the integrated OH peak intensity over the detected spectral region centered at 3250 cm^{-1} (green line). A control sample was measured to check for incorporated temperature drifts. In this case an alkane thiol DDT

film on gold (prepared as described in section 3.2) was used. The control exhibited significant temperature drifts, which are due to thermally induced misalignments. The trend observed in pNIPAM film roughly mirrors the dynamics of the methyl stretches (green line) and from the captive contact angle. The OH signal doubles in intensity from 20°C to 32°C, after which a plateau is reached where the intensity remains constant. The water has a constant degree of order at the interface in the segregated phase. In the mixed phase the interface is not as distinct and there is therefore no overall orientational order of the water, leading to a minor SFG signal.

5.7 Conclusions

We studied the LCST phase transition of immobilized pNIPAM films on Au using *in situ* broadband SFG spectroscopy, ellipsometry, and contact angles. The results suggest a continuous change of the molecular conformation within the pNIPAM film starting below the LCST transition temperature of 32°C. Above this temperature, only subtle changes can be observed. Since macroscopic quantities like film thickness reveal changes within a narrow temperature range (1-2 °C), our results suggest that reorientation of the functional isopropyl groups within the film is involved, but is not the actual trigger for the macroscopic change in thickness. This is related to a reorientation of the outermost CH₃ groups towards the water phase in a narrow temperature range around 32°C, corresponding to the previously observed sharp change of the advancing contact angle and for low grafting densities also with the captive bubble contact angle. The bulk film collapses gradually, but the isopropyl groups located at the top of the film are change their orientation almost instantly.

A quantification of the molecular angles during the rearrangement at the LCST transition was possible and suggested a 20° smaller polar angle of the isopropyl groups upon segregation. In thick films the polymer backbone is more tilted, while in thinner films the chains are oriented more along the surface normal. Additionally, only ultrathin films with low grafting densities (5%) exhibit a instantaneous change of the chemical potential of the brushes at the LCST, while thicker films gradually change their chemical potential with temperature. SFG studies in the Amide I region showed the possibility of having semi-crystalline structures in these films in air with water molecules incorporated even in a dry atmosphere, although the remaining water could be evaporated by heating the film. A detailed structural analysis of the C=O group is possible in air, but the interesting dynamics in aqueous solutions are almost completely hidden due to a unordered arrangement of the backbone and therefore a low

5. RESULTS & DISCUSSION OF POLY-N-ISOPROPYLACRYLAMIDE

SFG signal.

Investigations of the interfacial water with SFG on thin pNIPAM films hold valuable information similar to that which can be obtained in captive contact angle measurements. The water molecules at the interface gradually become increasingly ordered due to a more distinct interface with temperature, providing further confirmation of a gradual temperature-dependent transition in these films.

References

- [1] B. Sun, Y. Lin, and P. Wu, "Structure analysis of poly(n-isopropylacrylamide) using near-infrared spectroscopy and generalized two-dimensional correlation infrared spectroscopy," *Appl. Spectrosc.*, vol. 61, pp. 765–771, 2007. [92](#)
- [2] D. N. Rockwood, D. B. Chase, R. E. Akins, and J. F. Rabolt, "Characterization of electro-spun poly(n-isopropyl acrylamide) fibers," *Polymer*, vol. 49, no. 18, pp. 4025–4032, 2008. [92](#)
- [3] H. Yamauchi and Y. Maeda, "Lcst and ucst behavior of poly(n-isopropylacrylamide) in dmso[water mixed solvents studied by ir and micro-raman spectroscopy," *J. Phys. Chem. B*, vol. 111, pp. 12964–12968, 2007. [92](#)
- [4] A. M. Jonas, K. Glinel, R. Oren, B. Nysten, and W. T. S. Huck, "Thermo-responsive polymer brushes with tunable collapse temperatures in the physiological range," *Macromolecules*, vol. 40, pp. 4403–4405, 2007. [93](#)
- [5] K. N. Plunkett, X. Zhu, J. S. Moore, and D. E. Leckband, "Pnipam chain collapse depends on the molecular weight and grafting density," *Langmuir*, vol. 22, no. 9, pp. 4259–4266, 2006. [93](#)
- [6] R. Pelton, "Poly(n-isopropylacrylamide) (pnipam) is never hydrophobic," *J. Colloid Interface Sci.*, vol. 348, no. 2, pp. 673 – 674, 2010. [93](#)
- [7] X. H. Cheng, H. E. Canavan, M. J. Stein, J. R. Hull, S. J. Kweskin, M. S. Wagner, G. A. Somorjai, D. G. Castner, and B. D. Ratner, "Surface chemical and mechanical properties of plasma-polymerized n-isopropylacrylamide," *Langmuir*, vol. 21, no. 17, pp. 7833–7841, 2005. [93](#)
- [8] T. Miyamae, H. Akiyama, M. Yoshida, and N. Tamaoki, "Characterization of poly(n-isopropylacrylamide)-grafted interfaces with sum-frequency generation spectroscopy," *Macromolecules*, vol. 40, no. 13, pp. 4601–4606, 2007. [97](#)
- [9] M. D. Porter, T. B. Bright, D. L. Allara, and C. E. D. Chidsey, "Spontaneously organized molecular assemblies .4. structural characterization of normal-alkyl thiol monolayers on gold by optical ellipsometry, infrared-spectroscopy, and electrochemistry," *J. Am. Chem. Soc.*, vol. 109, no. 12, pp. 3559–3568, 1987. [97](#), [98](#)
- [10] R. L. Rosas, H. H. Liefoghe, J. Laane, and B. J. Vanderveken, "Conformational-analysis and vibrational-spectra of isopropyl formate and some deuterated isotopomers," *J. Raman Spectrosc.*, vol. 24, no. 3, pp. 143–165, 1993. [95](#), [97](#)
- [11] I. Noda and Y. Ozaki, *Two-dimensional Correlation Spectroscopy - Applications in Vibrational and Optical Spectroscopy*. John Wiley & Sons Ltd., 2004. [95](#)

REFERENCES

- [12] S. Schmidt, H. Motschmann, T. Hellweg, and R. von Klitzing, "Thermoresponsive surfaces by spin-coating of pnipam-co-paa microgels: A combined afm and ellipsometry study," *Polymer*, vol. 49, no. 3, pp. 749–756, 2008. [100](#)
- [13] S. Balamurugan, S. Mendez, S. S. Balamurugan, M. J. O'Brien, and G. P. Lopez, "Thermal response of poly(n-isopropylacrylamide) brushes probed by surface plasmon resonance," *Langmuir*, vol. 19, no. 7, pp. 2545–2549, 2003. [100](#)
- [14] S. Balamurugan, L. K. Ista, J. Yan, G. P. Lopez, J. Fick, M. Himmelhaus, and M. Grunze, "Reversible protein adsorption and bioadhesion on monolayers terminated with mixtures of oligo(ethylene glycol) and methyl groups," *J. Am. Chem. Soc.*, vol. 127, no. 42, pp. 14548–14549, 2005. [100](#)
- [15] A. Percot, X. X. Zhu, and M. Lafleur, "A simple ftir spectroscopic method for the determination of the lower critical solution temperature of n-isopropylacrylamide copolymers and related hydrogels," *J. Poly. Sci. B: Polymer Physics*, vol. 38, pp. 907–915, 2000. [106](#)
- [16] Y. Maeda, T. Higuchi, and I. Ikeda, "Change in hydration state during the coil-globule transition of aqueous solutions of poly(n-isopropylacrylamide) as evidenced by ftir spectroscopy," *Langmuir*, vol. 16, pp. 7503–7509, 2000. [106](#)
- [17] G. Eaton, M. C. R. Symons, and P. P. Rastogi, "Spectroscopic studies of the solvation of amides with n-h groups. part 1. the carbonyl group," *J. Chem. Soc., Faraday Trans. 1*, vol. 85, pp. 3257–3271, 1989. [106](#)
- [18] Y. Hirashima, H. Sato, and A. Suzuki, "Atr-ftir spectroscopic study on hydrogen bonding of poly(n-isopropylacrylamide-co-sodium acrylate) gel," *Macromolecules*, vol. 38, pp. 9280–9286, 2005. [106](#)
- [19] G. L. Richmond, "Molecular bonding and interactions at aqueous surfaces as probed by vibrational sum frequency spectroscopy," *Chem. Rev.*, vol. 102, pp. 2693–2724, 2002. [108](#)
- [20] S. Gopalakrishnan, D. F. Liu, H. C. Allen, M. Kuo, and M. J. Shultz, "Vibrational spectroscopic studies of aqueous interfaces: Salts, acids, bases, and nanodrops," *Chem. Rev.*, vol. 106, pp. 1155–1175, 2006. [108](#)

6

Oligo ethylene-glycol

6.1 Quantum chemical calculations

These studies aim to increase understanding of the interfacial properties of polymer-based layers with IRRAS and SFG vibrational spectroscopy. As a model system for *ab initio* studies, ethylene-based system are investigated with quantum chemical tools. Ethylene glycol strands adopt a variety of conformationally different structures whose occurrences can be determined by the energetics of the system. *Ab initio* studies of one simple EG unit such as 2-methoxy ethanol (1-hydroxy 2-methoxy ethane, HME) [1, 2, 3, 4, 5, 6, 7, 8, 9, 10] have demonstrated that several conformations exist and that hydrogen bonding plays a significant role. For larger systems like OEG strands the situation becomes more complicated, however these types of systems have also been studied by *ab initio* methods [11, 12] and Monte Carlo calculations.[13, 14, 15, 16]

The *ab initio* calculations done for this work are triggered by SFG spectra in the CH stretching region and will explain the drastic changes of the OEG layers upon a changing environment. The HME is representative of the polymer chains' last repeating unit, which is contributing the most to the overall SFG signal. The effect of water is simulated with the simplest case of just one water molecule next to and interacting with the HME.

6.1.1 Method

All calculations were performed with the Gaussian03 suite of programs.[17] The calculation method was chosen in order to have the best fit with the vibrational resonances observed in IR and SFG spectra. [18] The MP2 level with the 6-31+G(d) basis set was used with very tight convergence criteria. The scaling factor was tuned to 0.937 to fit

6. OLIGO ETHYLENE-GLYCOL

the spectra.

6.1.2 Results

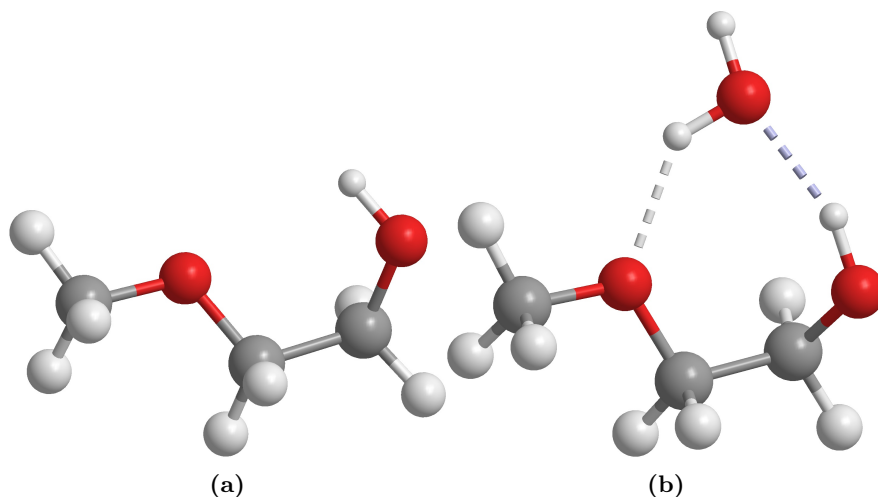


Figure 6.1: Geometry optimized conformations of HME (a) in air (b) interacting with a H_2O molecule

HME spectra with and without water were calculated. About 95% of the HME should be in the lowest energy conformations, as determined by Buck [18]. They also concluded that there is only one water molecule interacting with each EG unit. After a geometry optimization the molecule adopt a conformation shown in Fig. 6.1a and Fig. 6.1b with a water molecule present.

The Gaussian input file with the cartesian coordinates of HME is shown here:

```
# MP2/6-31+G(d) SCF=tight Opt=tight Freq=raman
```

```
[2-met-eth (tg+g-): opt; freq(raman)]
```

```
0 1
O 0 -2.233934 -0.000000 -1.230601
C 0 -0.821268 0.000000 -1.185237
C 0 -0.363154 0.000000 0.262015
O 0 -0.860915 -1.152889 0.895142
C 0 -0.474732 -1.223912 2.251030
H 0 -2.567611 -0.784351 -0.788238
H 0 -0.469339 0.907093 -1.725946
H 0 -0.469339 -0.907093 -1.725946
H 0 -0.751715 0.905352 0.783512
H 0 0.750610 -0.004433 0.307965
H 0 -0.902303 -2.156010 2.683497
```

H	O	-0.877134	-0.351950	2.812974
H	O	0.633949	-1.267039	2.334655

The corresponding IR and Raman intensities were calculated. With the Gabedit software[19], the Gaussian output file was loaded and the vibrational modes were visualized. All vibrations of the CH_3 were ignored in order to correlate the results with the spectra of EG_1OH . The CH_2 IR and Raman resonance intensities were taken and multiplied pairwise in order to simulate the SFG spectra. The peak width was set to 35 cm^{-1} and constant intensity factor was applied to match the count numbers of the spectra.

A comparison of *ab initio* and experimental data of the EG_1OH in air and D_2O is shown in Fig. 6.2a and 6.2a, where the SFG data is acquired with the background subtraction mode as described in section 2.3.2.1. The sample preparation was as described in section 3.4.

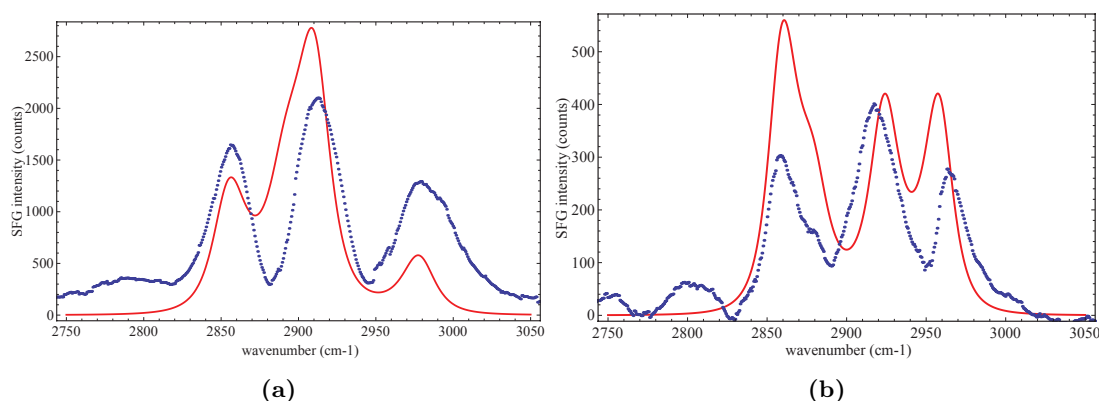


Figure 6.2: *Ab initio* and experimental spectra of EG_1OH - (points) experimental data (solid line) calculated spectra. (a) in air (b) in D_2O

Due to the good agreement between the calculated and measured resonance frequencies, this technique was used for the peak assignments for all the other samples. The *ab initio* calculations were only performed for this simple system, since the coordinates of the molecules were already well known. The mismatch in relative intensities is easily explainable, as in the simulated spectra no symmetry considerations, which are very crucial for SFG, were taken into account. For bigger molecules the predicted relative intensities will not match the experimental spectra at all, therefore molecular angles and symmetry considerations need to be addressed as well. The general influence of factors such as molecular tilt angles on SFG spectra is addressed in section. 4.2.5

6.2 SFG results

The orientation and conformation of self-assembled oligo (ethylene glycol) (EG_x , $x=1-6$) and poly (ethylene glycol) (PEG2000) monolayers on gold with OH and OCH_3 terminating groups are investigated. *In situ* broadband sum-frequency-generation (SFG) spectroscopy was applied in air and aqueous solutions in the CH stretching region. The effects of different salts and temperatures on the ultrathin film were investigated.

We used the homebuilt TLC, where the sample itself is probed through the base of a CaF_2 prism and a water film a few micrometers thick, located above the sample. The temperature of the liquid cell is controlled by a circulating bath. The incident angles of the s/p-polarized visible and p-polarized infrared beam were 67° and 61° , respectively.

To normalize the SFG signals, the resonant contributions were compared to the non-resonant background signal produced by the gold substrate. This signal is not sensitive to the solution above the sample or the position on the sample. Therefore, the non-resonant signal intensity was used for intensity and phase calibrations.

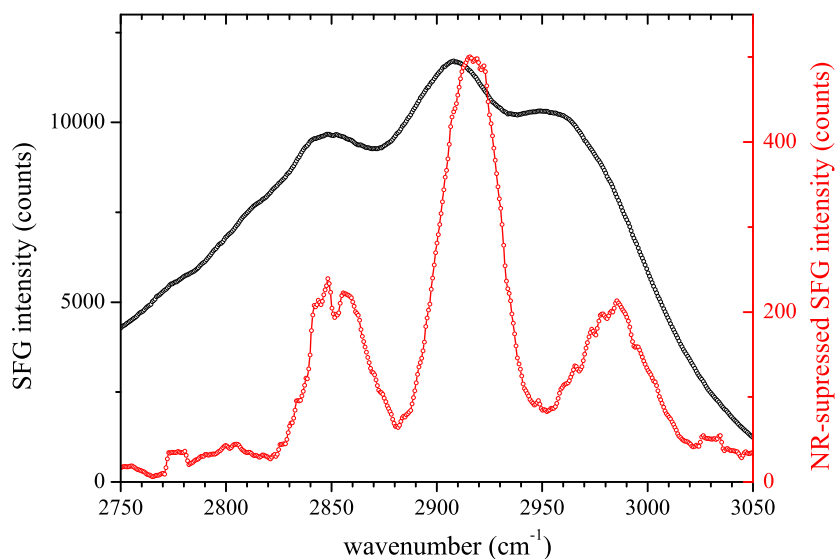


Figure 6.3: SFG spectra in the CH stretching region of EG_1OH . - (black) raw spectra (red) background suppressed spectra with 300 fs delay offset.

In Fig. 6.3 two spectra of EG_1OH are shown. The spectrum exemplified by the black lines is more commonly used usually for analyzing SFG data, since the signal to noise is much better. For simplifying the fitting process, a background-suppressed spectra was acquired as well. This was obtained following the routine in described in section 2.3.2.1 with 300fs delay offset. These background-suppression procedure allows

for the deduction of the relative phase of each resonant contribution. The obtained relative phase $\Phi_{rel} = \Phi_{gold} - \Phi_{res}$ was $\sim 80^\circ$ between non-resonant and resonant contributions. A starting value of 20 cm^{-1} was set for the resonant peak during the fitting routine.

6.2.1 Chain length effect

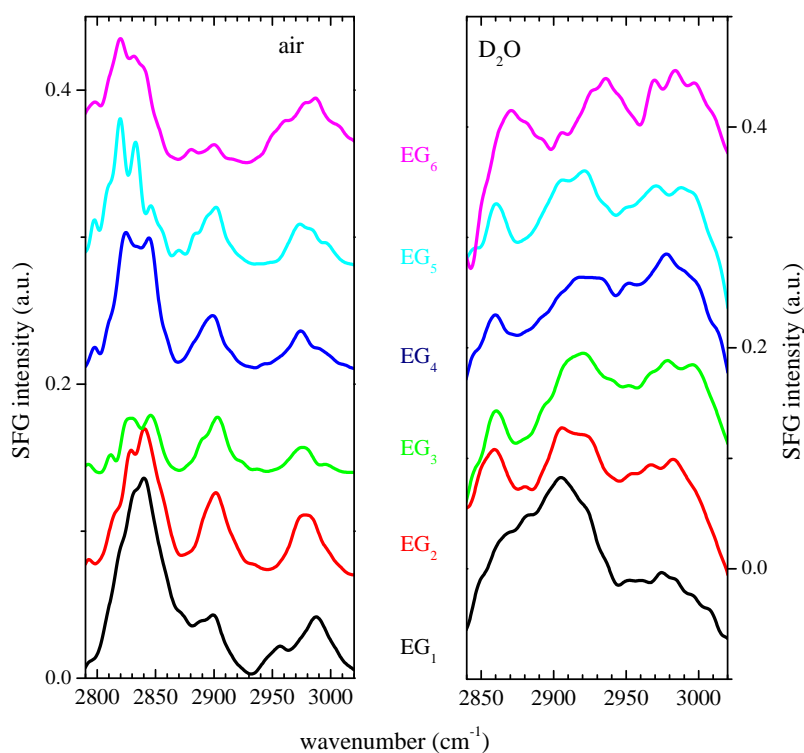


Figure 6.4: SFG spectra in the CH stretching region of $\text{EG}_1\text{OH}-\text{EG}_6\text{OH}$ - left side spectra in air, right side in D_2O .

The first set of measurements show the CH vibration band of OH-terminated ethylene glycol SAMs of different chain length on gold. The SFG spectra shown in Fig. 6.4 were recorded both in aqueous media and in air for comparison. The SFG setup used for these measurements had pulse energies three times lower than the one described in the methods chapter, but was otherwise similar.

The spectral features are comparable with IR spectra obtained from other researchers. For peak assignments several IR spectroscopy papers together with *ab initio*

6. OLIGO ETHYLENE-GLYCOL

calculations done in this work and from Buck [18] were used. The assignments are summarized in Tab. 6.1.

Vib. Mode	D ₂ O	Air
CH ₂ sym. alcy	2850	2850 [20]
CH ₂ asym. alcy	2900	2900 [20]
CH ₂ sym. EG gauche	2860[21]	2845 [20, 22]
CH ₂ asym. EG	2970[21]	2950 [20, 23], 2980 [21]
CH ₃ sym. EG	2820	2820 [22]
CH ₃ asym. EG	2980	2980 [22]

Table 6.1: SFG peak assignments

The spectra in air look similar for each chain length. For the longer chains, however, there are two general trends in which the peaks are become broader and change the relative peak intensities. The broadening of the peaks is attributed to the methylene of the EG units which have more possible conformations in longer chains and therefore also other preferred conformations. This may also result in a shifting of the peaks. The strong dependency of the conformation on the resonance frequency can be reviewed in [18]. For example the peak at around 2980 cm⁻¹ is assigned to the asymmetric methylene of a helical conformation. The basis of one helix are three EG units with gauche defects[12]. The peak assigned for methylene asymmetric stretch in the alkyl linker at 2900 cm⁻¹ remains more or less constant. In the case of EG₆OH this stretch is much smaller, likely since this sample was prepared differently and with a linker, that consisted of only 2 methylene groups.

The polymer surface is drastically affected by water as shown in Fig. 6.4. The spectra are dominated by three broad features located at 2860, 2900 and 2975 cm⁻¹. Strong hydration effects shift the symmetric methylene vibration of EG by 20 cm⁻¹ towards 2860 cm⁻¹. But in EG₁OH this hydrated peak is not present, indicating that the necessary hydrated conformation is maybe not possible for only one unit. For EG₆OH this peak is already broadened due to more conformational realizations. The asymmetric CH₂ blue shifts up to 2960 cm⁻¹. The more EG units present the more this peak is blue shifted. This is in agreement with the symmetric stretch and indicates that the film is more effectively hydrated when the chains are longer.

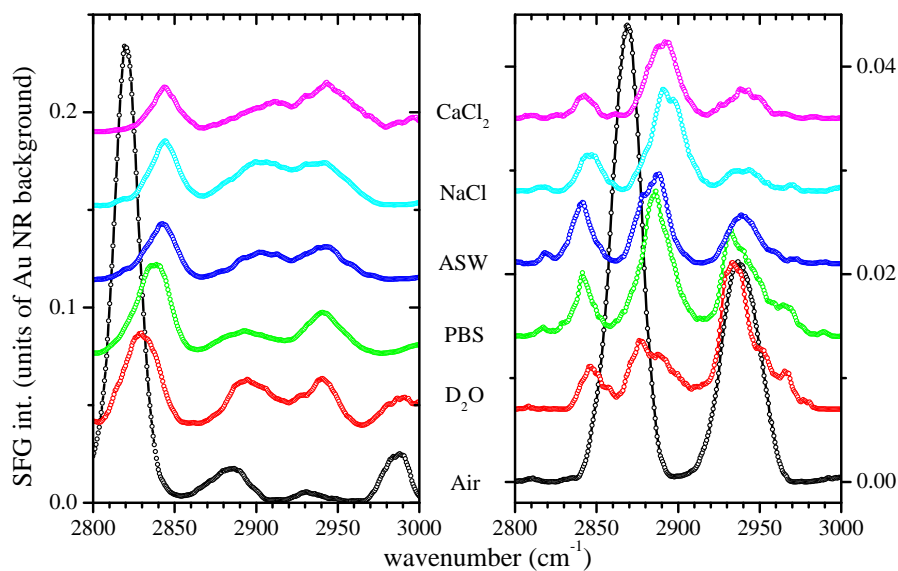


Figure 6.5: SFG spectrum of EG₆OMe (left) and EG₆OH (right) - different aqueous environments are stacked

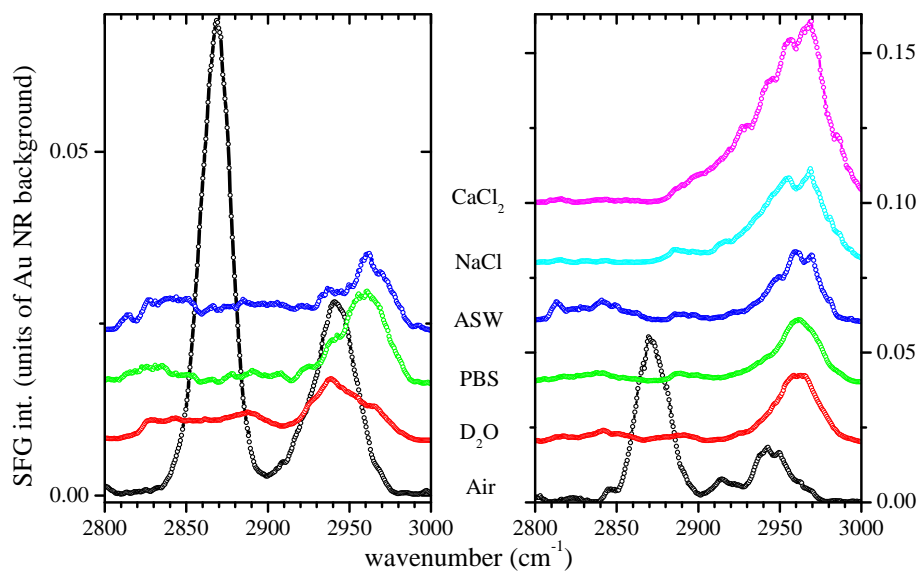


Figure 6.6: SFG spectrum of PEG2000OH (left) and PEG2000OMe (right). - different aqueous environments are shown

6. OLIGO ETHYLENE-GLYCOL

6.2.2 Environmental effects

In figure 6.5 and 6.6 SFG spectra of EG₆ and PEG2000 are shown. These spectra were recorded in different aqueous solutions in order to mimic different environmental conditions. ASW was chosen for marine antifouling issues and PBS was chosen to be similar to the conditions in which implants are usually embedded. Sodium and calcium ions were introduced to test the effects of mono vs. divalent cations.

EG₆OH spectra are considerably different in aqueous solution. The prominent methylene peaks in air are due to a crystal-like *all trans* conformation.[14] This ordered structure of EG-SAMs under ambient conditions is heavily affected. The decrease of methylene peaks is very strong, indicating that the film surface become almost amorphous. The water introduces blue shifts of the symmetric methylene vibrations from 2865 cm⁻¹ to 2890 cm⁻¹. Considering the different aqueous media, there is no significant difference for the OH terminated SAM observable. Since the film is already completely hydrated in pure D₂O no further "ion" assisted increase in hydration occurs.

The spectra of EG₆OCH₃ reveals strong methyl peaks at 2820 cm⁻¹ and 2990 cm⁻¹. In air the interfacial methyl groups are all pointing towards the interface, resulting in a interfacial symmetry break. As soon as water is introduced the hydrophobic head-groups bend away from the interface in order to avoid hydration. With pure D₂O the methyl peaks are not completely removed, leaving some "dry" structure remaining. After the addition of different salts the symmetric methyl stretch becomes weaker and the asymmetric stretch is removed. Salt ions are helping to hydrate the film and to make the interface amorphous. Methylene peaks first increase in D₂O, indicating that the SAM still exhibits still some crystal-helical structure in the solvated state. This structure decreases with the addition of ions, which is due to the different properties of the ions. The most chaotropic ion solution CaCl₂, leads to least amount of orientation in the film.

The influence of different environmental conditions was also investigated for PEG2000. The spectra exhibit no difference for OH and OCH₃ terminated moieties. Since the oligomer is long, there are many conformational possibilities of one chain. When the headgroup is buried somewhere inside the film, no crystal like interface will build up. Like the shorter oligomers of ethylene glycol PEG also has a conformational change from air to water. However, only the asymmetric methylene vibrations are contributing to the SFG signal in water. The most hydrated film in CaCl₂ solution has also the strongest peak, emphasizing again, that hydration can help building ordered structure, since it is somehow disentangling the polymer chains.

6.2.3 Temperature effects

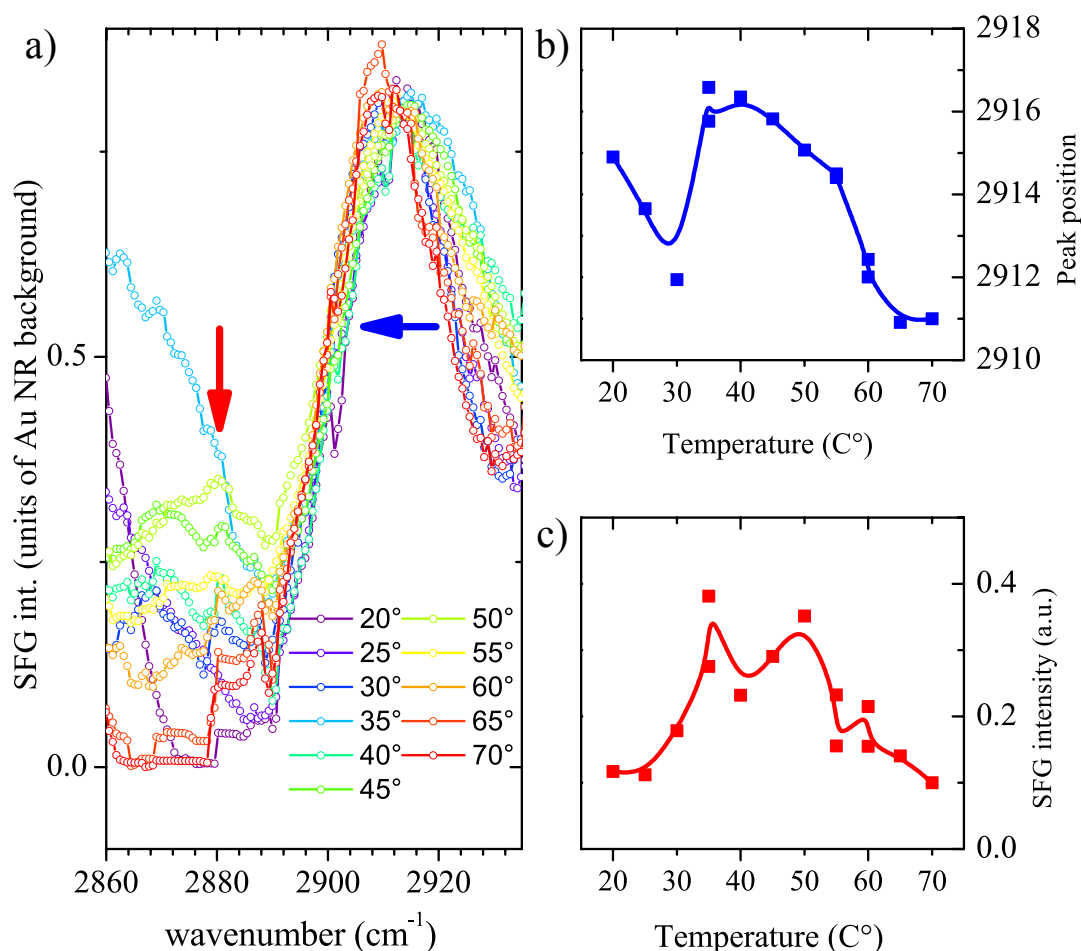


Figure 6.7: background suppressed SFG spectra of EG₆OH - (left) CH₂ ethylene glycol asymmetric stretch sample was measured in H₂O with *ssp* polarization and temperature was increased stepwise (a). (b) peak position of CH₂ asymmetric stretch, (c) peak amplitude of CH₂ symmetric of EG, indicating helical structure.

Spectra of EG₆OH in figure 6.7 were acquired in the background suppressing mode with the TLA. The asymmetric CH₂ attributed to the alkyl backbone was shifting with temperature, caused by a changing conformation and hydration.[23] At around 35° C even the backbone of the EG film gets hydrated, leading to the peak shift. But at 60° C the temperature is again high enough to remove the hydration and repel the water from the SAM backbone.

A measure of the conformation of the EG in the helical structure is the peak intensity

6. OLIGO ETHYLENE-GLYCOL

of the CH_2 symmetric stretch at 2880 cm^{-1} , plotted as function of temperature in Fig. 6.7c). The presence of helical structures in the EG film is therefore greatest from 35°C to 50°C .

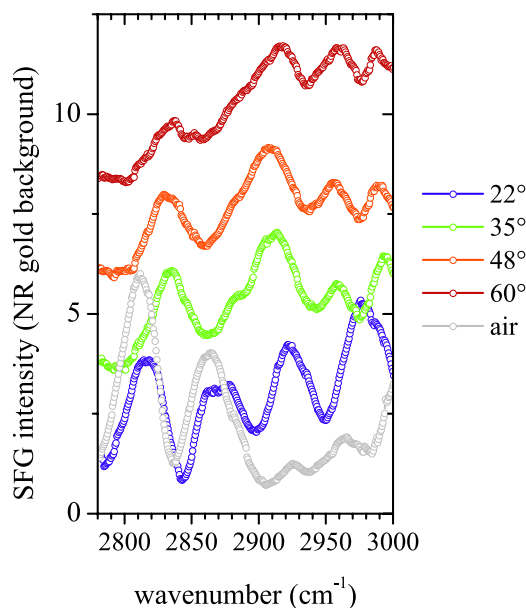


Figure 6.8: SFG spectra of EG_6OCH_3 SFG spectra in the CH stretching region with *ssp* polarization - Sample was measured in H_2O and temperature increased stepwise.

In Fig. 6.8 the temperature behavior of methyl terminated EG_6 is shown. All spectra beside the grey line were taken in an aqueous environment. The spectral pattern of the curve taken at 22°C is a mixture of those taken in air and those taken at a higher temperature. The film is not yet hydrated and the strong methylene peaks are indicating a well ordered methylene interface. At 35°C these peaks disappear as the interfacial methylene structure is distorted. The hydrated SAM is well structured at 35°C , all peaks are sharp and strong, but the CH_2 peaks become weaker at 48°C , and even more so at 60°C , as the EG helical structure becomes more random.

6.3 Conclusions

Oligo ethylene glycol SAMs show significant structural changes upon hydration. The hydration is dependent upon temperature, terminating groups and environmental conditions, making these SAMs useful as a model system to investigate these types of

effects. Upon hydration OEG SAMs lose their interfacial ordered structure, however the EG strands can arrange themselves into helical conformations which leads to an overall ordered structure gives rise to an SFG signal. The terminating group does not have any effect on long oligomers like PEG2000, but in short chains such as EG₆ the methyl-terminated SAMs are shielded against hydration. These layers can be hydrated, however, by increasing the temperature or adding salt.

REFERENCES

References

- [1] S. A. Vazquez, M. A. Rios, and L. Carballeira, "Molecular mechanics study of conformational trends in simple alcohols and ethers. 11. intramolecular hydrogen bonding," *J. Comput. Chem.*, vol. 13, pp. 851–859, 1992. [113](#)
- [2] S. Vázquez, R. A. Mosquera, M. A. Rios, and C. V. Alsenoya, "Ab initio-gradient optimized molecular geometry and conformational analysis of 2-methoxyethanol at the 4-21g level," *J. Mol. Struct.: THEOCHEM*, vol. 188, pp. 95–104, 1989. [113](#)
- [3] M. H. Langoor, L. M. J. Kroon-Batenburg, and J. H. V. der Maas, "Conformational analysis of alkoxyalcohols a combined ir and molecular mechanics study," *J. Chem. Soc., Faraday Trans.*, vol. 93, pp. 4107–4113, 1997. [113](#)
- [4] F. P. S. C. Gil, R. Fausto, A. M. A. da Costa, and J. J. C. Teixeira-Dias, "Structures and vibrational spectra of $\text{CH}_3\text{OCH}_2\text{CH}_2\text{OH}$: the hydrogen-bonded conformers," *J. Chem. Soc., Faraday Trans.*, vol. 90, pp. 689–695, 1994. [113](#)
- [5] F. P. S. C. Gil, A. M. A. D. Costa, and J. J. C. Teixeira-Dias, "Conformational analysis of $\text{C}_m\text{H}_{2m+1}\text{OCH}_2\text{CH}_2\text{OH}$ ($m = 1-4$): The role of CH-O intramolecular interactions," *J. Phys. Chem.*, vol. 99, pp. 8066–8070, 1995. [113](#)
- [6] F. P. S. C. Gil and J. J. C. Teixeira-Dias, "Structures and vibrational spectra for the conformers of $\text{CH}_3\text{OCH}_2\text{CH}_2\text{OH}$," *J. Mol. Struct.: THEOCHEM*, vol. 332, pp. 269–275, 1995. [113](#)
- [7] F. P. Gil and J. Teixeira-Dias, "Solvent effects on 2-methoxyethanol conformers: an ab initio dft study using the sci-pcmodel," *J. Mol. Struct.*, vol. 482-483, pp. 621–625, 1999. [113](#)
- [8] H. Yoshida, K. Takikawa, K. Ohno, and H. Matsuura, "Vibrational spectroscopic study of 2-methoxyethanol: matrix-isolation infrared spectra and conformational analysis based on ab initio mo calculations," *J. Mol. Struct.*, vol. 299, pp. 141–147, 1993. [113](#)
- [9] H. Yoshida, T. Harada, and H. Matsuura, "Conformational and vibrational analyses of 2-methoxyethanol and 2-(methylthio)ethanol by density functional theory," *J. Mol. Struct.*, vol. 413-414, pp. 217–226, 1997. [113](#)
- [10] H. Yoshida, K. Takikawa, I. Kaneko, and H. Matsuura, "Conformational analysis of model compounds of non-ionic surfactants in aqueous solution: Raman spectroscopy and ab initio mo calculations," *J. Mol. Struct.: THEOCHEM*, vol. 311, pp. 205–210, 1994. [113](#)
- [11] R. L. C. Wang and H. J. Kreuzer, "Molecular conformation and solvation of oligo(ethylene glycol)-terminated self-assembled monolayers and their resistance to protein adsorption," *J. Phys. Chem. B*, vol. 101, pp. 9769–9773, 1997. [113](#)

REFERENCES

- [12] R. L. C. Wang, H. J. Kreuzer, and M. Grunze, "The interaction of oligo(ethylene oxide) with water: a quantum mechanical study.," *Phys. Chem. Chem. Phys.*, vol. 2, no. 16, pp. 3613–3622, 2000. [113](#), [118](#)
- [13] A. J. Pertsin, M. Grunze, and I. A. Garbuzova, "Low-energy configurations of methoxy triethylene glycol terminated alkanethiol self-assembled monolayers and their relevance to protein adsorption," *J. Phys. Chem. B*, vol. 102, pp. 4918–4926, 1998. [113](#)
- [14] A. J. Pertsin and M. Grunze, "Computer simulations of water near the surface of oligo(ethylene glycol)-terminated alkanethiols self-assembled monolayers," *Langmuir*, vol. 16, pp. 8829–8841, 2000. [113](#), [120](#)
- [15] A. J. Pertsin, M. Grunze, H. J. Kreuzer, and R. L. C. Wang, "The effect of electrostatic fields on an oligo(ethylene glycol) terminated alkanethiol self-assembled monolayer," *Phys. Chem. Chem. Phys.*, vol. 2, pp. 1729–1733, 2000. [113](#)
- [16] A. J. Pertsin, T. Hayashi, and M. Grunze, "The interaction of oligo(ethylene glycol) with water: Testing an atomistic force field for transferability," *Phys. Chem. Chem. Phys.*, vol. 3, pp. 1598–1601, 2001. [113](#)
- [17] M. J. Frisch, G. W. Trucks, H. B. Schlegel, G. E. Scuseria, M. A. Robb, J. R. Cheeseman, J. A. Montgomery, Jr., T. Vreven, K. N. Kudin, J. C. Burant, J. M. Millam, S. S. Iyengar, J. Tomasi, V. Barone, B. Mennucci, M. Cossi, G. Scalmani, N. Rega, G. A. Petersson, H. Nakatsuji, M. Hada, M. Ehara, K. Toyota, R. Fukuda, J. Hasegawa, M. Ishida, T. Nakajima, Y. Honda, O. Kitao, H. Nakai, M. Klene, X. Li, J. E. Knox, H. P. Hratchian, J. B. Cross, V. Bakken, C. Adamo, J. Jaramillo, R. Gomperts, R. E. Stratmann, O. Yazyev, A. J. Austin, R. Cammi, C. Pomelli, J. W. Ochterski, P. Y. Ayala, K. Morokuma, G. A. Voth, P. Salvador, J. J. Dannenberg, V. G. Zakrzewski, S. Dapprich, A. D. Daniels, M. C. Strain, O. Farkas, D. K. Malick, A. D. Rabuck, K. Raghavachari, J. B. Foresman, J. V. Ortiz, Q. Cui, A. G. Baboul, S. Clifford, J. Cioslowski, B. B. Stefanov, G. Liu, A. Liashenko, P. Piskorz, I. Komaromi, R. L. Martin, D. J. Fox, T. Keith, M. A. Al-Laham, C. Y. Peng, A. Nanayakkara, M. Challacombe, P. M. W. Gill, B. Johnson, W. Chen, M. W. Wong, C. Gonzalez, and J. A. Pople, "Gaussian 03, Revision C.02." Gaussian, Inc., Wallingford, CT, 2004. [113](#)
- [18] M. Buck, "Ab initio calculations of vibrational spectra of 2-methoxy ethanol in the c-h stretching range.," *Phys. Chem. Chem. Phys.*, vol. 5, no. 1, pp. 18–25, 2003. [113](#), [114](#), [118](#)
- [19] A. ALLOUCHE, "Gabedit - a graphical user interface for computational chemistry softwares," *J. Comput. Chem.*, 2010. [115](#)
- [20] R. Valiokas, S. Svedhem, S. C. T. Svensson, and B. Liedberg, "Self-assembled monolayers of oligo(ethylene glycol)-terminated and amide group containing alkanethiolates on gold," *Langmuir*, vol. 15, no. 10, pp. 3390–3394, 1999. [118](#)

REFERENCES

- [21] L. Dreesen, C. Humbert, P. Hollander, A. A. Mani, K. Ataka, P. A. Thiry, and A. Peremans, “Study of the water/poly(ethylene glycol) interface by ir-visible sum-frequency generation spectroscopy,” *Chem. Phys. Lett.*, vol. 333, no. 5, pp. 327–331, 2001. [118](#)
- [22] P. Harder, M. Grunze, R. Dahint, G. M. Whitesides, and P. E. Laibinis, “Molecular conformation in oligo(ethylene glycol)-terminated self-assembled monolayers on gold and silver surfaces determines their ability to resist protein adsorption,” *J. Phys. Chem. B*, vol. 102, no. 2, pp. 426–436, 1998. [118](#)
- [23] R. Valiokas, M. Östblom, S. Svedhem, S. C. T. Svensson, and B. Liedberg, “Temperature-driven phase transitions in oligo(ethylene glycol)-terminated self-assembled monolayers,” *J. Phys. Chem. B*, vol. 104, pp. 7565–7569, 2000. [118](#), [121](#)

Acknowledgements

This work was performed at the Applied physical Chemistry at the Heidelberg University and during the last year also at the Karlsruhe Institute of Technology. First I would like to thank to Patrick Koelsch who was my supervisor in the field of research. He introduced me to the nonlinear optical spectroscopy and supported me in many areas and helped with his knowledge.

Prof. Michael Grunze the head of the APC department, for his steady support and fruitful discussions.

Dominique Verrault and all the other PhD-students and members of the Koelsch group for spending their time on discussions and cooperations.

Sören Schilp and Christoph Christophis from the Rosenhahn group for the preparation of the ATRP pNIPAM and EG films.

Jianming Eric Zhang from the group of Stefan Zauscher at Duke University for various pNIPAM films.

Stefan Zorn from Tübingen for borrowing his PM-IRRAS *in situ* cell for preliminary test.

Renate Reiter for using the ellipsometer in Freiburg.

Marta Cooperstein for arranging measuring time for the capturing bubble contact angle instrument at the University of New Mexico in Albuquerque.

Thanks the Deutsche Forschungsgemeinschaft (KO 3618/1-1 and 2) for financial support.